A cholinergic circuit that relieves pain despite opioid tolerance
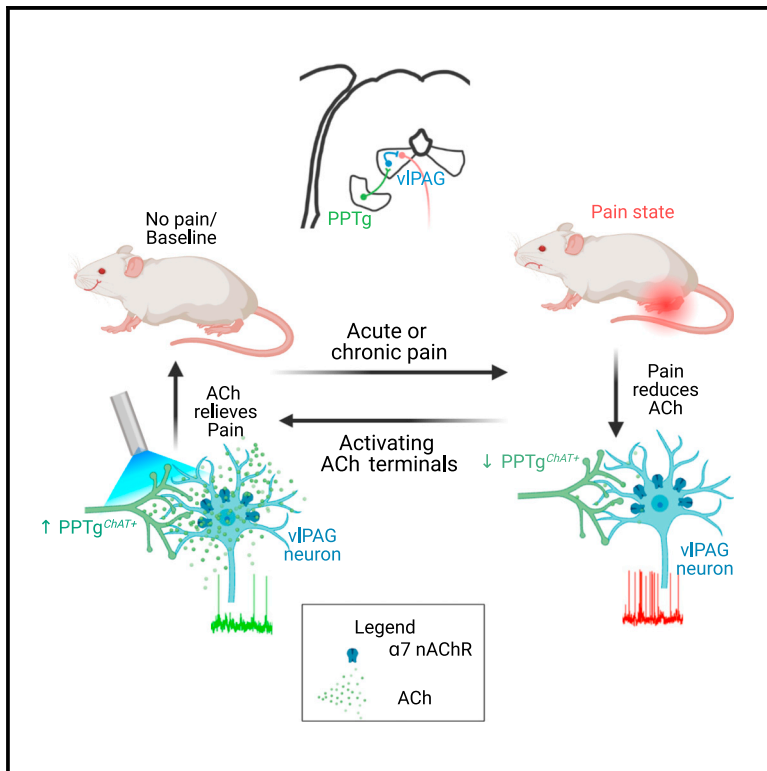
Graphical abstract

Authors

Shivang Sullere, Alissa Kunczt,
Daniel S. McGehee

Correspondence

dmcgehee@uchicago.edu

In brief

The role of central cholinergic signaling in pain modulation remains poorly understood. Sullere et al. identify an endogenous cholinergic circuit that regulates sensory and affective components of acute and chronic pain. Activating PPTg^{ChAT+} → vlPAG projections exerts profound analgesia through α7 nAChRs that inhibit vlPAG^{GABA+} neurons to relieve pain despite opioid tolerance.

Highlights

- Acute and chronic pain decrease ACh in the ventrolateral periaqueductal gray (vlPAG)

- Activating PPTg^{ChAT+} → vlPAG projections relieves somatic and affective pain behaviors

- α7 nAChRs mediate these analgesic effects by inhibiting vlPAG^{GABA+} neurons

- Analgesic potency of this cholinergic circuitry is preserved despite opioid tolerance

CellPress

Article

A cholinergic circuit that relieves pain despite opioid tolerance

Shivang Sullere,[1] Alissa Kunczt,[2] and Daniel S. McGehee[1,2,3,*]
[1]Committee on Neurobiology, University of Chicago, Chicago, IL 60637, USA
[2]Department of Anesthesia and Critical Care, University of Chicago, Chicago, IL 60637, USA
[3]Lead contact
*Correspondence: dmcgehee@uchicago.edu
https://doi.org/10.1016/j.neuron.2023.08.017

SUMMARY

Chronic pain is a tremendous burden for afflicted individuals and society. Although opioids effectively relieve pain, significant adverse outcomes limit their utility and efficacy. To investigate alternate pain control mechanisms, we explored cholinergic signaling in the ventrolateral periaqueductal gray (vlPAG), a critical nexus for descending pain modulation. Biosensor assays revealed that pain states decreased acetylcholine release in vlPAG. Activation of cholinergic projections from the pedunculopontine tegmentum to vlPAG relieved pain, even in opioid-tolerant conditions, through $\alpha7$ nicotinic acetylcholine receptors (nAChRs). Activating $\alpha7$ nAChRs with agonists or stimulating endogenous acetylcholine inhibited vlPAG neuronal activity through Ca^{2+} and peroxisome proliferator-activated receptor α (PPARα)-dependent signaling. *In vivo* 2-photon imaging revealed that chronic pain induces aberrant excitability of vlPAG neuronal ensembles and that $\alpha7$ nAChR-mediated inhibition of these cells relieves pain, even after opioid tolerance. Finally, pain relief through these cholinergic mechanisms was not associated with tolerance, reward, or withdrawal symptoms, highlighting its potential clinical relevance.

INTRODUCTION

Although opioids, such as morphine and fentanyl, are effective treatments for chronic pain,[1] their use is compromised by unpleasant side effects, abuse liability, the development of analgesic tolerance, and withdrawal symptoms.[2–6] Their increased availability has contributed to elevated incidence of opioid use disorder (OUD) and overdose-induced deaths.[3,5] These concerns highlight the need to identify novel non-opioid targets for pain management.[7]

The descending pain-modulatory pathway is an evolutionarily conserved neural circuit that encodes[8–13] and modulates nociceptive signaling based on internal states and external stimuli.[14,15] The ventrolateral periaqueductal gray (vlPAG) is a key regulator of this pathway,[16] and electrical,[17–24] pharmacological,[17,19,25–33] and chemogenetic[14,34–36] manipulation of this region produces profound analgesia. vlPAG is also a key site of endorphin-mediated analgesia,[22] and direct infusion of opioids into the vlPAG relieves pain by suppressing GABAergic drive onto projections to the rostral ventromedial medulla (RVM).[37,38] However, other non-opioid neuromodulators that alter pain through changes in vlPAG activity are less well studied. Although *in vivo* recordings in vlPAG have identified response characteristics of different neuronal populations, activity patterns of neuronal ensembles in acute and chronic pain states have not been studied.

Acetylcholine (ACh) is a key neuromodulator that affects cellular signaling and neuronal excitability in multiple brain regions to modulate behavior.[39–43] Although acetylcholinesterase inhibitors like donepezil and agonists of nicotinic and muscarinic ACh receptors (n/mAChRs) alter pain, the precise role of endogenous ACh and the cellular and network mechanisms that alter pain have not been thoroughly investigated.[44–47] Although anatomical studies reveal cholinergic terminals in the vlPAG,[48,49] their function is not known. Thus, understanding how these endogenous cholinergic circuits regulate vlPAG and the descending pain control circuitry to modulate pain may lead to novel analgesic treatments.

Here, we assayed ACh release dynamics in the vlPAG under various pain states using the novel ACh biosensor— GRAB$_{ACh\ 3.0}$.[50] Then, using anatomical and optogenetic approaches, we identified the source of ACh in the vlPAG and tested how manipulating ACh levels relieves somatic and affective aspects of pain. After establishing that ACh is an important neuromodulator in this system, we identified the receptor and intracellular signaling that mediate the analgesic effects of these cholinergic projections. These investigations are supplemented by electrophysiological and *in vivo* characterizations of pain-induced plasticity in the vlPAG. Finally, using *in vivo* 2-photon imaging, we explored the neuropathic pain-induced aberrant neuronal dynamics in the vlPAG and how opioids, opioid tolerance, and cholinergic modulation alter these
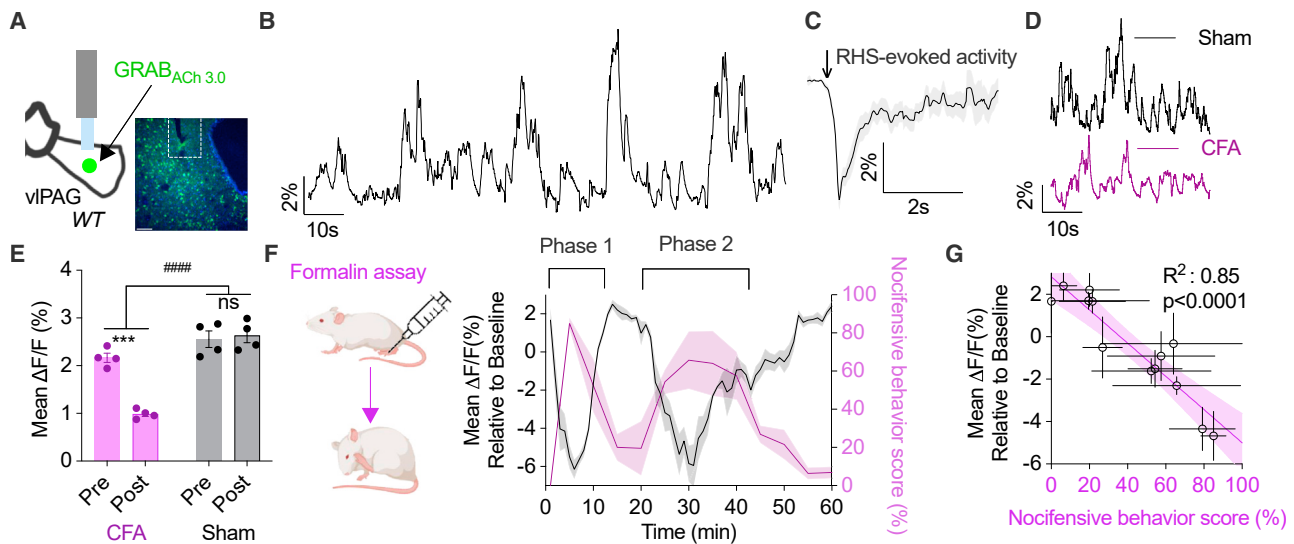
Figure 1. Nocifensive behaviors correlate with decreased ACh levels in the vlPAG

(A) Left: schematic of injection site and optical fiber placement (white dashed line) for the ACh fluorescent sensor, GRAB$_{ACh\ 3.0}$. Right: fluorescence image showing GRAB$_{ACh\ 3.0}$ (green) and nuclear DAPI stain (blue; scale bars, 50 μm).

(B) Representative recording of vlPAG GRAB$_{ACh\ 3.0}$ fluorescence dynamics recorded using fiber photometry during open-field behavior.

(C) Mean GRAB$_{ACh\ 3.0}$ fluorescence traces time locked to paw withdrawal in response to radiant heat source (RHS) assay (downward arrow, 6 traces per animal; n = 4 mice).

(D) Representative GRAB$_{ACh\ 3.0}$ fluorescence traces from sham-control (black) and CFA-injected animals (purple) collected 3 days after CFA/sham injection.

(E) Mean GRAB$_{ACh\ 3.0}$ fluorescence pre- and post-CFA injection (purple) and in sham controls (gray). n = 4 mice. ***p < 0.001 paired t test, ####p < 0.0001 interaction repeated measures (RM) two-way ANOVA.

(F) Left: schematic showing formalin injection in the plantar surface of the hind paw and subsequent monitoring of nocifensive behaviors for 1 h post formalin injection. Right: mean GRAB$_{ACh\ 3.0}$ fluorescence per minute on the left y axis (black) and the nocifensive behavior score (% time spent licking, lifting, or guarding paw in 5 min bins) on the right y axis (purple). Phase 1, 0–15 min and phase 2, 20–45 min. Fluorescence data normalized to 15 min of baseline before formalin administration.

(G) Negative correlation between nocifensive behavior score (%) and mean GRAB$_{ACh\ 3.0}$ fluorescence (ΔF/F%). Each point represents a separate 5 min bin. The error bars represent the standard error of mean (SEM) across animals in that time bin. n = 4 mice; shading represents 95% confidence interval.

Error bars and shaded areas represent SEM,

---

ensemble dynamics. Together, these investigations ultimately provide insights into novel cholinergic circuitry and receptor mechanisms that relieve pain despite opioid tolerance without evidence of withdrawal symptoms, reward profile, or the development of analgesic tolerance.

RESULTS

ACh release in the vlPAG is inhibited during nocifensive behaviors

We investigated pain-induced changes in ACh in the vlPAG using a biosensor—GRAB$_{ACh\ 3.0}$ (Figure 1A). This method revealed spontaneous ACh release in the vlPAG during open-field behavior (Figure 1B; Figure S1A). Acute painful stimuli transiently inhibited ACh release, as reflected in reduced GRAB$_{ACh\ 3.0}$ fluorescence (Figure 1C). Complete Freund's adjuvant (CFA) injected in the hindpaw induced a chronic inflammatory pain state, which decreased ACh transients and mean fluorescence (Figures 1D and 1E). Note that ACh levels in the vlPAG were not correlated with movement (Figures S1A and S1B). We verified this inverse relationship between ACh and pain using a single-session formalin assay to mitigate inter-session variability. Within a formalin assay, different temporal phases are associated with varying levels of nocifensive

behaviors[51] (Figure 1F). Phases associated with stronger nocifensive behaviors showed lower GRAB$_{ACh\ 3.0}$ fluorescence, indicating lower levels of ACh in the vlPAG and vice versa (Figures 1F and 1G). These observations suggest an interdependency between the pain state and cholinergic tone in the vlPAG.

Cholinergic PPTg neurons project to the vlPAG

Next, we explored the potential source of ACh in the vlPAG using anatomical labeling. We injected retrogradely transported virus[52] in the vlPAG of *ChAT-Cre* mice, which expresses tdTomato in presynaptic *Cre*-expressing neurons and enhanced yellow fluorescent protein (EYFP) in all back-labeled neurons[53] (Figure 2A). We verified the injection site (Figure 2B) and conducted whole-brain imaging (Figure 2C) to observe back-labeling in the pedunculopontine tegmental nucleus (PPTg) and laterodorsal tegmental nucleus (LDTg, Figure 2D). Sparse labeling was observed in the medial septum-diagonal band of Broca (MS-DBB, Figures 2C and 2D). These results agree with previous publications[48,49] and data from the Allen Institute. Next, we activated PPTg^{ChAT+} terminals optogenetically using ChrimsonR while monitoring ACh in the vlPAG with GRAB$_{ACh\ 3.0}$ and observed increased fluorescence, indicating that these projections release ACh (Figures S1C and S1D).
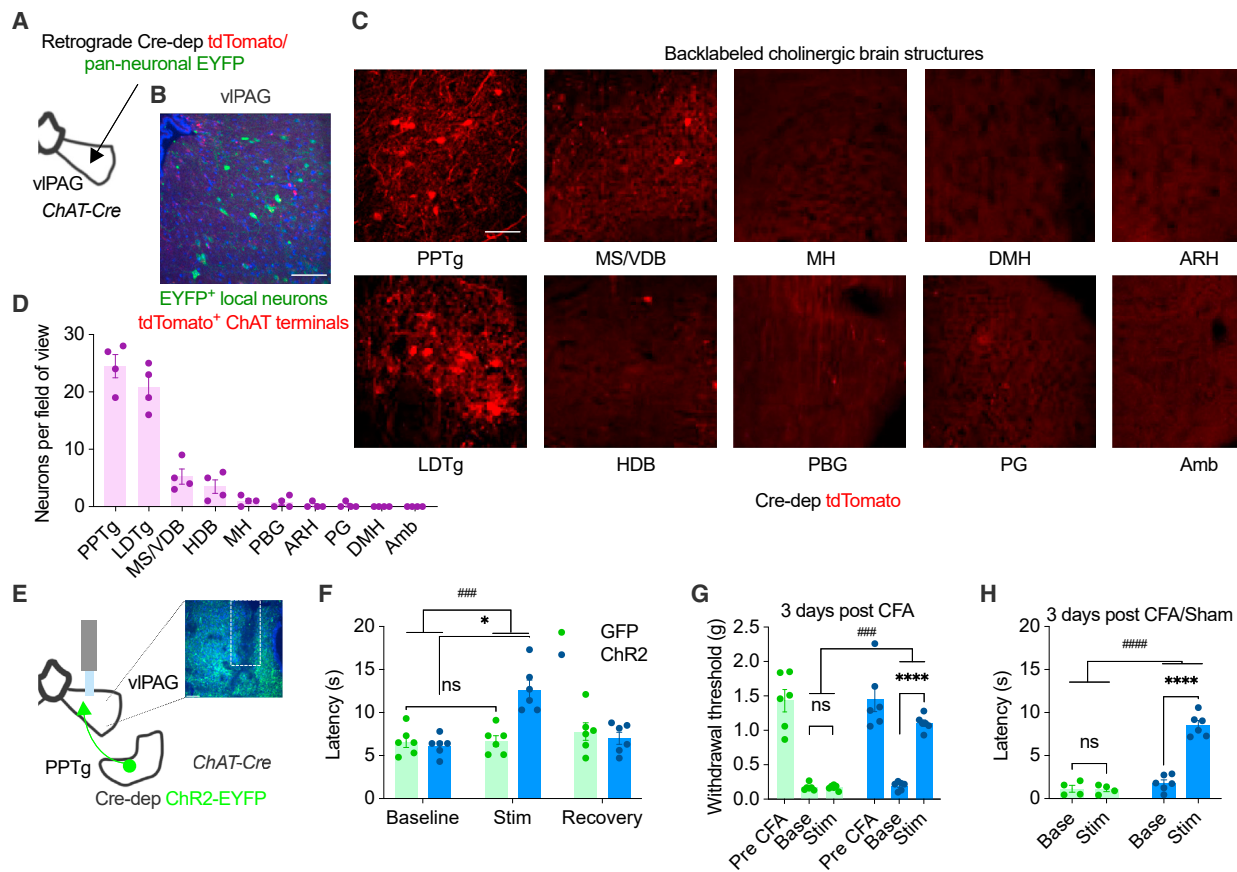
Figure 2. PPTg^{ChAT+} neurons project to vlPAG, and activating them is antinociceptive

(A) Schematic showing retrograde labeling strategy to express tdTomato in presynaptic *Cre*-expressing cholinergic neurons. EYFP was also expressed in the vlPAG to identify the injection site.

(B) Viral injection site with local neurons (green), cholinergic terminals (red), and DAPI-stained nuclei (blue; scale bars, 50 μm).

(C) Representative images of cholinergic brain structures with back-labeled neurons (red).

(D) Quantification of back-labeled cholinergic neurons per field of view (FOV). Each data point represents an animal. From each animal, at least 6 FOVs were collected per brain region, and the number of neurons were averaged per animal (n = 4 mice).

(E) Left: schematic of *Cre*-dependent ChR2 expression in PPTg^{ChAT+} neurons and cannula placement (white dashed line) in the vlPAG. Right: fluorescence image showing ChR2-expressing PPTg^{ChAT+} terminals (green) with DAPI stain (blue; scale bars, 50 μm).

(F) Paw withdrawal latency in a RHS assay during no stimulation (baseline), optogenetic stimulation (stim), and post-stimulation (recovery) in ChR2 (blue) and GFP (green) expressing mice. n = 6 mice. *p < 0.05 paired t test, ###p < 0.001 interaction RM two-way ANOVA.

(G) Paw withdrawal threshold in von Frey assay before (pre-CFA) and after CFA (green) during baseline and optogenetic stimulation (Stim) in ChR2 (blue) and GFP (green) expressing mice. n = 6 mice. ****p < 0.0001 paired t test, ###p < 0.001 interaction RM two-way ANOVA.

(H) Paw withdrawal latency in a RHS assay in CFA-injected mice (3 days prior) during baseline and optogenetic stimulation (stim) in ChR2 (blue) and GFP (green) expressing mice. n = 6 mice. ****p < 0.0001 paired t test, ####p < 0.0001 interaction RM two-way ANOVA.

Error bars represent SEM.

Activating PPTg^{ChAT+} → vlPAG projections is antinociceptive

Given the dense PPTg^{ChAT+} → vlPAG connectivity (Figure 2) and the negative correlation between nocifensive behaviors and ACh release in the vlPAG (Figure 1), we explored the pain-relieving effects of activating these projections. In *ChAT-Cre* animals, we expressed ChR2[54] or EYFP in PPTg^{ChAT+} neurons and placed an optical cannula in the vlPAG to activate cholinergic terminals (Figure 2E). Activating these cholinergic terminals increased the latency to paw flick in a radiant heat source (RHS) assay (Figure 2F). Activation of LDTg^{ChAT+} → vlPAG did not alter nocifensive responses (data not shown). Next, we explored the effects

of stimulating these terminals on CFA-induced chronic inflammatory pain. Although CFA injection induces hyperalgesia and allodynia, activating PPTg^{ChAT+} → vlPAG projections reversed these effects, with consistently increased paw withdrawal threshold (Figure 2G) and latency to paw flick in RHS and cold allodynia assays (Figure 2H; Figure S1F).

A recent study demonstrated that manipulating PPTg^{ChAT+} neuronal activity does not alter motor function,[55] and we also assessed the potential confounds on locomotion, anxiety, and general motor control using open-field assay,[56] rotarod assay,[57] and a high-power output RHS. In the open-field assay, stimulating PPTg^{ChAT+} → vlPAG projections did not alter the distance
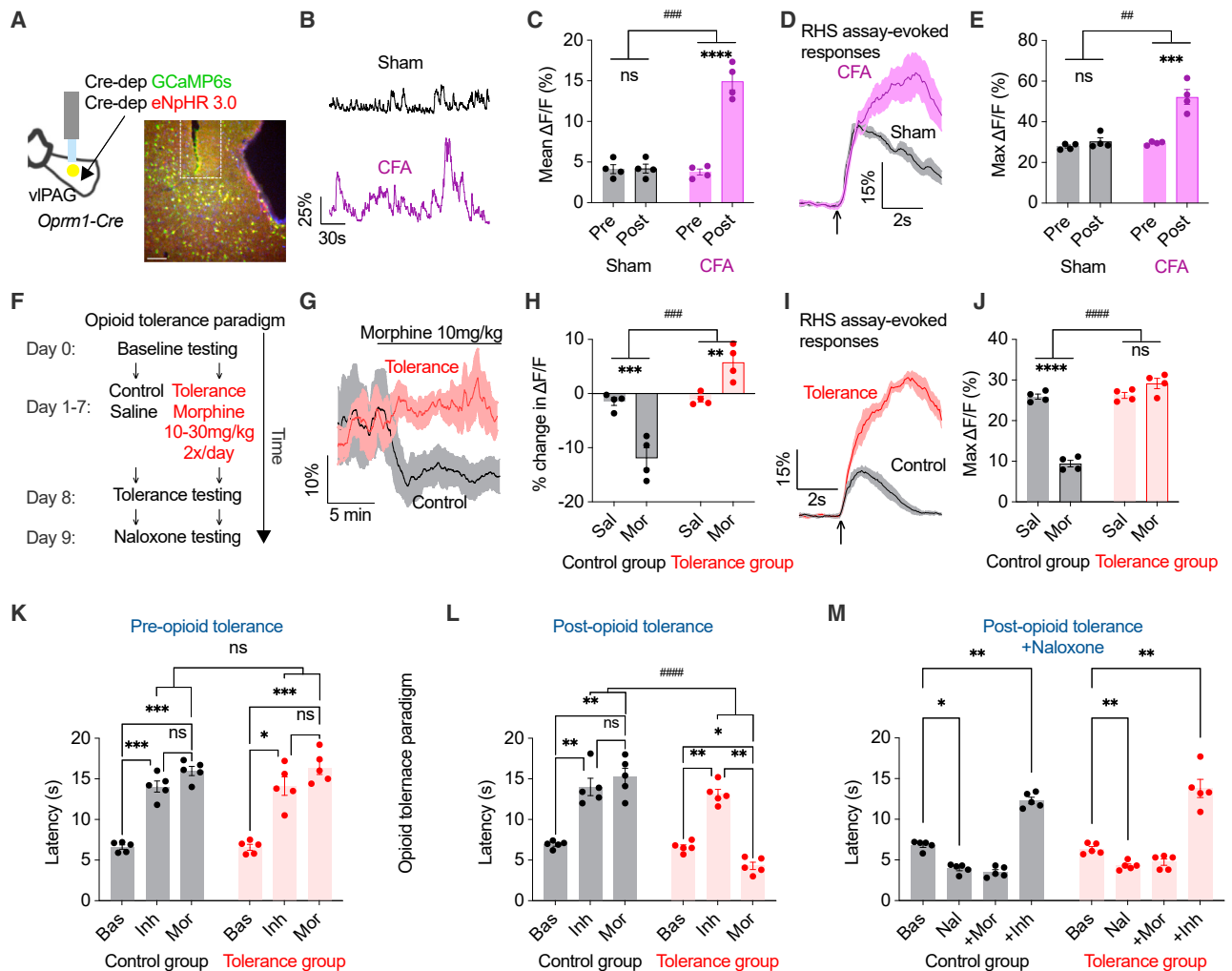
Figure 3. Inhibiting vlPAG^{Oprm1+} neurons is antinociceptive under baseline and opioid-tolerant conditions

(A) Left: schematic depicting GCaMP6 and eNpHR 3.0 expression in vlPAG^{Oprm1+} neurons and cannula placement (white dashed line) in the vlPAG. Right: fluorescence image showing GCaMP6 (green) and eNpHR 3.0 (red) expression with nuclear DAPI staining (blue; scale bars, 50 μm).

(B) Representative GCaMP6 fluorescence traces from vlPAG^{Oprm1+} neurons collected using fiber photometry during open-field behavior in CFA-injected (purple) and sham-control (black) mice. Data collected 3 days after CFA/sham injection.

(C) Mean fluorescence in sham-control (black) and CFA-injected mice (purple) before (Pre) and after (Post) CFA injection. n = 4 mice. ****p < 0.0001 paired t test, ###p < 0.001 interaction RM two-way ANOVA.

(D) Mean vlPAG^{Oprm1+} GCaMP6 fluorescence traces time locked to paw withdrawal in RHS assay (arrow) in CFA-injected (purple) and sham-control mice (black, 6 traces per mouse; n = 4 mice).

(E) Peak vlPAG^{Oprm1+} GCaMP6 fluorescence transient during RHS-evoked responses in sham-control (black) and CFA-injected mice (purple) during RHS assay. n = 4 mice. ***p < 0.001 paired t test, ##p < 0.01 interaction RM two-way ANOVA.

(F) Schematic of the tolerance exposure paradigm.

(G) Mean vlPAG^{Oprm1+} GCaMP6 fluorescence traces time locked to morphine administration (10 mg/kg) in opioid tolerance-exposed (red) or control (black) animals.

(H) Change in vlPAG^{Oprm1+} GCaMP6 fluorescence post morphine/saline (15–20 min) compared with before (10–5 min) in mice exposed to opioid tolerance (red) or controls (black). n = 4 mice. ***p < 0.001, **p < 0.01 paired t test, ###p < 0.0001 interaction RM two-way ANOVA.

(I) Mean vlPAG^{Oprm1+} GCaMP6 fluorescence traces time locked to paw withdrawal during RHS assay after morphine (10 mg/kg) injection in opioid tolerance-exposed or control animals.

(J) Peak vlPAG^{Oprm1+} GCaMP6 fluorescence time locked to paw withdrawal during RHS assay after morphine/saline administration in mice exposed to opioid tolerance (red) or controls (black). n = 4 mice. ****p < 0.0001 paired t test, ####p < 0.0001 interaction RM two-way ANOVA.

(K) Paw withdrawal latency in RHS assay before tolerance exposure in control (black) and tolerance (red) group during baseline (Bas), optogenetic inhibition (Inh), and after morphine administration (Mor, 10 mg/kg). n = 5 mice.

(L) Paw withdrawal latency in RHS assay after tolerance exposure in the control (black) and tolerance (red) groups during baseline (Bas), optogenetic inhibition (Inh), and after morphine administration (Mor, 10 mg/kg). n = 5 mice.

(legend continued on next page)

traveled, the number of movement bouts, or time spent in the center zone (Figures S1G, S1H, and S1I). In the rotarod assay, optogenetic activation did not alter the latency to fall (Figure S1J). Increasing thermal intensity in RHS assay lowered the latency to paw flick compared with regular RHS assay, even during optogenetic activation (Figure S1K). Thus, optogenetic activation of PPTg^{ChAT+} → vlPAG projections modulates nociception without altering motor function or anxiety levels.

Optogenetic inhibition of vlPAG^{Oprm1+} neurons is antinociceptive post-opioid tolerance

Repeated opioid use induces tolerance by reducing analgesic efficacy.[58–60] To test how μ-opioid receptor-expressing vlPAG neurons (vlPAG^{Oprm1+}) respond to nocifensive behaviors before and after opioid tolerance, we expressed the genetically encoded calcium indicator GCaMP6 in vlPAG^{Oprm1+} neurons using Oprm1-Cre mice (Figure 3A). Using in vivo fiber photometry (Figure 3B), we found that vlPAG^{Oprm1+} neurons are activated during nocifensive behaviors, such as paw withdrawal from acute nociceptive thermal stimuli in the RHS assay (Figure 3D). Also, CFA-induced chronic pain increased neuronal excitability, as evidenced by increased mean fluorescence (Figures 3B and 3C) and higher transient amplitude in response to nocifensive stimuli (Figures 3D and 3E). As expected, morphine (10 mg/kg i.p.) decreased mean fluorescence (Figures 3G and 3H) and transient amplitudes (Figures 3I and 3J, black control trace), suggesting that morphine inhibits vlPAG^{Oprm1+} neurons. Treatment of the mice with an escalating morphine regimen[58,61] (10 → 30 mg/kg over 7 days; Figure 3F) induced opioid tolerance, verified by a lack of increase in latency to paw flick after morphine administration (Figure S2A). Morphine doses that inhibited vlPAG^{Oprm1+} neurons in control mice did not inhibit vlPAG^{Oprm1+} neurons in opioid-tolerant mice (Figures 3G–3J, red-tolerant trace), indicating compromised inhibition. Hence, we tested whether cell-autonomous inhibition of vlPAG^{Oprm1+} neurons relieved pain in this opioid-tolerant state. We expressed the inhibitory opsin, halorhodopsin (eNpHR 3.0), in vlPAG^{Oprm1+} neurons and implanted a fiberoptic cannula in the vlPAG (Figure 3A). Halorhodopsin function was verified using simultaneous fiber photometry, where inhibition decreased mean fluorescence (Figure S2B). Optogenetic inhibition of vlPAG^{Oprm1+} neurons in opioid-naive mice increased latency to paw flick in RHS assay (Figure 3K), recapitulating the antinociceptive effects of morphine. After inducing and verifying opioid tolerance, we observed that optogenetic inhibition of vlPAG^{Oprm1+} neurons still increased the latency to paw flick (Figure 3L), even after naloxone (6 mg/kg i.p., Figure 3M). Separately, we verified that inhibiting vlPAG^{Oprm1+} neurons reduced thermal hyperalgesia associated with chronic pain (Figure S2C).

Finally, we tested whether activating PPTg^{ChAT+} → vlPAG projections recapitulates these observations and relieves pain in opioid-tolerant mice. Indeed, after opioid tolerance, when morphine lost its analgesic potency, optogenetic activation of PPTg^{ChAT+} → vlPAG projections increased paw withdrawal latency (Figures S2D and S2E). Furthermore, activation of PPTg^{ChAT+} → vlPAG projections also relieved pain, even after naloxone administration (Figure S2F), demonstrating conserved analgesic potency even after opioid tolerance.

α7 nAChRs mediate the analgesic effects of activating PPTg^{ChAT+} → vlPAG projections

To identify the mechanisms of the observed effects, we explored the underlying receptors. First, we assayed AChR mRNA in the vlPAG using fluorescence in situ hybridization (FISH).[62] We observed strong expression of Chrna7 and Chrm2 and weak expression of Chrm4 mRNA (Figure 4A; Figure S3A). Next, we sequentially administered receptor antagonists before activating PPTg^{ChAT+} → vlPAG projections and found that the systemic administration of α7 nAChR antagonist (methyllycaconitine [MLA] 6 mg/kg) blocks the antinociceptive effects (Figure 4B). Interestingly, pan-muscarinic (atropine 10 mg/kg) and M2 mAChR antagonist (AFDX-116 3 mg/kg) decreased baseline latencies to paw flick without changing the antinociceptive effects of activating this circuit (Figure 4B). Given the potential non-specific effects of the receptor antagonists in other areas of the nervous system, we verified our observations by focally infusing MLA into the vlPAG. The antinociceptive effects of activating PPTg^{ChAT+} → vlPAG projections were blocked by focal MLA infusion (Figure 4C). These observations implicate α7 nAChRs in the antinociceptive effects of activating this cholinergic circuit. Interestingly, the higher affinity M2 mAChRs may mediate baseline pain sensitivity given the baseline cholinergic tone (Figure 1).

To test if α7 nAChRs also mediate synaptic communication between PPTg^{ChAT+} and vlPAG neurons, we expressed channelrhodopsin 2 (ChR2) in PPTg^{ChAT+} terminals and recorded from vlPAG neurons in regions of densest innervation (Figure 4D). Activation of PPTg^{ChAT+} terminals evoked rapid inward currents (optically evoked excitatory postsynaptic currents [oEPSCs]) in 71% of the recorded neurons (n = 17 neurons, 6 mice, Figure 4E). These oEPSCs were blocked by MLA (10 nM) and recovered after washout (Figure 4F). Additionally, α-bungarotoxin (100 nM) irreversibly blocked these oEPSCs, whereas 6-cyano-7-nitroquinoxaline-2,3-dione (CNQX, 20 μM) did not alter them (Figures S3B and S3C). These observations demonstrate functional cholinergic synaptic transmission mediated through α7 nAChRs between evolutionarily conserved brain structures associated with descending pain modulation, a rare observation within the CNS.[43,63–67]

vlPAG$^{Chrna7+}$ neurons are activated during nocifensive behaviors in response to noxious stimuli

Given the importance of α7 nAChRs, we explored pain-induced changes in vlPAG$^{Chrna7+}$ neurons. First, we used fiber photometry to monitor α7 nAChR-expressing (vlPAG$^{Chrna7+}$) neurons using GCaMP6 and Chrna7-Cre mouse lines (Figure 5A). vlPAG$^{Chrna7+}$ neurons were activated by noxious stimuli that elicited nocifensive

(M) Paw withdrawal latency in RHS assay after tolerance and naloxone exposure during baseline (Bas), after naloxone (6 mg/kg, Nal) and morphine (Mor, 10 mg/kg) administration, and during optogenetic inhibition (Inh). n = 5 mice. *p < 0.05, **p < 0.01, ***p < 0.001, ****p < 0.0001 paired t test; ####p < 0.0001 interaction RM two-way ANOVA.
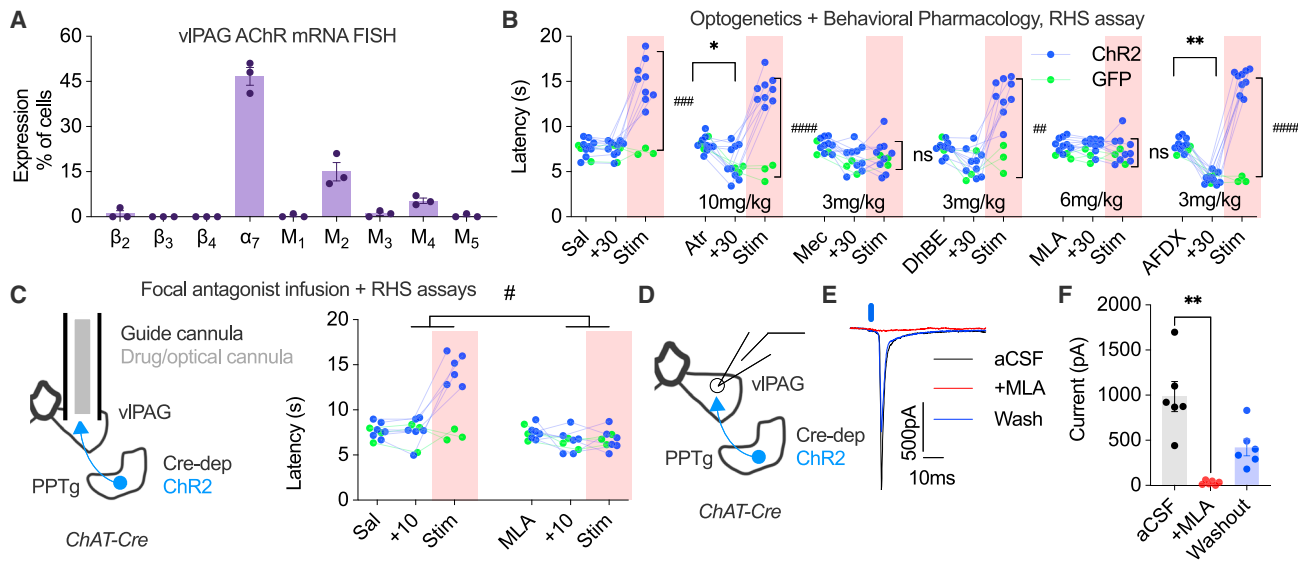
Error bars and shaded areas represent SEM.

Figure 4. α7 nAChRs mediate the antinociceptive effects of PPTg^{ChAT+} → vlPAG projections

(A) Fluorescent *in situ* hybridization (FISH) signal for AChR mRNA expression in vlPAG. n = 3 mice.

(B) Paw withdrawal latency in RHS assay for mice expressing ChR2 (blue) or GFP (green) in PPTg^{ChAT+} neurons before drug injection (drug name), 30 min after drug injection (+30), and after activation of PPTg^{ChAT+} terminals in vlPAG (Stim, pink shading). n = 9 mice for ChR2, 3 for GFP. *p < 0.05, **p < 0.01 paired t test; ##p < 0.01, ###p < 0.001, #####p < 0.0001 interaction RM two-way ANOVA.

(C) Left: schematic showing strategy for PPTg^{ChAT+} terminal activation along with focal drug infusion. Right: paw withdrawal latency in RHS assay in mice expressing ChR2 (blue) or GFP (green) in PPTg^{ChAT+} terminals in the vlPAG. RHS assay was conducted before drug administration (drug name), 10 min after focal drug infusion (+10), and after optogenetic stimulation (Stim). n = 6 mice for ChR2, 3 mice for GFP. #p < 0.05 interaction RM three-way ANOVA.

(D) Slice electrophysiology schematic to monitor optically evoked excitatory postsynaptic currents (oEPSCs). ChR2-expressing PPTg^{ChAT+} terminals were activated during voltage-clamp recordings (−70 mV) of vlPAG neurons.

(E) Representative trace demonstrating PPTg^{ChAT+} terminal activation-evoked oEPSC is blocked by bath application of α7 nAChR antagonist MLA (10 nM).

(F) Current amplitude of oEPSCs before, during, and after MLA (10 nM) bath perfusion. n = 6 cells, 4 mice. **p < 0.01 unpaired t test.

Error bars represent SEM.

behaviors selectively, including hot (55°C) and cold (2°C) water, von Frey filaments (1.4 g), radiant heat, noxious pinprick, and acetone (Figure 5B). These neurons were not strongly activated by other non-noxious stimuli, including somatosensory, visual, olfactory, or auditory stimuli (Figure 5B). CFA-induced chronic pain increased RHS-evoked transient amplitudes and mean fluorescence intensity, indicating elevated activity of vlPAG$^{Chrna7+}$ neurons compared with sham controls (Figures 5C and 5D). To identify the cellular basis of this plasticity, we recorded fluorescently labeled vlPAG$^{Chrna7+}$ neurons. Although we observed minimal differences between CFA and sham controls in intrinsic excitability and inhibitory drive (Figures S3D and S3E), we observed a significantly stronger excitatory synaptic drive to these vlPAG$^{Chrna7+}$ neurons in CFA-injected animals (Figures 5E and 5F). These observations suggest that inhibiting vlPAG$^{Chrna7+}$ neurons mediates the antinociceptive effects, which is counterintuitive as α7 nAChRs are cation channels that generally induce excitation. Hence, we investigated the pain-modulatory effects of inhibiting vlPAG$^{Chrna7+}$ using optogenetics.

Inhibiting vlPAG$^{Chrna7+}$ neurons is antinociceptive, despite opioid tolerance

We expressed eNpHR 3.0 on vlPAG$^{Chrna7+}$ neurons and implanted an optical cannula in vlPAG (Figure 5G). Optogenetic inhibition of these neurons increased the latency to paw flick in

acute thermal pain assays (Figure 5H). In CFA-induced chronic pain state, inhibiting vlPAG$^{Chrna7+}$ neurons increased latency to paw flick in RHS assay and increased paw withdrawal threshold in von Frey assay (Figure 5I; Figure S3F). Furthermore, inhibiting these neurons was antinociceptive in opioid-tolerant animals, even after naloxone administration (6 mg/kg, Figure S3G). After repeated opioid injections, naloxone induces somatic withdrawal signs, including jumping and rearing behaviors.[68–72] Optogenetic inhibition of vlPAG$^{Chrna7+}$ neurons during naloxone-precipitated withdrawal reduced these somatic signs (Figure S3H). Furthermore, inhibiting the activity of vlPAG$^{Chrna7+}$ neurons did not affect motor control or anxiety (Figure S3I). Given these somatic effects, we employed a real-time place preference assay to test if inhibiting vlPAG$^{Chrna7+}$ neurons relieved the affective component of chronic pain.[73] We observed that chronic pain-induced preference for the chamber paired with inhibition of vlPAG$^{Chrna7+}$ neurons compared with controls or mice not in chronic pain (Figure S3J). These observations suggest that inhibiting these neurons relieves the affective component of pain but does not induce preference in the absence of chronic pain.

α7 nAChR activation relieves pain by inhibiting the activity of vlPAG$^{Chrna7+}$ neurons

Given that inhibiting vlPAG$^{Chrna7+}$ neurons is antinociceptive, we tested the effects of optogenetic activation of endogenous
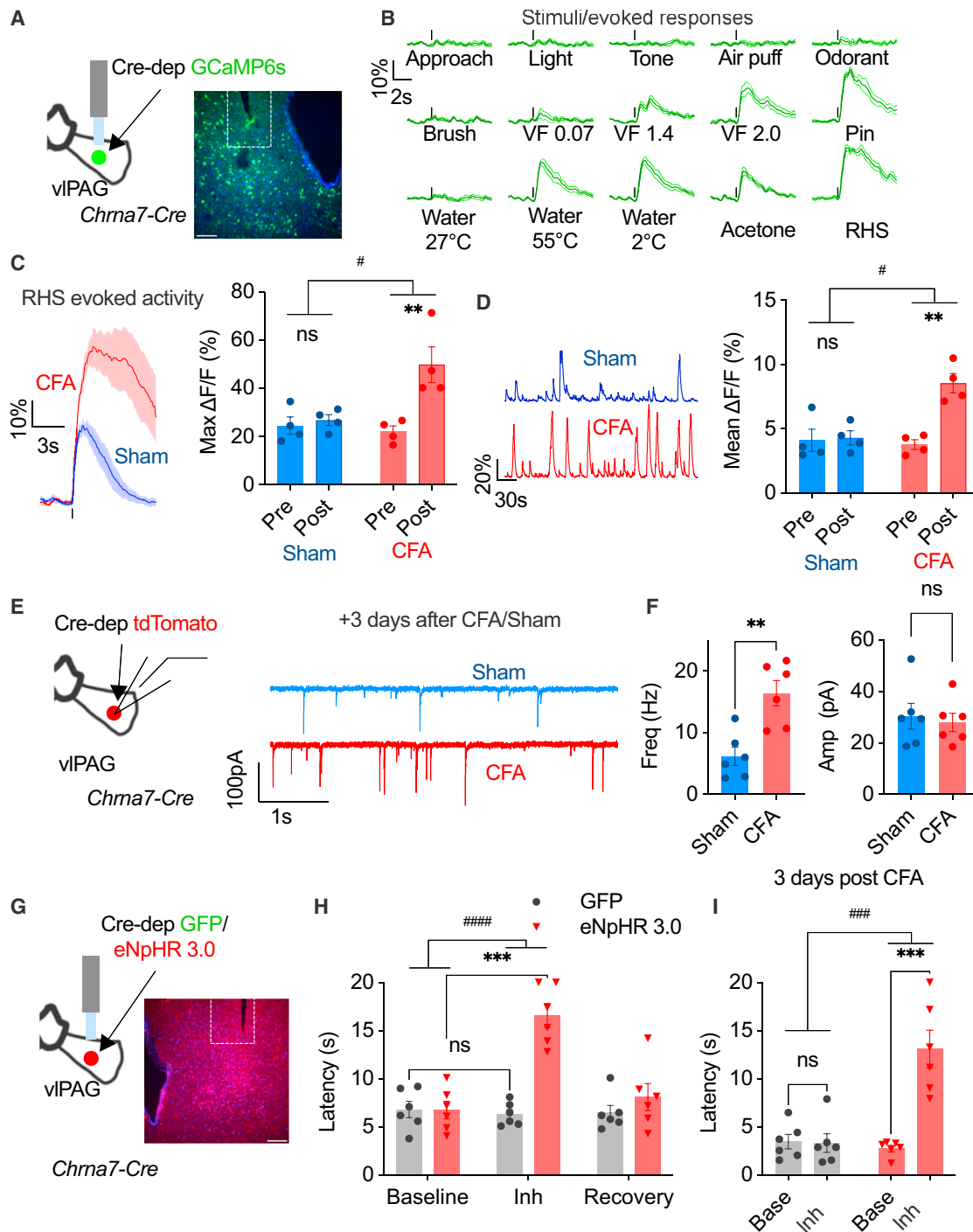
Figure 5. vlPAG$^{Chrna7+}$ neurons are activated by noxious stimuli, and inhibiting them is antinociceptive

(A) Left: schematic depicting GCaMP6 expression in vlPAG$^{Chrna7+}$ neurons and cannula placement (white dashed line) within vlPAG. Right: fluorescence image showing GCaMP6 (green) expression and nuclear DAPI (blue; scale bars, 50 μm).

(B) Mean vlPAG$^{Chrna7+}$ GCaMP6 fluorescence traces time locked (vertical line) to stimuli (approach, light, tone, air puff, odorant) or behavioral responses to von Frey (VF), water at 27°C, 55°C, or 4°C, acetone, or RHS assay (n = 4 mice for air puff/odorant, n = 8 mice for other tests).

(C) Left: mean vlPAG$^{Chrna7+}$ GCaMP6 fluorescence transient time locked to paw withdrawal (vertical line) in RHS assay in sham (blue) and CFA-injected mice (red) (n = 4 mice). Recordings were conducted 3 days after the CFA injection. Right: maximum vlPAG$^{Chrna7+}$ GCaMP6 fluorescence in RHS assay. n = 4 mice. **p < 0.01 paired t test, #p < 0.05 interaction RM two-way ANOVA.

cholinergic drive on these neurons. In a *ChAT-Cre::Chrna7-Cre* mouse line, we expressed ChrimsonR in PPTg^{ChAT+} neurons and GCaMP6 in vlPAG$^{Chrna7+}$ neurons and conducted simultaneous optogenetics and fiber photometry (Figure 6A). Activating PPTg^{ChAT+} terminals in the vlPAG increased latency to paw flick and correlated with a decrease in fluorescence intensity, indicating the inhibition of vlPAG$^{Chrna7+}$ neurons (Figures 6B and 6C). The maximal increase in latency to paw flick was observed during the lowest activity of vlPAG$^{Chrna7+}$ neurons (Figure 6C). Activation of PPTg^{ChAT+} terminals transiently increased activity, followed by inhibition that took ~15 min to develop, suggesting potential cell signaling after α7 nAChR activation. Given that stimulating cholinergic inputs suppressed vlPAG$^{Chrna7+}$ neuronal activity and was antinociceptive, we tested the analgesic effects of the α7 nAChR agonist, EVP-6124.[74] In acute RHS assay, pretreatment with EVP-6124 (0.3 mg/kg) increased paw withdrawal latency (Figure 6D). This analgesic effect peaked 25–45 min after EVP-6124 administration and persisted for several hours (data not shown). Using *in vivo* fiber photometry, we also verified that EVP-6124 at analgesic doses transiently activated vlPAG$^{Chrna7+}$ neurons but was followed by persistent inhibition (Figures 6E and 6F). To test the necessity of this decrease in activity for the antinociceptive effects of EVP-6124, we expressed ChrimsonR and GCaMP6 on vlPAG$^{Chrna7+}$ neurons to activate and monitor these neurons (Figure 6G). After EVP-6124 administration, optogenetic activation of vlPAG$^{Chrna7+}$ neurons blocked the analgesic effects of the agonist in a stimulation frequency-dependent manner (Figures 6H and 6I). These observations demonstrate that a decrease in the activity of vlPAG$^{Chrna7+}$ neurons is an essential substrate for the analgesic effects of α7 nAChR activation.

To explain α7 nAChR activation-induced decrease in activity, we explored potential cell signaling mechanisms. Activation of α7 nAChRs[75] leads to increases in intracellular Ca^{2+} through voltage-gated Ca^{2+} entry and direct permeation through the α7 channels. Increased cytosolic Ca^{2+} can recruit N-acyl phosphatidyl-ethanolamine-specific phospholipase D (NAPE-PLD)-dependent signaling.[76–78] Interestingly, NAPE-PLD levels are dynamically regulated by pain states as well, where, generally, chronic pain conditions decrease NAPE-PLD levels.[79–81] We tested if α7 nAChR activation alters NAPE-PLD in the vlPAG by injecting mice with EVP-6124 (0.3 mg/kg) or saline, followed by a formalin assay. We observed significant upregulation of NAPE-PLD in the vlPAG (Figure S4A). NAPE-PLD recruits endo-

cannabinoid-like signaling molecules to target the nuclear receptor-peroxisome proliferator-activated receptor α (PPARα),[82] which, along with fatty acid amide hydrolase (FAAH), is also implicated in altered algesia.[83–87] We explored if PPARα signaling is an essential substrate for α7 nAChR activation-induced decrease in activity. To that end, we fluorescently labeled vlPAG$^{Chrna7+}$ neurons and conducted cell-attached recordings (Figure 6J). EVP-6124 (2 nM) perfusion reduced the spontaneous firing rate (Figures 6K and 6L), as observed *in vivo* (Figures 6E and 6F). Preincubation with a PPARα antagonist, GW 6471 (1 μM), blocked EVP-6124 (2 nM)-mediated decrease in firing rate without altering baseline activity (Figures 6K and 6L) or α7 nAChR function (Figure S4D).

Although PPARα provides a nexus for the delayed inhibitory effects of α7 nAChR activation, the mechanism regulating membrane excitability is unknown. PPARα activators phosphorylate 5' adenosine monophosphate-activated protein kinase (AMPK), a key regulator of K$_v$2.1.[88] Both AMPK and K$_v$2.1 are implicated in nociception,[89–95] opioid use,[96–99] and regulating neuronal excitability.[100–102] Thus, we explored the phosphorylation of AMPK and various phosphorylation sites of K$_v$2.1 (S563, S603). Following EVP-6124 administration, we observed an increase in pAMPK (Thr172) and a decrease in pK$_v$2.1 (S603, Figures S4B and S4C). Decreased pK$_v$2.1 (S603) increases K$^+$ conductance to reduce excitability.[102] EVP-6124 treatment reduced both nocifensive behaviors in the formalin assay and the levels of pK$_v$2.1 (S603) (Figure S4C). Immunohistochemical signal at the S563 site did not show appreciable differences with EVP-6124 treatment (data not shown). These observations highlight a novel relationship between α7 nAChRs and potassium channels mediated through Ca^{2+}-dependent signaling cascades.

Given these observations, we tested if blocking PPARα lowers the analgesic effects of α7 nAChR agonist. Indeed, the analgesic effects of EVP-6124 (0.3 mg/kg) in phase 2 of the formalin assay were reduced after pre-administration of GW 6471 (2 mg/kg, Figure 6M). As endocannabinoid-like signaling associated with PPAR activation may recruit CB1 receptors, we tested if cannabinoid type-1 receptor (CB1R) antagonist NESS-0327 blocked the analgesic effects of α7 nAChR activation. Analgesic effects of EVP-6124 were not altered by CB1R antagonist NESS-0327 (0.5 mg/kg, Figure 6M). These observations suggest that α7 nAChRs agonist relieves pain by inhibiting the activity of vlPAG$^{Chrna7+}$

(D) Left: representative vlPAG$^{Chrna7+}$ GCaMP6 fluorescence traces during open-field behavior in CFA-injected (red) and sham-control (blue) mice. Right: mean fluorescence in sham-control (blue) and CFA-injected (red) mice. n = 4 mice. **p < 0.01 paired t test, #p < 0.05 interaction RM two-way ANOVA.

(E) Left: slice electrophysiology schematic showing recordings conducted from fluorescently labeled vlPAG$^{Chrna7+}$ neurons using Cre-dependent tdTomato expression in *Chrna7-Cre* mice. Right: representative spontaneous EPSC recordings from CFA-injected and sham-control animals 3 days after injection (−70 mV, Cl$^-$ reversal to −70 mV, Cs$^+$ internal).

(F) Frequency and amplitude of oEPSCs recorded from vlPAG$^{Chrna7+}$ neurons from mice 3 days after CFA or sham injections. n = 6 cells, 5 mice. **p < 0.01 unpaired t test.

(G) Left: schematic showing *Cre*-dependent eNpHR3.0 (or GFP) expression in vlPAG$^{Chrna7+}$ neurons and cannula placement in the vlPAG. Right: fluorescence image showing eNpHR3.0-mCherry (red) expression with DAPI stain (blue; scale bars, 50 μm).

(H) Paw withdrawal latency in RHS assay during baseline, optogenetic inhibition (Inh), and recovery in eNpHR 3.0 (red) and GFP-expressing mice (gray). n = 6 mice. ***p < 0.001 paired t test, ####p < 0.0001 interaction RM two-way ANOVA.

(I) Paw withdrawal latency in RHS assay in CFA-injected mice during baseline (Base) and optogenetic inhibition (Inh) in eNpHR 3.0 (red) and GFP-expressing mice (gray). n = 6 mice. ***p < 0.001 paired t test, ###p < 0.001 interaction RM two-way ANOVA.
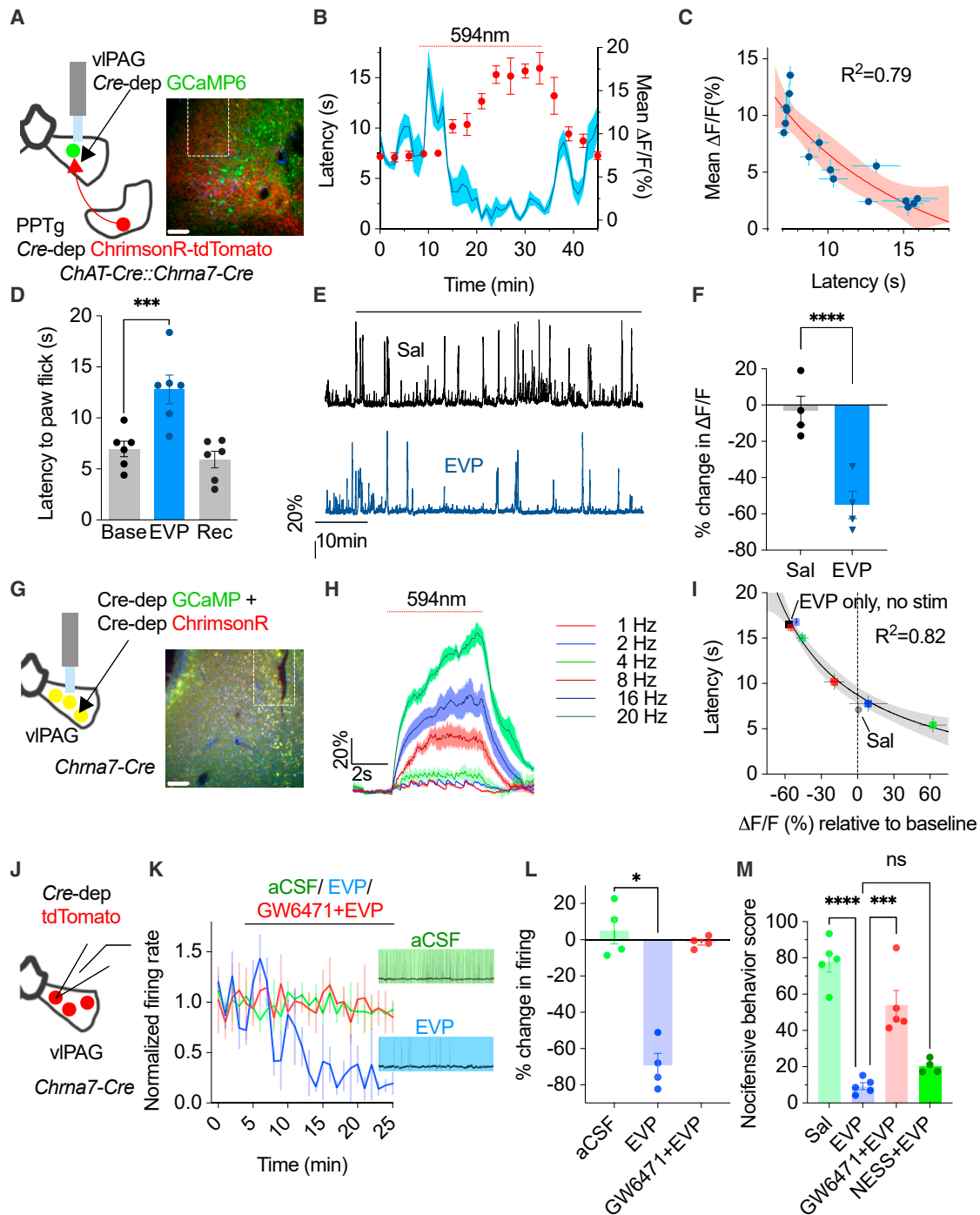
Error bars and shaded areas represent SEM.

Figure 6. α7 nAChR activation is antinociceptive via inhibition of vlPAG^Chrna7+ neurons

(A) Left: schematic of simultaneous fiber photometry and optogenetics strategy to activate PPTg^ChAT+ terminals while monitoring vlPAG^Chrna7+ neuronal activity using GCaMP6 and double transgenic *ChAT-Cre x Chrna7-Cre* mouse line. Right: fluorescence image showing GcaMP6 expression on vlPAG^Chrna7+ neurons (green) and ChrimsonR-tdTomato expression on PPTg^ChAT+ terminals (red; scale bars, 50 μm).

(B) Paw withdrawal latency in RHS assay on the left y axis (red). Mean GcaMP6 vlPAG^Chrna7+ fluorescence during 1 min time bins is plotted on the right y axis (blue). 20 Hz activation of PPTg^ChAT+ terminals in the red line. n = 4 mice.

(C) Mean GCaMP6 vlPAG^Chrna7+ fluorescence plotted against latency in RHS assay. Symbols represent 3 min bins. Fit illustrates inverse correlation and 95% confidence interval (CI, shaded area). n = 4 mice.

(D) Paw withdrawal latency in RHS assay during baseline, after EVP-6124 (0.3 mg/kg) administration, and recovery. n = 6 mice. ***p < 0.001 paired t test.

(legend continued on next page)

neurons through a PPARα-dependent signaling mechanism (Figure S4E).[78,87,103,104]

α7 nAChRs are expressed on vlPAG[GABA+] interneurons and relieve pain via disinhibition of descending pain control pathways

We further investigated the role of vlPAG[Chrna7+] neurons in the context of descending projections. First, we explored the mRNA expression profile of vlPAG[Chrna7+] neurons using FISH. We identified that a majority of vlPAG[Chrna7+] neurons expressed the vesicular GABA transporter (vGAT; Slc32a1+), a marker of GABAergic neurons (Figures S5A and S5B). These vlPAG[Chrna7+] neurons co-expressed markers for other neuromodulators and receptors, including cannabinoid receptor 1 (Cnr1), prodynorphin (Pdyn), and μ-opioid receptor (Oprm1, explored later, Figures S5A–S5C). Using optogenetics and slice electrophysiology, we tested whether vlPAG[Chrna7+] neurons function as local interneurons. Optogenetic activation of vlPAG[Chrna7+] neurons evoked outward currents (optically evoked inhibitory postsynaptic currents [oIPSCs]) in the neighboring recorded cells (Figure 7A), and these oIPSCs were blocked by pretreatment with the GABA-A receptor antagonist, bicuculline (20 μM, Figure 7B). Additionally, activating vlPAG[Chrna7+] neurons inhibited vlPAG → RVM projections in vivo as measured using simultaneous optogenetics and fiber photometry (Figures 7C and 7D). These observations suggest that vlPAG[Chrna7+] neurons are local inhibitory interneurons that regulate vlPAG → RVM projections. Thus, we tested if α7 nAChR activation relieves pain by disinhibiting descending vlPAG → RVM projections. Using slice electrophysiology, we observed that bath application of EVP-6124 (2 nM) decreased the frequency of spontaneous IPSCs recorded from back-labeled vlPAG → RVM projection neurons (Figures 7E and 7F). Additionally, only 6% of vlPAG[Chrna7+] neurons project to RVM (Figures 7G and 7H). Furthermore, activating vlPAG[Chrna7+] → RVM neurons did not alter nocifensive behaviors (Figure 7I). Finally, in vivo administration of EVP-6124 (0.3 mg/kg) decreased GABA levels within vlPAG as measured using iGABASnFR[105] and fiber photometry, similar to the effects of morphine (Figures 7J and 7K). Together, these findings demonstrate that α7 nAChR activation inhibits vlPAG[Chrna7+] neurons to disinhibit the descending pain pathways, similar to the physiological effects of opioids.[37]

α7 nAChR agonist inhibits pain- and opioid-sensitive neurons in the vlPAG

Given the observed similarities in the physiological and behavioral effects of α7 nAChR and μ-opioid receptor agonist, we explored overlap in receptor expression in the vlPAG. Using FISH and protein assays, we found co-expression in 71%–74% of the neurons that expressed at least one of these receptor types (Figures S6A–S6D). Thus, we tested whether the opioid-sensitive pain-encoding vlPAG neuronal ensemble could be effectively targeted by the α7 nAChRs agonist (EVP-6124) to relieve pain, even after opioid tolerance. To that end, we used an in vivo 2-photon imaging approach to monitor neuronal ensemble dynamics over multiple days in the progression to a chronic pain state and through the development of opioid tolerance. Pan-neuronal GCaMP6 was expressed in the vlPAG, and neurons were imaged through a gradient index (GRIN) lens (Figure 8A). After habituation, mice were tested over 4 weeks, where the consistently tracked neurons were analyzed for spontaneous and pain-evoked activity (Figures 8B and 8C). A majority of the monitored vlPAG neurons were activated by noxious stimuli that elicited nocifensive behaviors (Figure 8F; Figures 6E and 6F). Furthermore, morphine (10 mg/kg) reduced both the spontaneous and pain-evoked activity of these vlPAG neurons (Figures 7D–7G). Establishing a chronic neuropathic pain state using paclitaxel (8 mg/kg, four injections over 8 days) induced thermal hyperalgesia (Figure 6G) and hyperexcitability in these vlPAG neurons (Figures 8D–8G). Interestingly, the chronic pain state also recruited neurons that were previously unresponsive to noxious stimuli into the pain-responsive ensemble (Figures S6E and S6F). In this chronic pain state, morphine still inhibited the pain-responsive ensemble, including those newly recruited pain-responsive cells (Figures 8D–8H). However, inducing opioid tolerance weakened the morphine-mediated suppression of activity (Figures 8D–8G). In agreement with our previous optogenetic testing in opioid-tolerant mice, subsequent exposure to EVP-6124 (0.3 mg/kg) effectively inhibited the pain-responsive ensemble (Figures 8D–8H) and increased latency to paw withdrawal (Figure S6G). Interestingly, the majority of neurons inhibited by morphine before inducing opioid

(E) Representative vlPAG[Chrna7+] neuronal activity measured using GCaMP6 and fiber photometry after saline (black) and EVP-6124 (blue) administration (horizontal line).

(F) Percent change in mean fluorescence after saline or EVP-6124 administration. n = 4 mice.

(G) Left: schematic to activate and monitor vlPAG[Chrna7+] neurons. Right: fluorescence images showing GCaMP6 (green) and ChrimsonR-tdTomato (red) expression (scale bars, 50 μm). ****p < 0.001 paired t test.

(H) Optogenetic activation of vlPAG[Chrna7+] neurons (1–20 Hz) and GCaMP6 fluorescence. GCaMP6 and ChrimsonR were expressed on vlPAG[Chrna7+] neurons to monitor and manipulate their activity (n = 4 mice).

(I) Paw withdrawal latency in RHS assay vs. change in vlPAG[Chrna7+] GCaMP6 fluorescence relative to baseline activity. Saline is gray circle. EVP-6124 (0.3 mg/kg) only is black square. Optogenetic activation of vlPAG[Chrna7+] neurons after EVP-6124 is denoted by different colors. Fit illustrates inverse correlation and 95% confidence interval (CI, shaded area) n = 4 mice.

(J) Schematic of slice electrophysiology from fluorescently labeled vlPAG[Chrna7+] neurons.

(K) On-cell recordings of vlPAG[Chrna7+] neurons during drug perfusions (EVP-6124, 2 nM; GW6471, 1 μM). Insets show representative traces during 20–25 min after artificial cerebrospinal fluid (aCSF) (green) and EVP-6124 (blue). n = 4 cells from 3 mice.

(L) Change in firing relative to baseline. n = 4 cells from 3 mice. *p < 0.05 unpaired t test.

(M) Nocifensive behavior score (%) during phase 2 of formalin assay after administration of Sal (light green, n = 5 mice), EVP-6124 (blue, n = 5 mice), and EVP administered after GW6471 pre-infusion (red, n = 5 mice) and after NESS0327 (dark green, n = 4 mice). ***p < 0.001 ****p < 0.0001 unpaired t test.

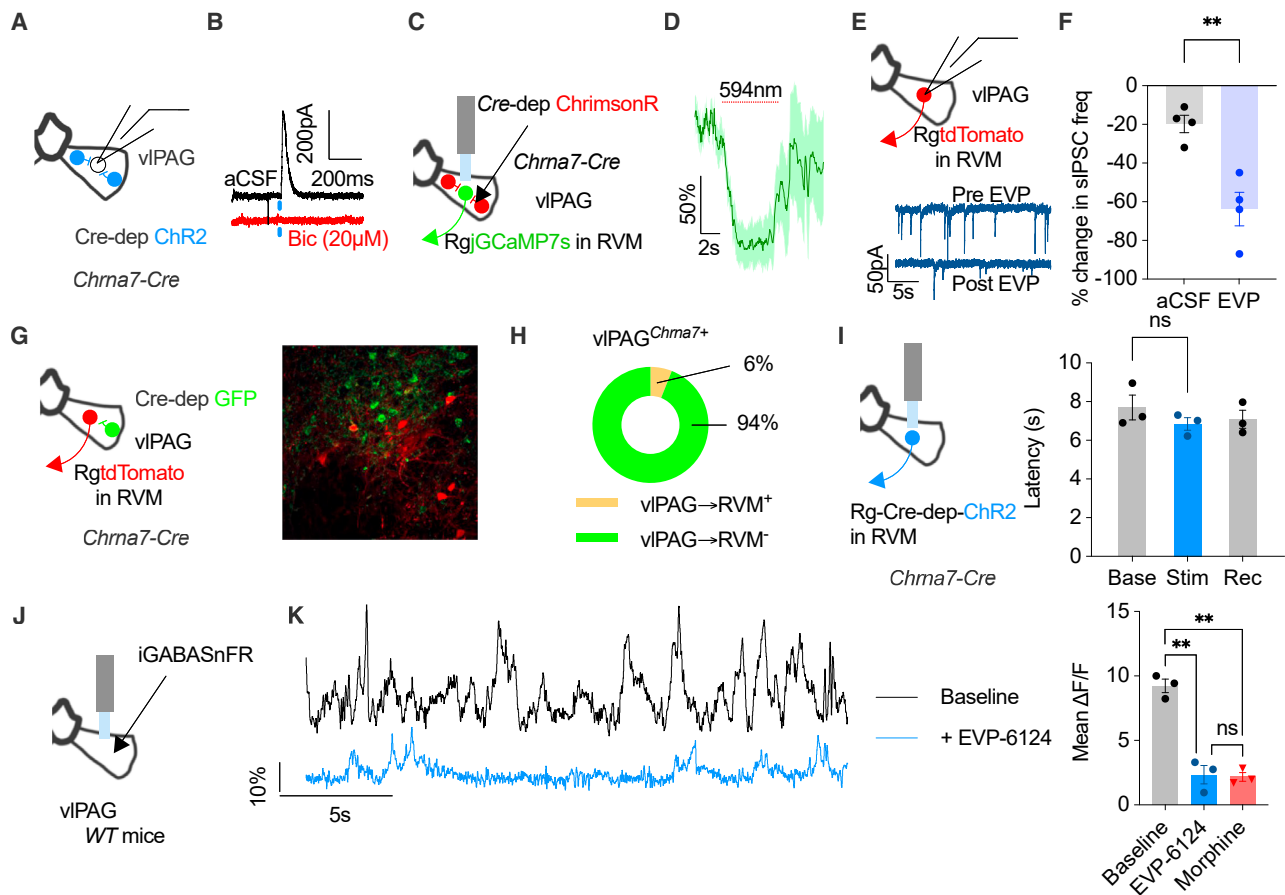Error bars and shaded areas represent SEM.

Figure 7. α7 nAChRs are expressed on GABAergic vlPAG neurons, which inhibit vlPAG → RVM neurons

(A) Slice electrophysiology schematic. vlPAG$^{Chrna7+}$ neurons were optogenetically activated while neighboring unlabeled neurons were recorded (0 mV, $E_{Cl^-} \sim -70$ mV).

(B) Optically evoked inhibitory postsynaptic current (IPSC) blocked by bath application of bicuculline (20 μM).

(C) Schematic depicting strategy to activate vlPAG$^{Chrna7+}$ neurons using ChrimsonR while monitoring vlPAG → RVM projection neurons using GCaMP7s.

(D) Mean GCaMP7s fluorescence from vlPAG → RVM projection neurons (green trace) collected using fiber photometry time locked to optogenetic activation of vlPAG$^{Chrna7+}$ neurons (red line, 4 traces per animal, n = 3 mice).

(E) Top: schematic depicting retrograde tdTomato labeling of vlPAG → RVM projection neurons for slice electrophysiology. Bottom: spontaneous IPSCs before (above) and after (below) EVP-6124 bath application. Neurons were voltage clamped at −70 mV with $E_{Cl^-} \sim 0$ mV and CNQX (20 μM) in the bath.

(F) Percent change in the frequency of spontaneous IPSCs 2–5 min before aCSF/EVP-6124 (2 nM) application and 15–20 min after aCSF (gray)/EVP (blue) bath application. n = 4 cells from 3 mice. **p < 0.01 unpaired t test.

(G) Left: schematic depicting retrograde tdTomato labeling of vlPAG → RVM projection neurons (red) and GFP labeling of vlPAG$^{Chrna7+}$ neurons (green). Right: representative image showing fluorescently labeled vlPAG neurons (scale bars, 50 μm).

(H) Pie chart showing the percentage of vlPAG$^{Chrna7+}$ neurons that project to RVM. A total of 2,202 cells were counted from 3 mice.

(I) Left: schematic showing the optogenetic strategy to selectively activate vlPAG$^{Chrna7+}$ → RVM projection neurons. Right: latency in RHS assay during baseline, optogenetic stimulation (blue), and recovery. n = 3 mice.

(J) Schematic showing fiber photometry strategy to monitor GABA levels within the vlPAG.

(K) Left: representative iGABASnFR fluorescence in baseline (black) and post-EVP-6124 administration (blue). Right: mean fluorescence in baseline (black), EVP-6124 (blue), and morphine (red) injected animals. n = 3 mice. **p < 0.01 unpaired t test.

Error bars and shaded areas represent SEM.

tolerance were also inhibited by EVP-6124 (Figure 8H). These observations demonstrate that chronic pain expands the pain-sensitive vlPAG neuronal ensemble. Additionally, α7 nAChRs and μ-opioid receptors inhibit similar ensembles of neurons, and α7 nAChR activation still inhibits these neurons after opioid tolerance.

α7 nAChR agonists relieve pain without the development of tolerance, rewarding effects, or withdrawal symptoms

In addition to the analgesic effects of EVP-6124, we tested for the development of analgesic tolerance. Even after repeated administration (6 days, 2×/day), EVP-6124 (0.3 mg/kg)
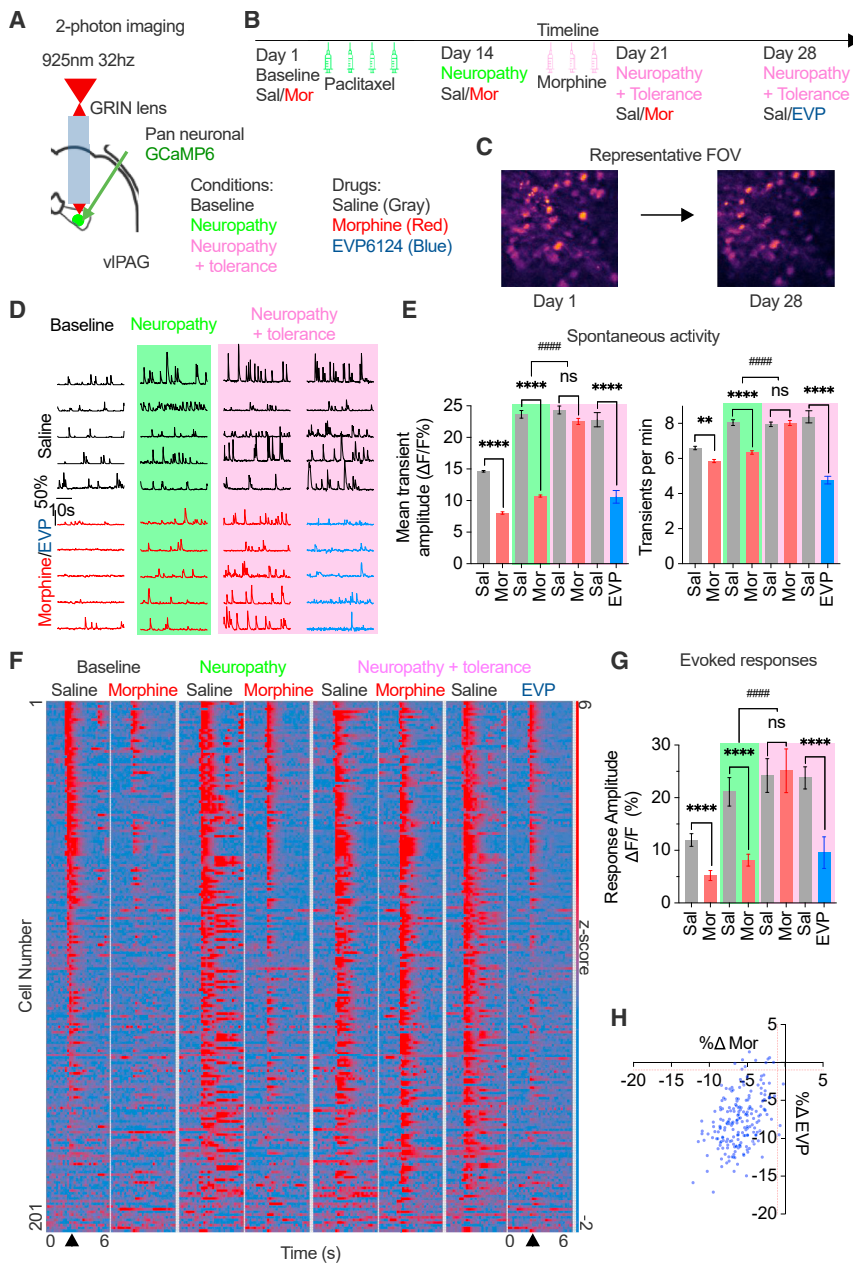
Figure 8. α7 nAChR agonist inhibits pain-responsive and opioid-sensitive ensembles

(A) Schematic showing 2-photon imaging strategy using GCaMP6 expressed in vlPAG neurons and GRIN lens implanted within vlPAG to monitor neuronal activity in head-fixed awake-behaving animals.

(B) Timeline: spontaneous and noxious-stimuli evoked activity was tracked after saline, morphine, or EVP-6124 administration. On day 2 to 7, mice underwent paclitaxel-induced neuropathy. On day 14 to 21, mice underwent opioid tolerance.

(C) Representative field of view (FOV) showing standard deviation fluorescence image reflecting active neurons during imaging sessions on day 1 and 28.

(D) Representative activity traces tracked through pathophysiological states (baseline, neuropathy [green], and opioid tolerance [pink]) and drug exposures: saline (black), morphine (red, 10 mg/kg), and EVP-6124 (blue, 0.3 mg/kg).

(E) Quantification of spontaneous activity (n = 201 neurons, 5 mice). Left, mean amplitude of transients. Right, mean transient frequency under baseline, neuropathy, tolerance, and EVP-6124 administration (4). Metrics post saline, morphine, and EVP-6124 administration are represented as gray, red, and blue, respectively.

(F) Raster plots of neuronal activity in the vlPAG during noxious heat-evoked tail withdrawal (arrow). Warmer colors represent stronger activation. n = 201 neurons, 5 mice.

(G) Evoked response amplitude after saline, morphine, and EVP-6124 during baseline, neuropathy, and after opioid tolerance and EVP-6124 administration. Metrics post saline, morphine, and EVP-6124 administration are represented as gray, red, and blue, respectively. n = 201 neurons, 5 mice.

(H) Percent reduction in noxious-stimuli-evoked neuronal response amplitude after morphine (x axis) and EVP-6124 (y axis). ****$p < 0.0001$ paired t test, ####$p < 0.0001$ interaction RM two-way ANOVA. Error bars represent SEM.

pre-exposed to morphine, EVP-6124-treated mice did not show an aversion to the MLA-paired chamber (Figure S7E). These data indicate that analgesic doses of the α7 agonist did not induce tolerance, reward, or withdrawal symptoms.

increased the latency to paw flick (Figure S7A). Next, we explored the reward profile associated with EVP-6124 using a conditioned place preference (CPP) assay (Figure S7B). Here, we observed that unlike morphine, exposure to an analgesic dose of EVP-6124 (0.3 mg/kg) in a particular context did not cause a preference for that context, similar to previous observations[106] (Figure S7C). Next, to test for affective withdrawal symptoms, we repeatedly exposed mice to EVP-6124 or morphine over 5 days and then conducted a conditioned place aversion assay where we precipitated withdrawal using their respective antagonists: MLA (3 mg/kg) or naloxone (6 mg/kg) (Figure S7D). Although the naloxone-paired chamber was avoided by animals

In addition to acute and chronic neuropathic pain, we tested if α7 nAChR agonist treatment relieved formalin-induced tonic inflammatory pain. EVP-6124 decreased the duration of nocifensive behaviors in phase 2 of the formalin assay to similar levels as that of morphine (Figures S7F and S7G). Furthermore, a different α7 nAChR agonist (PHA-543613, 10 mg/kg) and a positive allosteric modulator (PAM; PNU-120596, 10 mg/kg) yielded antinociceptive effects similar to EVP-6124, in agreement with previous studies[46,107] (Figure S7G). As the PAM requires endogenous ACh to achieve receptor activation and behavioral analgesic effects, these data complement our earlier results (Figure 1).

Clinically, drug combinations are often employed to limit opioid use. To test if α7 nAChR agonists could augment the analgesic effects of submaximal doses of morphine, we co-administered EVP-6124 (0.1 mg/kg) and morphine (4 mg/kg). Combined submaximal doses decreased nocifensive behaviors in a formalin assay (Figure S7H) with a magnitude similar to morphine at a 10 mg/kg dose, i.p. (Figure S7G). This combination was associated with less dissociative locomotor behavior,[108–110] which is commonly observed with analgesic morphine doses. EVP-6124 also decreased formalin-induced nocifensive behaviors in opioid-tolerant mice, even after naloxone treatment (6 mg/kg, Figure S7I). Finally, EVP-6124 also relieved the affective component of tonic inflammatory pain, as tested using CPP (Figure S7J). Together, these observations indicate that α7 nAChR agonists relieve pain and, along with the endogenous cholinergic circuit, form a viable avenue for pain treatment without evidence of adverse side effects or addiction liability.

DISCUSSION

Chronic pain states are encoded in multiple brain regions at cellular and network levels through synaptic and intrinsic excitability mechanisms.[111–115] Within these networks, the vlPAG serves as a critical nexus that modulates pain by integrating and processing information from functionally diverse brain areas.[116–122] Manipulating vlPAG neuronal activity has analgesic effects,[14,16–36] predominantly through projections to the RVM and locus ceruleus (LC).[38,79] How chronic pain and opioid exposure alter the physiology of pain-encoding ensembles, specifically within the vlPAG, has not been thoroughly explored.[13] To expand our understanding of neuromodulation in the vlPAG, particularly cholinergic modulation, we investigated endogenous ACh levels in vlPAG in various pain states and established an inverse relationship between these phenomena. We then determined that α7 AChRs and their signaling pathway reverse the pain-induced maladaptive hyperexcitability in neuronal ensembles of the vlPAG. We also show that the analgesic potency of descending pain control circuits is preserved after opioid tolerance. We show that ACh strongly modulates vlPAG excitability to alter sensory and affective pain experiences. This cholinergic modulation originates from synaptic inputs and ultimately alters the intrinsic excitability of pain-encoding neuronal ensembles. These observations deepen our understanding of pain control circuits and point toward molecular and cellular targets for identifying non-opioid pain treatment strategies.

Analgesic effects of opioids are mediated through multiple central and peripheral circuits. One important site of action is the vlPAG, where μ-opioid receptors inhibit GABAergic interneurons to disinhibit vlPAG output neurons.[37] Repeated opioid use leads to analgesic tolerance[2–6] and opioid-induced hyperalgesia through multiple maladaptive changes.[2–6] Neural adaptations associated with opioid tolerance may include changes in G protein and β-arrestin coupling to intracellular signaling pathways[60,123,124] and altered recruitment of G protein-coupled inwardly rectifying potassium (GIRK) channels within the vlPAG.[125–127] These foundational studies suggested that vlPAG-mediated pain modulation by other means could be compromised under opioid-tolerant conditions. We observed that a subset of vlPAG neurons was inhibited by morphine administration, and these effects were lost under opioid-tolerant conditions. Notably, after opioid tolerance, we found that direct somatic inhibition of vlPAG^{Oprm1+} neurons can still relieve pain, suggesting that the analgesic efficacy of these descending pain control circuits is preserved, independent of previous opioid treatments.

These investigations yielded unexpected observations regarding cholinergic physiology. First, we did not expect painful experiences to decrease ACh levels in the vlPAG, as salient stimuli typically *increase* ACh release.[41,128] Very few studies have identified a physiological role for decreases in ACh,[129] suggesting an unexplored but potentially important role of the baseline cholinergic tone. Our data demonstrate that decreases in basal cholinergic tone in vlPAG are correlated with pain, suggesting that basal levels help set an equilibrium level of algesia. Second, cholinergic signaling in the CNS is enigmatic, partially due to the uncertain nature of cholinergic synaptic transmission: both bulk volume transmission through diffuse axonal arborizations and fast synaptic transmission have been proposed.[41,63–65] These difficulties also stem from the kinetics of AChRs, the rapid hydrolysis of ACh, and its dominant effects on presynaptic terminals as opposed to somatodendritic sites.[43] Additionally, multiple cholinergic projections co-release other neurotransmitters.[43,130,131] Methodological innovations employed here have addressed these challenges. Using cell-type and projection-specific optogenetic approaches with slice electrophysiology, we demonstrate fast cholinergic synaptic transmission as a mediator of ACh modulation, which is uncommon in the CNS. Our use of a fluorescent ACh sensor allowed direct monitoring of ACh release dynamics during baseline conditions, as well as acute and chronic pain states. Importantly, increasing ACh levels using optogenetics relieves both acute and chronic pain. Third, our studies focused on PPTg inputs to vlPAG, but we also found anatomical connections between LDTg and MS-DBB. Although connectivity does not prove functional relevance, exploring these inputs is an important area for future investigation. Given the known functions of LDTg and MS-DBB in REM sleep[132–134] and fear encoding,[135–137] examining the contribution of these projections to the vlPAG in those conditions could provide valuable insights. Cholinergic neurons in the basal forebrain also regulate attention and cognitive functions,[39,138–140] and evaluating vlPAG contribution to attentional-analgesia[141,142] or placebo-analgesia[143–145] could reveal underlying mechanisms. Intriguingly, chronic pain conditions like diabetic neuropathies are associated with cognitive comorbidities like ADHD,[146] and exploring the potential role of vlPAG cholinergic tone in these conditions could present novel treatment strategies.

Our experiments indicate that the pain-relieving effects of increasing ACh levels are mediated through α7 nAChRs that inhibit vlPAG$^{Oprm1+/GABA+}$ interneurons. Recent studies have reported that inhibiting vlPAG^{GABA+} interneurons reduces acute pain.[14,34] Similarly, we found that inhibiting vlPAG$^{Chrna7+}$ neurons relieves the chronic and affective components of pain. Interestingly, decreasing the activity of these interneurons also reduces the behavioral symptoms of opioid withdrawal. Optogenetic activation of vlPAG$^{Chrna7+}$ interneurons at higher frequencies

reverses the inhibitory effects of α7 nAChR agonist administration. These data suggest that vlPAG^{GABA+} interneurons are tonically active, which means that vlPAG projection neurons are continuously inhibited under baseline conditions. These results were cross-verified by our *ex vivo* cell-attached recordings showing spontaneous activity. Others have shown that vlPAG^{GABA+} neurons undergo hyperexcitability under pain states,[147–150] mirroring our observations of vlPAG$^{Chrna7+}$ interneurons. Our lab and others have reported analgesic actions of α7 nAChR agonists through central mechanisms.[46,151–154] Our previous study suggested that α7 nAChRs were expressed by a subpopulation of vlPAG → RVM projection neurons that lack μ-opioid receptors. Here, we expanded our assessment and found that α7 nAChRs are expressed predominantly on local interneurons, where they inhibit these cells, leading to the activation of vlPAG → RVM projection neurons in a manner similar to opioid receptors.[37,148] Furthermore, aided by complementary and rigorous genetic, mRNA, protein, and physiological measures, we observed a high degree of overlap in the expression and function of μ-opioid and α7 nAChRs. Our molecular profiling also explored the overlap of α7 nAChRs with multiple molecular markers of vlPAG neurons. In the vlPAG, *Tac1*$^+$ and *Sst*$^+$ neurons modulate itch rather than pain,[155] and we did not observe α7 nAChR expression on those neurons. Although we attribute the analgesic effects of activating PPTg^{ChAT+} → vlPAG to α7 nAChRs, M2 mAChRs are also strongly expressed in the vlPAG.[156] Our testing of muscarinic antagonists suggests that M2 mAChRs may contribute to baseline pain sensitivity and thus may contribute to the onset of chronic pain physiology. Given the higher affinity of M2 mAChR to ACh, perhaps the decrease in ACh release in the vlPAG may be *sensed* by these receptors during acute and chronic pain states.[157,158] Further exploration of M2 mAChRs in vlPAG is needed to better understand the adaptations associated with chronic pain.

Another unexpected outcome of our investigations was that α7 nAChRs relieve pain through a persistent *inhibition* of neuronal activity. This effect was surprising given that α7 nAChRs are excitatory cation channels with high Ca^{2+} permeability, displaying rapid activation and desensitization kinetics.[75] Increasingly, investigations of Ca^{2+}-permeable receptors, like NMDA[159–163] and α7 nAChRs, have revealed signaling through non-canonical pathways with physiological responses beyond their ionotropic effects.[164–169] Evidence for metabotropic-like signaling pathways, Erk, Jak2/Stat3, and other kinases has also been reported.[170–172] Elevating intracellular Ca^{2+} through these Ca^{2+}-permeable receptors could induce decreases in neuronal excitability to reduce cytotoxicity.[173–176] In other brain regions, activation of Ca^{2+}-permeable nAChRs can modulate neuronal physiology through phosphorylation,[78,103] calcineurin signaling,[177–179] and activation of K$_{Ca}$ channels.[180,181] We observed strong regulation of K$_v$2.1 phosphorylation by α7 nAChR agonists, likely mediating the decrease in excitability through non-genomic actions of PPARα and AMPK phosphorylation.[100,182–187] Along with this cholinergic modulation, we also observed the expression of CB1Rs on vlPAG$^{Chrna7+}$ neurons. Although CB1R antagonist pretreatment did not alter the analgesic effects of α7 nAChR agonists, intra-vlPAG administration of CB1R modulators can regulate physiology and reduce

pain with minimal rewarding effects or withdrawal symptoms,[34,188–192] closely mimicking our observed analgesic outcomes. Thus, these vlPAG ensembles could serve as a fascinating unexplored nexus where endogenous cholinergic, opioid, and cannabinoid systems converge to regulate nocifensive behaviors.

STAR★METHODS

Detailed methods are provided in the online version of this paper and include the following:

- KEY RESOURCES TABLE
- RESOURCE AVAILABILITY
  - Lead contact
  - Materials availability
  - Data and code availability
- EXPERIMENTAL MODEL AND STUDY PARTICIPANT DETAILS
  - Mouse lines
- METHOD DETAILS
  - Surgeries
  - Slice electrophysiology
  - Optogenetics
  - Fiber photometry
  - *In vivo* calcium imaging
  - Behavior
  - Histology
- QUANTIFICATION AND STATISTICAL ANALYSIS

SUPPLEMENTAL INFORMATION

Supplemental information can be found online at https://doi.org/10.1016/j.neuron.2023.08.017.

AUTHOR CONTRIBUTIONS

Conceptualization, S.S. and D.S.M.; methodology, S.S. and D.S.M.; software, S.S.; validation, S.S. and A.K.; formal analysis, S.S.; investigation, S.S. and A.K.; resources, S.S. and D.S.M.; data curation, S.S.; writing – original draft, S.S.; writing – review and editing, S.S., A.K., and D.S.M.; visualization, S.S.; supervision, D.S.M.; project administration, S.S. and D.S.M.; funding acquisition, S.S. and D.S.M.

DECLARATION OF INTERESTS

The authors declare no competing interests.

REFERENCES

1. Ballantyne, J.C., and Mao, J. (2003). Opioid therapy for chronic pain. N. Engl. J. Med. *349*, 1943–1953. https://doi.org/10.1056/NEJMra025411.

2. Geppetti, P., and Benemei, S. (2009). Pain treatment with opioids: achieving the minimal effective and the minimal interacting dose. Clin. Drug Investig. *29*, 3–16. https://doi.org/10.2165/0044011-200929001-00002.

3. Volkow, N., Benveniste, H., and McLellan, A.T. (2018). Use and misuse of opioids in chronic pain. Annu. Rev. Med. *69*, 451–465. https://doi.org/10.1146/annurev-med-011817-044739.

4. Labianca, R., Sarzi-Puttini, P., Zuccaro, S.M., Cherubino, P., Vellucci, R., and Fornasari, D. (2012). Adverse effects associated with non-opioid and opioid treatment in patients with chronic pain. Clin. Drug Investig. *32*, 53–63. https://doi.org/10.2165/11630080-000000000-00000.

5. Benyamin, R., Trescot, A.M., Datta, S., Buenaventura, R., Adlaka, R., Sehgal, N., Glaser, S.E., and Vallejo, R. (2008). Opioid complications and side effects. Pain Physician *11*, S105–S120.

6. Rosenblum, A., Marsch, L.A., Joseph, H., and Portenoy, R.K. (2008). Opioids and the treatment of chronic pain: controversies, current status, and future directions. Exp. Clin. Psychopharmacol. *16*, 405–416. https://doi.org/10.1037/a0013628.

7. Spagnolo, P.A., and Goldman, D. (2017). Neuromodulation interventions for addictive disorders: challenges, promise, and roadmap for future research. Brain *140*, 1183–1203. https://doi.org/10.1093/brain/aww284.

8. Basbaum, A.I., and Fields, H.L. (1984). Endogenous pain control systems: brainstem spinal pathways and endorphin circuitry. Annu. Rev. Neurosci. *7*, 309–338. https://doi.org/10.1146/annurev.ne.07.030184.001521.

9. Heinricher, M.M. (2016). Pain modulation and the transition from acute to chronic pain. Adv. Exp. Med. Biol. *904*, 105–115. https://doi.org/10.1007/978-94-017-7537-3_8.

10. Heinricher, M.M., Tavares, I., Leith, J.L., and Lumb, B.M. (2009). Descending control of nociception: specificity, recruitment and plasticity. Brain Res. Rev. *60*, 214–225. https://doi.org/10.1016/j.brainresrev.2008.12.009.

11. Fields, H.L., and Heinricher, M.M. (1985). Anatomy and physiology of a nociceptive modulatory system. Philos. Trans. R. Soc. Lond. B Biol. Sci. *308*, 361–374. https://doi.org/10.1098/rstb.1985.0037.

12. Heinricher, M.M., Cheng, Z.F., and Fields, H.L. (1987). Evidence for two classes of nociceptive modulating neurons in the periaqueductal gray. J. Neurosci. *7*, 271–278. https://doi.org/10.1523/JNEUROSCI.07-01-00271.1987.

13. Samineni, V.K., Premkumar, L.S., and Faingold, C.L. (2017). Neuropathic pain-induced enhancement of spontaneous and pain-evoked neuronal activity in the periaqueductal gray that is attenuated by gabapentin. Pain *158*, 1241–1253. https://doi.org/10.1097/j.pain.0000000000000905.

14. Samineni, V.K., Grajales-Reyes, J.G., Copits, B.A., O'Brien, D.E., Trigg, S.L., Gomez, A.M., Bruchas, M.R., and Gereau, R.W. (2017). Divergent modulation of nociception by glutamatergic and GABAergic neuronal subpopulations in the periaqueductal gray. eNeuro *4*, ENEURO.0129-16.2017. https://doi.org/10.1523/ENEURO.0129-16.2017.

15. Fields, H. (2004). State-dependent opioid control of pain. Nat. Rev. Neurosci. *5*, 565–575. https://doi.org/10.1038/nrn1431.

16. Behbehani, M.M. (1995). Functional characteristics of the midbrain periaqueductal gray. Prog. Neurobiol. *46*, 575–605. https://doi.org/10.1016/0301-0082(95)00009-k.

17. Bennett, G.J., and Mayer, D.J. (1979). Inhibition of spinal cord interneurons by narcotic microinjection and focal electrical stimulation in the periaqueductal central gray matter. Brain Res. *172*, 243–257. https://doi.org/10.1016/0006-8993(79)90536-5.

18. Hosobuchi, Y., Adams, J.E., and Linchitz, R. (1977). Pain relief by electrical stimulation of the central gray matter in humans and its reversal by naloxone. Science *197*, 183–186. https://doi.org/10.1126/science.301658.

19. Jones, S.L., and Gebhart, G.F. (1988). Inhibition of spinal nociceptive transmission from the midbrain, pons and medulla in the rat: activation of descending inhibition by morphine, glutamate and electrical stimulation. Brain Res. *460*, 281–296. https://doi.org/10.1016/0006-8993(88)90373-3.

20. Liebeskind, J.C., Guilbaud, G., Besson, J.M., and Oliveras, J.L. (1973). Analgesia from electrical stimulation of the periaqueductal gray matter in the cat: behavioral observations and inhibitory effects on spinal cord interneurons. Brain Res. *50*, 441–446. https://doi.org/10.1016/0006-8993(73)90748-8.

21. Mayer, D.J., and Liebeskind, J.C. (1974). Pain reduction by focal electrical stimulation of the brain: an anatomical and behavioral analysis. Brain Res. *68*, 73–93. https://doi.org/10.1016/0006-8993(74)90534-4.

22. Millan, M.J., Członkowski, A., Millan, M.H., and Herz, A. (1987). Activation of periaqueductal grey pools of beta-endorphin by analgetic electrical stimulation in freely moving rats. Brain Res. *407*, 199–203. https://doi.org/10.1016/0006-8993(87)91239-x.

23. Morgan, M.M., Sohn, J.H., and Liebeskind, J.C. (1989). Stimulation of the periaqueductal gray matter inhibits nociception at the supraspinal as well as spinal level. Brain Res. *502*, 61–66. https://doi.org/10.1016/0006-8993(89)90461-7.

24. Reynolds, D.V. (1969). Surgery in the rat during electrical analgesia induced by focal brain stimulation. Science *164*, 444–445.

25. Sandkühler, J., Willmann, E., and Fu, Q.G. (1989). Blockade of GABAA receptors in the midbrain periaqueductal gray abolishes nociceptive spinal dorsal horn neuronal activity. Eur. J. Pharmacol. *160*, 163–166. https://doi.org/10.1016/0014-2999(89)90667-5.

26. Behbehani, M.M., Jiang, M., Chandler, S.D., and Ennis, M. (1990). The effect of GABA and its antagonists on midbrain periaqueductal gray neurons in the rat. Pain *40*, 195–204. https://doi.org/10.1016/0304-3959(90)90070-T.

27. Carstens, E., Hartung, M., Stelzer, B., and Zimmermann, M. (1990). Suppression of a hind limb flexion withdrawal reflex by microinjection of glutamate or morphine into the periaqueductal gray in the rat. Pain *43*, 105–112. https://doi.org/10.1016/0304-3959(90)90055-l.

28. Carstens, E., Stelzer, B., and Zimmermann, M. (1988). Microinjections of glutamate or morphine at coincident midbrain sites have different effects on nociceptive dorsal horn neurons in the rat. Neurosci. Lett. *95*, 185–191. https://doi.org/10.1016/0304-3940(88)90654-4.

29. Depaulis, A., Morgan, M.M., and Liebeskind, J.C. (1987). GABAergic modulation of the analgesic effects of morphine microinjected in the ventral periaqueductal gray matter of the rat. Brain Res. *436*, 223–228. https://doi.org/10.1016/0006-8993(87)91665-9.

30. Heinricher, M.M., Martenson, M.E., and Neubert, M.J. (2004). Prostaglandin E2 in the midbrain periaqueductal gray produces

hyperalgesia and activates pain-modulating circuitry in the rostral ventro-medial medulla. Pain *110*, 419–426. https://doi.org/10.1016/j.pain.2004.04.026.

31. Jensen, T.S., and Yaksh, T.L. (1989). Comparison of the antinociceptive effect of morphine and glutamate at coincidental sites in the periaqueductal gray and medial medulla in rats. Brain Res. *476*, 1–9. https://doi.org/10.1016/0006-8993(89)91529-1.

32. Pertovaara, A., Wei, H., and Hämäläinen, M.M. (1996). Lidocaine in the rostroventromedial medulla and the periaqueductal gray attenuates allodynia in neuropathic rats. Neurosci. Lett. *218*, 127–130. https://doi.org/10.1016/s0304-3940(96)13136-0.

33. Roychowdhury, S.M., and Fields, H.L. (1996). Endogenous opioids acting at a medullary mu-opioid receptor contribute to the behavioral antinociception produced by GABA antagonism in the midbrain periaqueductal gray. Neuroscience *74*, 863–872. https://doi.org/10.1016/0306-4522(96)00180-7.

34. Zhu, H., Xiang, H.C., Li, H.P., Lin, L.X., Hu, X.F., Zhang, H., Meng, W.Y., Liu, L., Chen, C., Shu, Y., et al. (2019). Inhibition of GABAergic neurons and excitation of glutamatergic neurons in the ventrolateral periaqueductal gray participate in electroacupuncture analgesia mediated by cannabinoid receptor. Front. Neurosci. *13*, 484. https://doi.org/10.3389/fnins.2019.00484.

35. Yang, L., Lu, J., Guo, J., Chen, J., Xiong, F., Wang, X., Chen, L., and Yu, C. (2022). Ventrolateral periaqueductal gray astrocytes regulate nociceptive sensation and emotional motivation in diabetic neuropathic pain. J. Neurosci. *42*, 8184–8199. https://doi.org/10.1523/JNEUROSCI.0920-22.2022.

36. Taylor, N.E., Pei, J., Zhang, J., Vlasov, K.Y., Davis, T., Taylor, E., Weng, F.J., Van Dort, C.J., Solt, K., and Brown, E.N. (2019). The role of glutamatergic and dopaminergic neurons in the periaqueductal gray/dorsal raphe: separating analgesia and anxiety. eNeuro *6*, ENEURO.0018-18.2019. https://doi.org/10.1523/ENEURO.0018-18.2019.

37. Vaughan, C.W., Ingram, S.L., Connor, M.A., and Christie, M.J. (1997). How opioids inhibit GABA-mediated neurotransmission. Nature *390*, 611–614. https://doi.org/10.1038/37610.

38. Kim, J.H., Gangadharan, G., Byun, J., Choi, E.J., Lee, C.J., and Shin, H.S. (2018). Yin-and-yang bifurcation of opioidergic circuits for descending analgesia at the midbrain of the mouse. Proc. Natl. Acad. Sci. USA *115*, 11078–11083. https://doi.org/10.1073/pnas.1806082115.

39. Ballinger, E.C., Ananth, M., Talmage, D.A., and Role, L.W. (2016). Basal forebrain cholinergic circuits and signaling in cognition and cognitive decline. Neuron *91*, 1199–1218. https://doi.org/10.1016/j.neuron.2016.09.006.

40. Luchicchi, A., Bloem, B., Viaña, J.N.M., Mansvelder, H.D., and Role, L.W. (2014). Illuminating the role of cholinergic signaling in circuits of attention and emotionally salient behaviors. Front. Synaptic Neurosci. *6*, 24. https://doi.org/10.3389/fnsyn.2014.00024.

41. Picciotto, M.R., Higley, M.J., and Mineur, Y.S. (2012). Acetylcholine as a neuromodulator: cholinergic signaling shapes nervous system function and behavior. Neuron *76*, 116–129. https://doi.org/10.1016/j.neuron.2012.08.036.

42. Decker, M.W., Brioni, J.D., Bannon, A.W., and Arneric, S.P. (1995). Diversity of neuronal nicotinic acetylcholine receptors: lessons from behavior and implications for CNS therapeutics. Life Sci. *56*, 545–570. https://doi.org/10.1016/0024-3205(94)00488-e.

43. Jiang, L., López-Hernández, G.Y., Lederman, J., Talmage, D.A., and Role, L.W. (2014). Optogenetic studies of nicotinic contributions to cholinergic signaling in the central nervous system. Rev. Neurosci. *25*, 755–771. https://doi.org/10.1515/revneuro-2014-0032.

44. Naser, P.V., and Kuner, R. (2018). Molecular, cellular and circuit basis of cholinergic modulation of pain. Neuroscience *387*, 135–148. https://doi.org/10.1016/j.neuroscience.2017.08.049.

45. Nicolodi, M., Galeotti, N., Ghelardini, C., Bartolini, A., and Sicuteri, F. (2002). Central cholinergic challenging of migraine by testing second-generation anticholinesterase drugs. Headache *42*, 596–602. https://doi.org/10.1046/j.1526-4610.2002.02146.x.

46. Umana, I.C., Daniele, C.A., Miller, B.A., Abburi, C., Gallagher, K., Brown, M.A., Mason, P., and McGehee, D.S. (2017). Nicotinic modulation of descending pain control circuitry. Pain *158*, 1938–1950. https://doi.org/10.1097/j.pain.0000000000000993.

47. Umana, I.C., Daniele, C.A., and McGehee, D.S. (2013). Neuronal nicotinic receptors as analgesic targets: it's a winding road. Biochem. Pharmacol. *86*, 1208–1214. https://doi.org/10.1016/j.bcp.2013.08.001.

48. Wang, H.L., and Morales, M. (2009). Pedunculopontine and laterodorsal tegmental nuclei contain distinct populations of cholinergic, glutamatergic and GABAergic neurons in the rat. Eur. J. Neurosci. *29*, 340–358. https://doi.org/10.1111/j.1460-9568.2008.06576.x.

49. Beitz, A.J. (1982). The organization of afferent projections to the midbrain periaqueductal gray of the rat. Neuroscience *7*, 133–159. https://doi.org/10.1016/0306-4522(82)90157-9.

50. Jing, M., Li, Y., Zeng, J., Huang, P., Skirzewski, M., Kljakic, O., Peng, W., Qian, T., Tan, K., Zou, J., et al. (2020). An optimized acetylcholine sensor for monitoring in vivo cholinergic activity. Nat. Methods *17*, 1139–1146. https://doi.org/10.1038/s41592-020-0953-2.

51. Bannon, A.W., and Malmberg, A.B. (2007). Models of nociception: hot-plate, tail-flick, and formalin tests in rodents. Curr. Protoc. Neurosci. *41*, 8.9.1–8.9.16. https://doi.org/10.1002/0471142301.ns0809s41.

52. Tervo, D.G.R., Hwang, B.-Y.Y., Viswanathan, S., Gaj, T., Lavzin, M., Ritola, K.D., Lindo, S., Michael, S., Kuleshova, E., Ojala, D., et al. (2016). A designer AAV variant permits efficient retrograde access to projection neurons. Neuron *92*, 372–382. https://doi.org/10.1016/j.neuron.2016.09.021.

53. Bäck, S., Necarsulmer, J., Whitaker, L.R., Coke, L.M., Koivula, P., Heathward, E.J., Fortuno, L.V., Zhang, Y., Yeh, C.G., Baldwin, H.A., et al. (2019). Neuron-specific genome modification in the adult rat brain using CRISPR-Cas9 transgenic rats. Neuron *102*, 105–119.e8. https://doi.org/10.1016/j.neuron.2019.01.035.

54. Deisseroth, K. (2015). Optogenetics: 10 years of microbial opsins in neuroscience. Nat. Neurosci. *18*, 1213–1225. https://doi.org/10.1038/nn.4091.

55. Ruan, Y., Li, K.Y., Zheng, R., Yan, Y.Q., Wang, Z.X., Chen, Y., Liu, Y., Tian, J., Zhu, L.Y., Lou, H.F., et al. (2022). Cholinergic neurons in the pedunculopontine nucleus guide reversal learning by signaling the changing reward contingency. Cell Rep. *38*, 110437. https://doi.org/10.1016/j.celrep.2022.110437.

56. Prut, L., and Belzung, C. (2003). The open field as a paradigm to measure the effects of drugs on anxiety-like behaviors: a review. Eur. J. Pharmacol. *463*, 3–33. https://doi.org/10.1016/S0014-2999(03)01272-X.

57. Deacon, R.M.J. (2013). Measuring motor coordination in mice. J. Vis. Exp.e2609 https://doi.org/10.3791/2609.

58. Corder, G., Tawfik, V.L., Wang, D., Sypek, E.I., Low, S.A., Dickinson, J.R., Sotoudeh, C., Clark, J.D., Barres, B.A., Bohlen, C.J., and Scherrer, G. (2017). Loss of μ opioid receptor signaling in nociceptors, but not microglia, abrogates morphine tolerance without disrupting analgesia. Nat. Med. *23*, 164–173. https://doi.org/10.1038/nm.4262.

59. Dumas, E.O., and Pollack, G.M. (2008). Opioid tolerance development: a pharmacokinetic/pharmacodynamic perspective. AAPS J. *10*, 537–551. https://doi.org/10.1208/s12248-008-9056-1.

60. Kieffer, B.L., and Evans, C.J. (2002). Opioid tolerance-in search of the Holy Grail. Cell *108*, 587–590. https://doi.org/10.1016/s0092-8674(02)00666-9.

61. Cahill, C.M., Walwyn, W., Taylor, A.M.W., Pradhan, A.A.A., and Evans, C.J. (2016). Allostatic mechanisms of opioid tolerance beyond desensitization and downregulation. Trends Pharmacol. Sci. *37*, 963–976. https://doi.org/10.1016/j.tips.2016.08.002.

62. Wang, F., Flanagan, J., Su, N., Wang, L.C., Bui, S., Nielson, A., Wu, X., Vo, H.T., Ma, X.J., and Luo, Y. (2012). RNAscope: a novel in situ RNA analysis platform for formalin-fixed, paraffin-embedded tissues. J. Mol. Diagn. *14*, 22–29. https://doi.org/10.1016/j.jmoldx.2011.08.002.

63. Sarter, M., Parikh, V., and Howe, W.M. (2009). Phasic acetylcholine release and the volume transmission hypothesis: time to move on. Nat. Rev. Neurosci. *10*, 383–390. https://doi.org/10.1038/nrn2635.

64. Sarter, M., and Lustig, C. (2020). Forebrain cholinergic signaling: wired and phasic, not tonic, and causing behavior. J. Neurosci. *40*, 712–719. https://doi.org/10.1523/JNEUROSCI.1305-19.2019.

65. Disney, A.A., and Higley, M.J. (2020). Diverse spatiotemporal scales of cholinergic signaling in the neocortex. J. Neurosci. *40*, 720–725. https://doi.org/10.1523/JNEUROSCI.1306-19.2019.

66. Galindo-Charles, L., Hernandez-Lopez, S., Galarraga, E., Tapia, D., Bargas, J., Garduño, J., Frías-Dominguez, C., Drucker-Colin, R., Mihailescu, S., and Hernández-López, S. (2008). Serotoninergic dorsal raphe neurons possess functional postsynaptic nicotinic acetylcholine receptors. Synapse *62*, 601–615. https://doi.org/10.1002/syn.20526.

67. Power, S.K., Venkatesan, S., and Lambe, E.K. (2023). Xanomeline restores endogenous nicotinic acetylcholine receptor signaling in mouse prefrontal cortex. Neuropsychopharmacology *48*, 671–682. https://doi.org/10.1038/s41386-023-01531-5.

68. Siegel, R.K., Gusewelle, B.E., and Jarvik, M.E. (1975). Naloxone-induced jumping in morphine dependent mice: stimulus control and motivation. Int. Pharmacopsychiatry *10*, 17–23. https://doi.org/10.1159/000468164.

69. Kaka, G., Rahmanzade, R., Safee, F., and Haghparast, A. (2014). Naloxone induces frequent jumping after chronic morphine and methamphetamine co-administration in rats. Basic Clin. Neurosci. *5*, 42–47.

70. García-Carmona, J.A., Baroja-Mazo, A., Milanés, M.V., and Laorden, M.L. (2015). Sex differences between CRF1 receptor deficient mice following naloxone-precipitated morphine withdrawal in a conditioned place aversion paradigm: implication of HPA axis. PLoS One *10*, e0121125. https://doi.org/10.1371/journal.pone.0121125.

71. Sharf, R., Sarhan, M., and Dileone, R.J. (2010). Role of orexin/hypocretin in dependence and addiction. Brain Res. *1314*, 130–138. https://doi.org/10.1016/j.brainres.2009.08.028.

72. Alvarez-Bagnarol, Y., Marchette, R.C.N., Francis, C., Morales, M.M., and Vendruscolo, L.F. (2022). Neuronal correlates of hyperalgesia and somatic signs of heroin withdrawal in male and female mice. eNeuro *9*, ENEURO.0106-22.2022. https://doi.org/10.1523/ENEURO.0106-22.2022.

73. Rodriguez, E., Sakurai, K., Xu, J., Chen, Y., Toda, K., Zhao, S., Han, B.X., Ryu, D., Yin, H., Liedtke, W., and Wang, F. (2017). A craniofacial-specific monosynaptic circuit enables heightened affective pain. Nat. Neurosci. *20*, 1734–1743. https://doi.org/10.1038/s41593-017-0012-1.

74. Prickaerts, J., van Goethem, N.P., Chesworth, R., Shapiro, G., Boess, F.G., Methfessel, C., Reneerkens, O.A.H., Flood, D.G., Hilt, D., Gawryl, M., et al. (2012). EVP-6124, a novel and selective α7 nicotinic acetylcholine receptor partial agonist, improves memory performance by potentiating the acetylcholine response of α7 nicotinic acetylcholine receptors. Neuropharmacology *62*, 1099–1110. https://doi.org/10.1016/j.neuropharm.2011.10.024.

75. Séguéla, P., Wadiche, J., Dineley-Miller, K., Dani, J.A., and Patrick, J.W. (1993). Molecular cloning, functional properties, and distribution of rat brain alpha 7: a nicotinic cation channel highly permeable to calcium. J. Neurosci. *13*, 596–604. https://doi.org/10.1523/JNEUROSCI.13-02-00596.1993.

76. Vallés, A.S., and Barrantes, F.J. (2022). Interactions between the nicotinic and endocannabinoid receptors at the plasma membrane. Membranes (Basel) *12*, 812. https://doi.org/10.3390/membranes12080812.

77. Melis, M., and Pistis, M. (2012). Hub and switches: endocannabinoid signalling in midbrain dopamine neurons. Philos. Trans. R. Soc. Lond. B Biol. Sci. *367*, 3276–3285. https://doi.org/10.1098/rstb.2011.0383.

78. Melis, M., Scheggi, S., Carta, G., Madeddu, C., Lecca, S., Luchicchi, A., Cadeddu, F., Frau, R., Fattore, L., Fadda, P., et al. (2013). PPARα regulates cholinergic-driven activity of midbrain dopamine neurons via a novel mechanism involving α7 nicotinic acetylcholine receptors. J. Neurosci. *33*, 6203–6211. https://doi.org/10.1523/JNEUROSCI.4647-12.2013.

79. Huang, J., Gadotti, V.M., Chen, L., Souza, I.A., Huang, S., Wang, D., Ramakrishnan, C., Deisseroth, K., Zhang, Z., and Zamponi, G.W. (2019). A neuronal circuit for activating descending modulation of neuropathic pain. Nat. Neurosci. *22*, 1659–1668. https://doi.org/10.1038/s41593-019-0481-5.

80. Huang, W.J., Chen, W.W., and Zhang, X. (2016). Endocannabinoid system: role in depression, reward and pain control (review). Mol. Med. Rep. *14*, 2899–2903. https://doi.org/10.3892/mmr.2016.5585.

81. Sagar, D.R., Staniaszek, L.E., Okine, B.N., Woodhams, S., Norris, L.M., Pearson, R.G., Garle, M.J., Alexander, S.P.H., Bennett, A.J., Barrett, D.A., et al. (2010). Tonic modulation of spinal hyperexcitability by the endocannabinoid receptor system in a rat model of osteoarthritis pain. Arthritis Rheum. *62*, 3666–3676. https://doi.org/10.1002/art.27698.

82. Costa, M., Squassina, A., Congiu, D., Chillotti, C., Niola, P., Galderisi, S., Pistis, M., and Del Zompo, M. (2013). Investigation of endocannabinoid system genes suggests association between peroxisome proliferator activator receptor-α gene (PPARA) and schizophrenia. Eur. Neuropsychopharmacol. *23*, 749–759. https://doi.org/10.1016/j.euroneuro.2012.07.007.

83. Okine, B.N., Gaspar, J.C., and Finn, D.P. (2019). PPARs and pain. Br. J. Pharmacol. *176*, 1421–1442. https://doi.org/10.1111/bph.14339.

84. Maeda, T., and Kishioka, S. (2009). PPAR and pain. Int. Rev. Neurobiol. *85*, 165–177. https://doi.org/10.1016/S0074-7742(09)85013-7.

85. Donvito, G., Wilkerson, J.L., Damaj, M.I., and Lichtman, A.H. (2016). Palmitoylethanolamide reverses paclitaxel-induced allodynia in mice. J. Pharmacol. Exp. Ther. *359*, 310–318. https://doi.org/10.1124/jpet.116.236182.

86. Caillaud, M., Patel, N.H., White, A., Wood, M., Contreras, K.M., Toma, W., Alkhlaif, Y., Roberts, J.L., Tran, T.H., Jackson, A.B., et al. (2021). Targeting peroxisome proliferator-activated receptor-α (PPAR- α) to reduce paclitaxel-induced peripheral neuropathy. Brain Behav. Immun. *93*, 172–185. https://doi.org/10.1016/j.bbi.2021.01.004.

87. Jackson, A., Bagdas, D., Muldoon, P.P., Lichtman, A.H., Carroll, F.I., Greenwald, M., Miles, M.F., and Damaj, M.I. (2017). In vivo interactions between α7 nicotinic acetylcholine receptor and nuclear peroxisome proliferator-activated receptor-α: implication for nicotine dependence. Neuropharmacology *118*, 38–45. https://doi.org/10.1016/j.neuropharm.2017.03.005.

88. Lee, W.H., and Kim, S.G. (2010). AMPK-dependent metabolic regulation by PPAR agonists. PPAR Res. *2010*, 549101. https://doi.org/10.1155/2010/549101.

89. Asiedu, M.N., Dussor, G., and Price, T.J. (2016). Targeting AMPK for the alleviation of pathological pain. Exp Suppl. *107*, 257–285. https://doi.org/10.1007/978-3-319-43589-3_11.

90. Wang, S., and Dai, Y. (2021). Roles of AMPK and its downstream signals in pain regulation. Life (Basel) *11*, 836. https://doi.org/10.3390/life11080836.

91. Xiang, H.C., Lin, L.X., Hu, X.F., Zhu, H., Li, H.P., Zhang, R.Y., Hu, L., Liu, W.T., Zhao, Y.L., Shu, Y., et al. (2019). AMPK activation attenuates inflammatory pain through inhibiting NF-κB activation and IL-1β expression. J. Neuroinflammation *16*, 34. https://doi.org/10.1186/s12974-019-1411-x.

92. Price, T.J., and Dussor, G. (2013). AMPK: an emerging target for modification of injury-induced pain plasticity. Neurosci. Lett. *557*, 9–18. https://doi.org/10.1016/j.neulet.2013.06.060.

93. Bullón, P., Alcocer-Gómez, E., Carrión, A.M., Marín-Aguilar, F., Garrido-Maraver, J., Román-Malo, L., Ruiz-Cabello, J., Culic, O., Ryffel, B.,

Apetoh, L., et al. (2016). AMPK phosphorylation modulates pain by activation of NLRP3 inflammasome. Antioxid. Redox Signal. *24*, 157–170. https://doi.org/10.1089/ars.2014.6120.

94. Tsantoulas, C., Zhu, L., Yip, P., Grist, J., Michael, G.J., and McMahon, S.B. (2014). Kv2 dysfunction after peripheral axotomy enhances sensory neuron responsiveness to sustained input. Exp. Neurol. *251*, 115–126. https://doi.org/10.1016/j.expneurol.2013.11.011.

95. Zhu, X., Chen, Y., Xu, X., Xu, X., Lu, Y., Huang, X., Zhou, J., Hu, L., Wang, J., and Shen, X. (2020). SP6616 as a Kv2.1 inhibitor efficiently ameliorates peripheral neuropathy in diabetic mice. EBioMedicine *61*, 103061. https://doi.org/10.1016/j.ebiom.2020.103061.

96. Eacret, D., Noreck, J., and Blendy, J.A. (2022). Adenosine monophosphate-activated protein kinase (AMPK) in serotonin neurons mediates select behaviors during protracted withdrawal from morphine in mice. Behav. Brain Res. *419*, 113688. https://doi.org/10.1016/j.bbr.2021.113688.

97. Zhang, Y., Tao, G.J., Hu, L., Qu, J., Han, Y., Zhang, G., Qian, Y., Jiang, C.Y., and Liu, W.T. (2017). Lidocaine alleviates morphine tolerance via AMPK-SOCS3-dependent neuroinflammation suppression in the spinal cord. J. Neuroinflammation *14*, 211. https://doi.org/10.1186/s12974-017-0983-6.

98. Li, L., Zhang, H., Li, T., and Zhang, B. (2011). Involvement of adenosine monophosphate-activated protein kinase in morphine-induced cardioprotection. J. Surg. Res. *169*, 179–187. https://doi.org/10.1016/j.jss.2009.11.007.

99. Pan, Y., Sun, X., Jiang, L., Hu, L., Kong, H., Han, Y., Qian, C., Song, C., Qian, Y., and Liu, W. (2016). Metformin reduces morphine tolerance by inhibiting microglial-mediated neuroinflammation. J. Neuroinflammation *13*, 294. https://doi.org/10.1186/s12974-016-0754-9.

100. Muraleedharan, R., and Dasgupta, B. (2022). AMPK in the brain: its roles in glucose and neural metabolism. FEBS J. *289*, 2247–2262. https://doi.org/10.1111/febs.16151.

101. Misonou, H., Mohapatra, D.P., and Trimmer, J.S. (2005). Kv2.1: a voltage-gated k+ channel critical to dynamic control of neuronal excitability. Neurotoxicology *26*, 743–752. https://doi.org/10.1016/j.neuro.2005.02.003.

102. Ikematsu, N., Dallas, M.L., Ross, F.A., Lewis, R.W., Rafferty, J.N., David, J.A., Suman, R., Peers, C., Hardie, D.G., and Evans, A.M. (2011). Phosphorylation of the voltage-gated potassium channel Kv2.1 by AMP-activated protein kinase regulates membrane excitability. Proc. Natl. Acad. Sci. USA *108*, 18132–18137. https://doi.org/10.1073/pnas.1106201108.

103. Melis, M., Carta, S., Fattore, L., Tolu, S., Yasar, S., Goldberg, S.R., Fratta, W., Maskos, U., and Pistis, M. (2010). Peroxisome proliferator-activated receptors-alpha modulate dopamine cell activity through nicotinic receptors. Biol. Psychiatry *68*, 256–264. https://doi.org/10.1016/j.biopsych.2010.04.016.

104. Donvito, G., Bagdas, D., Toma, W., Rahimpour, E., Jackson, A., Meade, J.A., AlSharari, S., Kulkarni, A.R., Ivy Carroll, F., Lichtman, A.H., et al. (2017). The interaction between alpha 7 nicotinic acetylcholine receptor and nuclear peroxisome proliferator-activated receptor-α represents a new antinociceptive signaling pathway in mice. Exp. Neurol. *295*, 194–201. https://doi.org/10.1016/j.expneurol.2017.06.014.

105. Marvin, J.S., Shimoda, Y., Magloire, V., Leite, M., Kawashima, T., Jensen, T.P., Kolb, I., Knott, E.L., Novak, O., Podgorski, K., et al. (2019). A genetically encoded fluorescent sensor for in vivo imaging of GABA. Nat. Methods *16*, 763–770. https://doi.org/10.1038/s41592-019-0471-2.

106. Jackson, A., Alkhlaif, Y., Papke, R.L., Brunzell, D.H., and Damaj, M.I. (2019). Impact of modulation of the α7 nicotinic acetylcholine receptor on nicotine reward in the mouse conditioned place preference test. Psychopharmacol. (Berl.) *236*, 3593–3599. https://doi.org/10.1007/s00213-019-05331-y.

107. Freitas, K., Ghosh, S., Ivy Carroll, F., Lichtman, A.H., and Imad Damaj, M. (2013). Effects of α7 positive allosteric modulators in murine inflammatory and chronic neuropathic pain models. Neuropharmacology *65*, 156–164. https://doi.org/10.1016/j.neuropharm.2012.08.022.

108. Guo, H., Xie, Q., Cui, J., Xu, D., Deji, C., Chen, Y., Wang, Y., and Lai, J. (2019). Naloxone reversed cognitive impairments induced by repeated morphine under heavy perceptual load in the 5-choice serial reaction time task. J. Neurosci. Res. *97*, 1051–1065. https://doi.org/10.1002/jnr.24427.

109. Kitanaka, J., Kitanaka, N., Hall, F.S., Fujii, M., Goto, A., Kanda, Y., Koizumi, A., Kuroiwa, H., Mibayashi, S., Muranishi, Y., et al. (2015). Memory impairment and reduced exploratory behavior in mice after administration of systemic morphine. J. Exp. Neurosci. *9*, 27–35. https://doi.org/10.4137/JEN.S25057.

110. Murphy, N.P., Lam, H.A., and Maidment, N.T. (2001). A comparison of morphine-induced locomotor activity and mesolimbic dopamine release in C57BL6, 129Sv and DBA2 mice. J. Neurochem. *79*, 626–635. https://doi.org/10.1046/j.1471-4159.2001.00599.x.

111. Denk, F., McMahon, S.B., and Tracey, I. (2014). Pain vulnerability: a neurobiological perspective. Nat. Neurosci. *17*, 192–200. https://doi.org/10.1038/nn.3628.

112. Waxman, S.G., and Zamponi, G.W. (2014). Regulating excitability of peripheral afferents: emerging ion channel targets. Nat. Neurosci. *17*, 153–163. https://doi.org/10.1038/nn.3602.

113. Piomelli, D., and Sasso, O. (2014). Peripheral gating of pain signals by endogenous lipid mediators. Nat. Neurosci. *17*, 164–174. https://doi.org/10.1038/nn.3612.

114. Prescott, S.A., Ma, Q., and De Koninck, Y. (2014). Normal and abnormal coding of somatosensory stimuli causing pain. Nat. Neurosci. *17*, 183–191. https://doi.org/10.1038/nn.3629.

115. Kuner, R., and Flor, H. (2016). Structural plasticity and reorganisation in chronic pain. Nat. Rev. Neurosci. *18*, 20–30. https://doi.org/10.1038/nrn.2016.162.

116. Zhu, X., Xu, Y., Shen, Z., Zhang, H., Xiao, S., Zhu, Y., Wu, M., Chen, Y., Wu, Z., Xu, Y., et al. (2021). Rostral anterior cingulate cortex-ventrolateral periaqueductal gray circuit underlies electroacupuncture to alleviate hyperalgesia but not anxiety-like behaviors in mice with spared nerve injury. Front. Neurosci. *15*, 757628. https://doi.org/10.3389/fnins.2021.757628.

117. Sun, Y., Wang, J., Liang, S.H., Ge, J., Lu, Y.C., Li, J.N., Chen, Y.B., Luo, D.S., Li, H., and Li, Y.Q. (2020). Involvement of the ventrolateral periaqueductal gray matter-central medial thalamic nucleus-basolateral amygdala pathway in neuropathic pain regulation of rats. Front. Neuroanat. *14*, 32. https://doi.org/10.3389/fnana.2020.00032.

118. Huang, J., Zhang, Z., Gambeta, E., Chen, L., and Zamponi, G.W. (2021). An orbitofrontal cortex to midbrain projection modulates hypersensitivity after peripheral nerve injury. Cell Rep. *35*, 109033. https://doi.org/10.1016/j.celrep.2021.109033.

119. Yin, J.B., Liang, S.H., Li, F., Zhao, W.J., Bai, Y., Sun, Y., Wu, Z.Y., Ding, T., Sun, Y., Liu, H.X., et al. (2020). dmPFC-vlPAG projection neurons contribute to pain threshold maintenance and antianxiety behaviors. J. Clin. Invest. *130*, 6555–6570. https://doi.org/10.1172/JCI127607.

120. Sun, Y., Blanco-Centurion, C., Zou, B., Bendell, E., Shiromani, P.J., and Liu, M. (2019). Amygdala GABA neurons project to vlPAG and mPFC. IBRO Rep. *6*, 132–136. https://doi.org/10.1016/j.ibror.2019.03.001.

121. Li, J.N., Ren, J.H., He, C.B., Zhao, W.J., Li, H., Dong, Y.L., and Li, Y.Q. (2021). Projections from the lateral parabrachial nucleus to the lateral and ventral lateral periaqueductal gray subregions mediate the itching sensation. Pain *162*, 1848–1863. https://doi.org/10.1097/j.pain.0000000000002193.

122. Yeh, L.F., Ozawa, T., and Johansen, J.P. (2021). Functional organization of the midbrain periaqueductal gray for regulating aversive memory formation. Mol. Brain *14*, 136. https://doi.org/10.1186/s13041-021-00844-0.

123. Bohn, L.M., Gainetdinov, R.R., Lin, F.T., Lefkowitz, R.J., and Caron, M.G. (2000). Mu-opioid receptor desensitization by beta-arrestin-2 determines morphine tolerance but not dependence. Nature *408*, 720–723. https://doi.org/10.1038/35047086.

124. Al-Hasani, R., and Bruchas, M.R. (2011). Molecular mechanisms of opioid receptor-dependent signaling and behavior. Anesthesiology *115*, 1363–1381. https://doi.org/10.1097/ALN.0b013e318238bba6.

125. McPherson, K.B., and Ingram, S.L. (2022). Cellular and circuit diversity determines the impact of endogenous opioids in the descending pain modulatory pathway. Front. Syst. Neurosci. *16*, 963812. https://doi.org/10.3389/fnsys.2022.963812.

126. Macey, T.A., Bobeck, E.N., Suchland, K.L., Morgan, M.M., and Ingram, S.L. (2015). Change in functional selectivity of morphine with the development of antinociceptive tolerance. Br. J. Pharmacol. *172*, 549–561. https://doi.org/10.1111/bph.12703.

127. Bagley, E.E., Chieng, B.C.H., Christie, M.J., and Connor, M. (2005). Opioid tolerance in periaqueductal gray neurons isolated from mice chronically treated with morphine. Br. J. Pharmacol. *146*, 68–76. https://doi.org/10.1038/sj.bjp.0706315.

128. Hasselmo, M.E. (2006). The role of acetylcholine in learning and memory. Curr. Opin. Neurobiol. *16*, 710–715. https://doi.org/10.1016/j.conb.2006.09.002.

129. Al-Hasani, R., Gowrishankar, R., Schmitz, G.P., Pedersen, C.E., Marcus, D.J., Shirley, S.E., Hobbs, T.E., Elerding, A.J., Renaud, S.J., Jing, M., et al. (2021). Ventral tegmental area GABAergic inhibition of cholinergic interneurons in the ventral nucleus accumbens shell promotes reward reinforcement. Nat. Neurosci. *24*, 1414–1428. https://doi.org/10.1038/s41593-021-00898-2.

130. Takács, V.T., Cserép, C., Schlingloff, D., Pósfai, B., Szőnyi, A., Sos, K.E., Környei, Z., Dénes, Á., Gulyás, A.I., Freund, T.F., and Nyiri, G. (2018). Co-transmission of acetylcholine and GABA regulates hippocampal states. Nat. Commun. *9*, 2848. https://doi.org/10.1038/s41467-018-05136-1.

131. Saunders, A., Granger, A.J., and Sabatini, B.L. (2015). Corelease of acetylcholine and GABA from cholinergic forebrain neurons. ELife *4*, e06412. https://doi.org/10.7554/eLife.06412.

132. Weber, F., Hoang Do, J.P., Chung, S., Beier, K.T., Bikov, M., Saffari Doost, M., and Dan, Y. (2018). Regulation of REM and non-REM sleep by periaqueductal GABAergic neurons. Nat. Commun. *9*, 354. https://doi.org/10.1038/s41467-017-02765-w.

133. Patel, A.A., McAlinden, N., Mathieson, K., and Sakata, S. (2020). Simultaneous electrophysiology and fiber photometry in freely behaving mice. Front. Neurosci. *14*, 148. https://doi.org/10.3389/fnins.2020.00148.

134. Van Dort, C.J., Zachs, D.P., Kenny, J.D., Zheng, S., Goldblum, R.R., Gelwan, N.A., Ramos, D.M., Nolan, M.A., Wang, K., Weng, F.J., et al. (2015). Optogenetic activation of cholinergic neurons in the PPT or LDT induces REM sleep. Proc. Natl. Acad. Sci. USA *112*, 584–589. https://doi.org/10.1073/pnas.1423136112.

135. Mondoloni, S., Mameli, M., and Congiu, M. (2022). Reward and aversion encoding in the lateral habenula for innate and learned behaviours. Transl. Psychiatry *12*, 3. https://doi.org/10.1038/s41398-021-01774-0.

136. Roy, D.S., Park, Y.G., Kim, M.E., Zhang, Y., Ogawa, S.K., DiNapoli, N., Gu, X., Cho, J.H., Choi, H., Kamentsky, L., et al. (2022). Brain-wide mapping reveals that engrams for a single memory are distributed across multiple brain regions. Nat. Commun. *13*, 1799. https://doi.org/10.1038/s41467-022-29384-4.

137. Lawrenson, C., Paci, E., Pickford, J., Drake, R.A.R., Lumb, B.M., and Apps, R. (2022). Cerebellar modulation of memory encoding in the periaqueductal grey and fear behaviour. ELife *11*, e76278. https://doi.org/10.7554/eLife.76278.

138. Záborszky, L., Gombkoto, P., Varsanyi, P., Gielow, M.R., Poe, G., Role, L.W., Ananth, M., Rajebhosale, P., Talmage, D.A., Hasselmo, M.E., et al. (2018). Specific basal forebrain-cortical cholinergic circuits coordi-nate cognitive operations. J. Neurosci. *38*, 9446–9458. https://doi.org/10.1523/JNEUROSCI.1676-18.2018.

139. Tashakori-Sabzevar, F., and Ward, R.D. (2018). Basal forebrain mediates motivational recruitment of attention by reward-associated cues. Front. Neurosci. *12*, 786. https://doi.org/10.3389/fnins.2018.00786.

140. Voytko, M.L. (1996). Cognitive functions of the basal forebrain cholinergic system in monkeys: memory or attention? Behav. Brain Res. *75*, 13–25. https://doi.org/10.1016/0166-4328(95)00143-3.

141. Oliva, V., Gregory, R., Davies, W.E., Harrison, L., Moran, R., Pickering, A.E., and Brooks, J.C.W. (2021). Parallel cortical-brainstem pathways to attentional analgesia. Neuroimage *226*, 117548. https://doi.org/10.1016/j.neuroimage.2020.117548.

142. Oliva, V., Gregory, R., Brooks, J.C.W., and Pickering, A.E. (2022). Central pain modulatory mechanisms of attentional analgesia are preserved in fibromyalgia. Pain *163*, 125–136. https://doi.org/10.1097/j.pain.0000000000002319.

143. Colloca, L., Klinger, R., Flor, H., and Bingel, U. (2013). Placebo analgesia: psychological and neurobiological mechanisms. Pain *154*, 511–514. https://doi.org/10.1016/j.pain.2013.02.002.

144. Schafer, S.M., Geuter, S., and Wager, T.D. (2018). Mechanisms of placebo analgesia: a dual-process model informed by insights from cross-species comparisons. Prog. Neurobiol. *160*, 101–122. https://doi.org/10.1016/j.pneurobio.2017.10.008.

145. Zunhammer, M., Spisák, T., Wager, T.D., and Bingel, U.; Placebo Imaging Consortium (2021). Meta-analysis of neural systems underlying placebo analgesia from individual participant fMRI data. Nat. Commun. *12*, 1391. https://doi.org/10.1038/s41467-021-21179-3.

146. Kerekes, N., Sanchéz-Pérez, A.M., and Landry, M. (2021). Neuroinflammation as a possible link between attention-deficit/hyperactivity disorder (ADHD) and pain. Med. Hypotheses *157*, 110717. https://doi.org/10.1016/j.mehy.2021.110717.

147. Pati, D., and Kash, T.L. (2021). Tumor necrosis factor-α modulates GABAergic and dopaminergic neurons in the ventrolateral periaqueductal gray of female mice. J. Neurophysiol. *126*, 2119–2129. https://doi.org/10.1152/jn.00251.2021.

148. Lau, B.K., and Vaughan, C.W. (2014). Descending modulation of pain: the GABA disinhibition hypothesis of analgesia. Curr. Opin. Neurobiol. *29*, 159–164. https://doi.org/10.1016/j.conb.2014.07.010.

149. Hahm, E.T., Kim, Y., Lee, J.J., and Cho, Y.W. (2011). GABAergic synaptic response and its opioidergic modulation in periaqueductal gray neurons of rats with neuropathic pain. BMC Neurosci. *12*, 41. https://doi.org/10.1186/1471-2202-12-41.

150. Tonsfeldt, K.J., Suchland, K.L., Beeson, K.A., Lowe, J.D., Li, M.H., and Ingram, S.L. (2016). Sex differences in GABAA signaling in the periaqueductal gray induced by persistent inflammation. J. Neurosci. *36*, 1669–1681. https://doi.org/10.1523/JNEUROSCI.1928-15.2016.

151. Wang, Y., Su, D.M., Wang, R.H., Liu, Y., and Wang, H. (2005). Antinociceptive effects of choline against acute and inflammatory pain. Neuroscience *132*, 49–56. https://doi.org/10.1016/j.neuroscience.2004.12.026.

152. Hamurtekin, E., and Gurun, M.S. (2006). The antinociceptive effects of centrally administered CDP-choline on acute pain models in rats: the involvement of cholinergic system. Brain Res. *1117*, 92–100. https://doi.org/10.1016/j.brainres.2006.07.118.

153. Damaj, M.I., Meyer, E.M., and Martin, B.R. (2000). The antinociceptive effects of alpha7 nicotinic agonists in an acute pain model. Neuropharmacology *39*, 2785–2791. https://doi.org/10.1016/s0028-3908(00)00139-8.

154. Bagdas, D., Sonat, F.A., Hamurtekin, E., Sonal, S., and Gurun, M.S. (2011). The antihyperalgesic effect of cytidine-5′-diphosphate-choline in neuropathic and inflammatory pain models. Behav. Pharmacol. *22*, 589–598. https://doi.org/10.1097/FBP.0b013e32834a1efb.

155. Gao, Z.R., Chen, W.Z., Liu, M.Z., Chen, X.J., Wan, L., Zhang, X.Y., Yuan, L., Lin, J.K., Wang, M., Zhou, L., et al. (2019). Tac1-expressing neurons in the periaqueductal gray facilitate the itch-scratching cycle via descending regulation. Neuron 101, 45–59.e9. https://doi.org/10.1016/j.neuron.2018.11.010.

156. Lau, B.K., and Vaughan, C.W. (2008). Muscarinic modulation of synaptic transmission via endocannabinoid signalling in the rat midbrain periaqueductal gray. Mol. Pharmacol. 74, 1392–1398. https://doi.org/10.1124/mol.108.045872.

157. Samochocki, M., Höffle, A., Fehrenbacher, A., Jostock, R., Ludwig, J., Christner, C., Radina, M., Zerlin, M., Ullmer, C., Pereira, E.F.R., et al. (2003). Galantamine is an allosterically potentiating ligand of neuronal nicotinic but not of muscarinic acetylcholine receptors. J. Pharmacol. Exp. Ther. 305, 1024–1036. https://doi.org/10.1124/jpet.102.045773.

158. Maier-Peuschel, M., Frölich, N., Dees, C., Hommers, L.G., Hoffmann, C., Nikolaev, V.O., and Lohse, M.J. (2010). A fluorescence resonance energy transfer-based M2 muscarinic receptor sensor reveals rapid kinetics of allosteric modulation. J. Biol. Chem. 285, 8793–8800. https://doi.org/10.1074/jbc.M109.098517.

159. Dore, K., Stein, I.S., Brock, J.A., Castillo, P.E., Zito, K., and Sjöström, P.J. (2017). Unconventional NMDA receptor signaling. J. Neurosci. 37, 10800–10807. https://doi.org/10.1523/JNEUROSCI.1825-17.2017.

160. Valbuena, S., and Lerma, J. (2016). Non-canonical signaling, the hidden life of ligand-gated ion channels. Neuron 92, 316–329. https://doi.org/10.1016/j.neuron.2016.10.016.

161. Aow, J., Dore, K., and Malinow, R. (2015). Conformational signaling required for synaptic plasticity by the NMDA receptor complex. Proc. Natl. Acad. Sci. USA 112, 14711–14716. https://doi.org/10.1073/pnas.1520029112.

162. Nabavi, S., Kessels, H.W., Alfonso, S., Aow, J., Fox, R., and Malinow, R. (2013). Metabotropic NMDA receptor function is required for NMDA receptor-dependent long-term depression. Proc. Natl. Acad. Sci. USA 110, 4027–4032. https://doi.org/10.1073/pnas.1219454110.

163. Dore, K., Aow, J., and Malinow, R. (2016). The emergence of NMDA receptor metabotropic function: insights from imaging. Front. Synaptic Neurosci. 8, 20. https://doi.org/10.3389/fnsyn.2016.00020.

164. Corradi, J., and Bouzat, C. (2016). Understanding the bases of function and modulation of α7 nicotinic receptors: implications for drug discovery. Mol. Pharmacol. 90, 288–299. https://doi.org/10.1124/mol.116.104240.

165. Yakel, J.L. (2012). Nicotinic ACh receptors in the hippocampus: role in excitability and plasticity. Nicotine Tob. Res. 14, 1249–1257. https://doi.org/10.1093/ntr/nts091.

166. Kabbani, N., and Nichols, R.A. (2018). Beyond the channel: metabotropic signaling by nicotinic receptors. Trends Pharmacol. Sci. 39, 354–366. https://doi.org/10.1016/j.tips.2018.01.002.

167. Zdanowski, R., Krzyżowska, M., Ujazdowska, D., Lewicka, A., and Lewicki, S. (2015). Role of α7 nicotinic receptor in the immune system and intracellular signaling pathways. Cent. Eur J. Immunol. 40, 373–379. https://doi.org/10.5114/ceji.2015.54602.

168. King, J.R., Gillevet, T.C., and Kabbani, N. (2017). A G protein-coupled α7 nicotinic receptor regulates signaling and TNF-α release in microglia. FEBS Open Bio 7, 1350–1361. https://doi.org/10.1002/2211-5463.12270.

169. Udakis, M., Wright, V.L., Wonnacott, S., and Bailey, C.P. (2016). Integration of inhibitory and excitatory effects of α7 nicotinic acetylcholine receptor activation in the prelimbic cortex regulates network activity and plasticity. Neuropharmacology 105, 618–629. https://doi.org/10.1016/j.neuropharm.2016.02.028.

170. Sawamura, N., Ju, Y., and Asahi, T. (2018). Cholinergic receptor, nicotinic, alpha 7 as a target molecule of Arctic mutant amyloid β. Neural Regen. Res. 13, 1360–1361. https://doi.org/10.4103/1673-5374.235238.

171. Souza, C.M., do Amaral, C.L., Souza, S.C., de Souza, A.C.P., de Cássia Alves Martins, I., Contieri, L.S., Milanski, M., Torsoni, A.S., Ignacio-Souza, L.M., and Torsoni, M.A. (2019). JAK2/STAT3 pathway is required

for α7nAChR-dependent expression of POMC and AGRP neuropeptides in male mice. Cell. Physiol. Biochem. 53, 701–712. https://doi.org/10.33594/000000166.

172. Charpantier, E., Wiesner, A., Huh, K.H., Ogier, R., Hoda, J.C., Allaman, G., Raggenbass, M., Feuerbach, D., Bertrand, D., and Fuhrer, C. (2005). Alpha7 neuronal nicotinic acetylcholine receptors are negatively regulated by tyrosine phosphorylation and Src-family kinases. J. Neurosci. 25, 9836–9849. https://doi.org/10.1523/JNEUROSCI.3497-05.2005.

173. Johnson, S.L., Beurg, M., Marcotti, W., and Fettiplace, R. (2011). Prestin-driven cochlear amplification is not limited by the outer hair cell membrane time constant. Neuron 70, 1143–1154. https://doi.org/10.1016/j.neuron.2011.04.024.

174. Daoudal, G., and Debanne, D. (2003). Long-term plasticity of intrinsic excitability: learning rules and mechanisms. Learn. Mem. 10, 456–465. https://doi.org/10.1101/lm.64103.

175. van Welie, I., van Hooft, J.A., and Wadman, W.J. (2004). Homeostatic scaling of neuronal excitability by synaptic modulation of somatic hyperpolarization-activated Ih channels. Proc. Natl. Acad. Sci. USA 101, 5123–5128. https://doi.org/10.1073/pnas.0307711101.

176. Nelson, A.B., Krispel, C.M., Sekirnjak, C., and du Lac, S. (2003). Long-lasting increases in intrinsic excitability triggered by inhibition. Neuron 40, 609–620. https://doi.org/10.1016/s0896-6273(03)00641-x.

177. Gottschalk, A., Almedom, R.B., Schedletzky, T., Anderson, S.D., Yates, J.R., and Schafer, W.R. (2005). Identification and characterization of novel nicotinic receptor-associated proteins in Caenorhabditis elegans. EMBO J. 24, 2566–2578. https://doi.org/10.1038/sj.emboj.7600741.

178. McClure-Begley, T.D., Stone, K.L., Marks, M.J., Grady, S.R., Colangelo, C.M., Lindstrom, J.M., and Picciotto, M.R. (2013). Exploring the nicotinic acetylcholine receptor-associated proteome with iTRAQ and transgenic mice. Genomics Proteomics Bioinformatics 11, 207–218. https://doi.org/10.1016/j.gpb.2013.05.005.

179. Shen, J.X., and Yakel, J.L. (2009). Nicotinic acetylcholine receptor-mediated calcium signaling in the nervous system. Acta Pharmacol. Sin. 30, 673–680. https://doi.org/10.1038/aps.2009.64.

180. Decker, E.R., and Dani, J.A. (1990). Calcium permeability of the nicotinic acetylcholine receptor: the single-channel calcium influx is significant. J. Neurosci. 10, 3413–3420.

181. Dani, J.A. (2015). Neuronal nicotinic acetylcholine receptor structure and function and response to nicotine. Int. Rev. Neurobiol. 124, 3–19. https://doi.org/10.1016/bs.irn.2015.07.001.

182. Belforte, N., Agostinone, J., Alarcon-Martinez, L., Villafranca-Baughman, D., Dotigny, F., Cueva Vargas, J.L., and Di Polo, A. (2021). AMPK hyperactivation promotes dendrite retraction, synaptic loss, and neuronal dysfunction in glaucoma. Mol. Neurodegener. 16, 43. https://doi.org/10.1186/s13024-021-00466-z.

183. Williams, T., Courchet, J., Viollet, B., Brenman, J.E., and Polleux, F. (2011). AMP-activated protein kinase (AMPK) activity is not required for neuronal development but regulates axogenesis during metabolic stress. Proc. Natl. Acad. Sci. USA 108, 5849–5854. https://doi.org/10.1073/pnas.1013660108.

184. Domise, M., Sauvé, F., Didier, S., Caillerez, R., Bégard, S., Carrier, S., Colin, M., Marinangeli, C., Buée, L., and Vingtdeux, V. (2019). Neuronal AMP-activated protein kinase hyper-activation induces synaptic loss by an autophagy-mediated process. Cell Death Dis. 10, 221. https://doi.org/10.1038/s41419-019-1464-x.

185. Wójtowicz, S., Strosznajder, A.K., Jeżyna, M., and Strosznajder, J.B. (2020). The novel role of PPAR alpha in the brain: promising target in therapy of Alzheimer's disease and other neurodegenerative disorders. Neurochem. Res. 45, 972–988. https://doi.org/10.1007/s11064-020-02993-5.

186. Tyagi, S., Gupta, P., Saini, A.S., Kaushal, C., and Sharma, S. (2011). The peroxisome proliferator-activated receptor: a family of nuclear receptors

role in various diseases. J. Adv. Pharm. Technol. Res. *2*, 236–240. https://doi.org/10.4103/2231-4040.90879.

187. Grygiel-Górniak, B. (2014). Peroxisome proliferator-activated receptors and their ligands: nutritional and clinical implications–a review. Nutr. J. *13*, 17. https://doi.org/10.1186/1475-2891-13-17.

188. Slivicki, R.A., Xu, Z., Kulkarni, P.M., Pertwee, R.G., Mackie, K., Thakur, G.A., and Hohmann, A.G. (2018). Positive allosteric modulation of cannabinoid receptor type 1 suppresses pathological pain without producing tolerance or dependence. Biol. Psychiatry *84*, 722–733. https://doi.org/10.1016/j.biopsych.2017.06.032.

189. Datta, U., Kelley, L.K., Middleton, J.W., and Gilpin, N.W. (2020). Positive allosteric modulation of the cannabinoid type-1 receptor (CB1R) in periaqueductal gray (PAG) antagonizes anti-nociceptive and cellular effects of a mu-opioid receptor agonist in morphine-withdrawn rats. Psychopharmacol. (Berl.) *237*, 3729–3739. https://doi.org/10.1007/s00213-020-05650-5.

190. Slivicki, R.A., Iyer, V., Mali, S.S., Garai, S., Thakur, G.A., Crystal, J.D., and Hohmann, A.G. (2020). Positive allosteric modulation of CB1 cannabinoid receptor signaling enhances morphine antinociception and attenuates morphine tolerance without enhancing morphine- induced dependence or reward. Front. Mol. Neurosci. *13*, 54. https://doi.org/10.3389/fnmol.2020.00054.

191. Jiang, Z., Wang, Q., Zhao, J., Wang, J., Li, Y., Dai, W., Zhang, X., Fang, Z., Hou, W., and Xiong, L. (2022). Sex-specific cannabinoid 1 receptors on GABAergic neurons in the ventrolateral periaqueductal gray mediate analgesia in mice. J. Comp. Neurol. *530*, 2315–2334. https://doi.org/10.1002/cne.25334.

192. Winters, B.L., Lau, B.K., and Vaughan, C.W. (2022). Cannabinoids and opioids differentially target extrinsic and intrinsic GABAergic inputs onto the periaqueductal grey descending pathway. J. Neurosci. *42*, 7744–7756. https://doi.org/10.1523/JNEUROSCI.0997-22.2022.

193. Norton, A.B.W.W., Jo, Y.S., Clark, E.W., Taylor, C.A., and Mizumori, S.J.Y.Y. (2011). Independent neural coding of reward and movement by pedunculopontine tegmental nucleus neurons in freely navigating rats. Eur. J. Neurosci. *33*, 1885–1896. https://doi.org/10.1111/j.1460-9568.2011.07649.x.

194. Yau, H.J., Wang, D.V., Tsou, J.H., Chuang, Y.F., Chen, B.T., Deisseroth, K., Ikemoto, S., and Bonci, A. (2016). Pontomesencephalic tegmental afferents to VTA non-dopamine neurons are necessary for appetitive Pavlovian learning. Cell Rep. *16*, 2699–2710. https://doi.org/10.1016/j.celrep.2016.08.007.

195. Sherathiya, V.N., Schaid, M.D., Seiler, J.L., Lopez, G.C., and Lerner, T.N. (2021). GuPPy, a Python toolbox for the analysis of fiber photometry data. Sci. Rep. *11*, 24212. https://doi.org/10.1038/s41598-021-03626-9.

196. Bruno, C.A., O'Brien, C., Bryant, S., Mejaes, J.I., Estrin, D.J., Pizzano, C., and Barker, D.J. (2021). pMAT: an open-source software suite for the analysis of fiber photometry data. Pharmacol. Biochem. Behav. *201*, 173093. https://doi.org/10.1016/j.pbb.2020.173093.

197. Cantu, D.A., Wang, B., Gongwer, M.W., He, C.X., Goel, A., Suresh, A., Kourdougli, N., Arroyo, E.D., Zeiger, W., and Portera-Cailliau, C. (2020). EZcalcium: open-source toolbox for analysis of calcium imaging data. Front. Neural Circuits *14*, 25. https://doi.org/10.3389/fncir.2020.00025.

198. Aharoni, D., and Hoogland, T.M. (2019). Circuit investigations with open-source miniaturized microscopes: past, present and future. Front. Cell. Neurosci. *13*, 141. https://doi.org/10.3389/fncel.2019.00141.

199. Friedrich, J., Giovannucci, A., and Pnevmatikakis, E.A. (2021). Online analysis of microendoscopic 1-photon calcium imaging data streams. PLoS Comput. Biol. *17*, e1008565. https://doi.org/10.1371/JOURNAL.PCBI.1008565.

200. Campos, P., Walker, J.J., and Mollard, P. (2020). Diving into the brain: deep-brain imaging techniques in conscious animals. J. Endocrinol. *246*, R33–R50. https://doi.org/10.1530/JOE-20-0028.

201. Rossi, M.A., Basiri, M.L., McHenry, J.A., Kosyk, O., Otis, J.M., Van Den Munkhof, H.E., Bryois, J., Hübel, C., Breen, G., Guo, W., et al. (2019). Obesity remodels activity and transcriptional state of a lateral hypothalamic brake on feeding. Science *364*, 1271–1274. https://doi.org/10.1126/science.aax1184.

202. Sheintuch, L., Rubin, A., Brande-Eilat, N., Geva, N., Sadeh, N., Pinchasof, O., and Ziv, Y. (2017). Tracking the same neurons across multiple days in Ca2+ imaging data. Cell Rep. *21*, 1102–1115. https://doi.org/10.1016/j.celrep.2017.10.013.

203. Scheller, K.J., Williams, S.J., Lawrence, A.J., Jarrott, B., and Djouma, E. (2014). An improved method to prepare an injectable microemulsion of the galanin-receptor 3 selective antagonist, SNAP 37889, using Kolliphor(®) HS 15. MethodsX *1*, 212–216. https://doi.org/10.1016/j.mex.2014.09.003.

STAR★METHODS

KEY RESOURCES TABLE

REAGENT or RESOURCE	SOURCE	IDENTIFIER
Antibodies		
NAPE-PLD	Abcam	RRID: AB_246951
pAMPK (Thr172)	Cell Signaling	RRID: AB_2535
pKv2.1	Gift from James Trimmer	Cat# Kv2.1-pS563, RRID:AB_2315785; Cat# Kv2.1-pS603, RRID: AB_2531883
u-opioid receptor	Abacm	RRID: AB_134054
a-Bungarotoxin (fluorescence conjugated)	Invitrogen	RRID: B13422 or B35450
Anti mouse f(ab) IgG H&L fragments	Abcam	RRID: AB_6668
DAPI Fluoromount G	SouthernBiotech	RRID: 0100-20
Normal donkey serum	Jackson ImmunoResearch	RRID: AB_2337258
Normal goat serum	Jackson ImmunoResearch	RRID: AB_2336990
Bacterial and virus strains		
GRAB ACh 3.0	WZ Biosciences	N/A
AAVrg-CAG-DIO-tdTomato	UNC Vector Core	N/A
AAV1-hSyn-iGABASnFR	Addgene	RRID:Addgene_112159
AAVrg-CAG-DIO-tdTomato	Addgene	RRID:Addgene_28306
AAV1-phSyn1-Flex-tdTomato-T2A-SypEGFP	Addgene	RRID:Addgene_51509
AAV9-hSyn-DIO-mCherry	Addgene	RRID:Addgene_50459
AAVrg-CAG-tdTomato	Addgene	RRID:Addgene_59462
AAV9-Ef1a-DIO-ChR2-EYFP	Addgene	RRID:Addgene_20298
AAV9-EF1a-DIO-ChR2-mCherry	Addgene	RRID:Addgene_20297
AAV9-EF1a-DIO-eNpHR3.0-EYFP	Addgene	RRID:Addgene_26966
AAV9-Syn-DIO-ChrimsonR-tdTomato	UNC Vector Core	N/A
AAVrg-EF1a-DIO-ChR2-mCherry	Addgene	RRID:Addgene_20297
AAV9-hSyn-DIO-EYFP	Addgene	RRID:Addgene_27056
AAV9-Syn-DIO-GCaMP6m	Addgene	RRID:Addgene_100838
AAVrg-Syn-jGCaMP7s	Addgene	RRID:Addgene_104487
Chemicals, peptides, and recombinant proteins		
Tracers - fluorescent retrobeads	Fisher Scientific	F8783
CFA	Sigma-Aldrich	F5881
Formalin	Fisher Scientific Company	F79500
Morphine sulfate	Sigma-Aldrich	M8777-250MG
Bicuculine	Sigma-Aldrich	14340-25MG
Paclitaxel	Thermo Scientific	AAJ62734MC
MLA	Tocris	1029
AFDX 116	Tocris	1105
Mecamylamine	Tocris	2483
Atropine	Sigma-Aldrich	1044990-50MG
DHBE	Tocris	2349
α-Bungarotoxin	Tocris	2133
CNQX	Tocris	1045
Acetone	Fisher Scientific Company	A18P-4
Naloxone	Sigma-Aldrich	BP548

(Continued on next page)

Continued

REAGENT or RESOURCE	SOURCE	IDENTIFIER
EVP 6124	ChemBlock	L14548
GW 6471	Tocris	4618
NESS 0327	Tocris	5746
PHA 543613	Sigma-Aldrich	PZ0135-25MG
PNU 120596	Tocris	2498
Meloxicam	Sigma-Aldrich	1379401
Dexamethasone	Sigma-Aldrich	D1756
Salts for aCSF, HEPES, NMDG	Sigma and Tocris	N/A
Critical commercial assays		
RNAScope Multiplex reagent kit	Advanced Cell Diagnostics	320851
3-plex Negative Control Probe	Advanced Cell Diagnostics	320871
3 plex Positive Control Probe	Advanced Cell Diagnostics	320881
Th	Advanced Cell Diagnostics	317621
Slc32a1	Advanced Cell Diagnostics	319191
Slc17a6	Advanced Cell Diagnostics	319171
Tac1	Advanced Cell Diagnostics	410351
Penk	Advanced Cell Diagnostics	318761
Pdyn	Advanced Cell Diagnostics	318771
Chat	Advanced Cell Diagnostics	408731
Sst	Advanced Cell Diagnostics	404631
Npy	Advanced Cell Diagnostics	313321
Chrm1	Advanced Cell Diagnostics	495291
Chrm2	Advanced Cell Diagnostics	495311
Chrm3	Advanced Cell Diagnostics	437701
Chrm4	Advanced Cell Diagnostics	410581
Chrm5	Advanced Cell Diagnostics	495301
Chrna5	Advanced Cell Diagnostics	31571
Chrna7	Advanced Cell Diagnostics	465161
Chrnb2	Advanced Cell Diagnostics	449231
Chrnb3	Advanced Cell Diagnostics	449201
Chrnb4	Advanced Cell Diagnostics	452971
Oprm1	Advanced Cell Diagnostics	315841
Cnr1	Advanced Cell Diagnostics	420721
Hcrtr1	Advanced Cell Diagnostics	466631
Glp1r	Advanced Cell Diagnostics	418851
Htr3a	Advanced Cell Diagnostics	411141
Drd2	Advanced Cell Diagnostics	406501
Cre-O1	Advanced Cell Diagnostics	474001
Experimental models: Organisms/strains		
Mouse: ChAT-Cre	Jackson Labs	6410
Mouse: Oprm1-Cre	Gift from Julie Blendy	N/A
Mouse: Chrna7-Cre	Jackson Labs	034808-UCD
Mouse: Gad2-Cre	Jackson Labs	10802
Software and algorithms		
Graphpad Prism v9	Graphpad Software	RRID: SCR_002798
ImageJ	NIH	RRID: SCR_002285
pCLAMP	Molecular Devices	RRID: SCR_011323

Continued

REAGENT or RESOURCE	SOURCE	IDENTIFIER
Mini Analysis	Synaptosoft	RRID: SCR_002184
MATLAB	Mathworks	RRID: SCR_001622
Cell Profiler	Cell Profiler	RRID: SCR_007358
Ethovision XT-11	Noldus	RRID: SCR_014429
Easy Electrophysiology	Easy Electrophysiology	RRID: SCR_021190
Clampfit	Molecular Devices	RRID: SCR_011323
NoRMCorre	Flatiron Institute	https://github.com/flatironinstitute/NoRMCorre
CNMF-E	GitHub	https://github.com/zhoupc/CNMF_E
CellReg	GitHub	https://github.com/zivlab/CellReg
EZCalcium	GitHub	https://github.com/porteralab/EZcalcium
Other		
2p imaging laser	Spectra Physics	Mai Tai BB
Syringe pump	Wolrd Precision Instrument	UMP3T
Optogenetic fiber	Doric	MFC_400/430-0.48_5mm_MF1.25_FL
Opto-pharmacology cannula	Doric	OmFC
Isoflurane	Covertrus	11695067772
Dental cement	Lang Dental	1404
Skull screws	PlasticsOne	0-80 1/16
LEDs	Doric	CLED_405 & CLED_465
Photometry digitizer	Tucker Davis Technologies	RZ5P
Femtowatt photoreceiver	Newport	2151
Cameras	Basler	acA1300-60
GRIN lens	Inscopix	1050-004597
10x objective	Olympus	UPLFLN10X
20x objective	Olympus	LCPLN20X
Sterilizer	Fine Science Tools	18000-45
Stereotaxic system	Kopf Instruments	962
Heating pad	Harvard Apparatus	72-0492
Drill	Foredom	K1070
Drill bit	Kyocera	105-0210L310
Injection syringe	Hamilton	1700 33G
Trephine	Fine Science Tools	18004-18
GRIN Lens holder	RWD Life Science	998-00201-00
SRO accolade	Zest Dental Solutions	91388-M
UV LED	SDI	5600202
Adhesive cement	Parkell	S380
Silicone Sealant	World Precision Instruments	KWIK-CAST
Electrophysiology amplifier	Molecular devices	Multiclamp 700A/Axopatch 200B
Electrophysiology digitizer	Molecular devices	Digidata 1440A
Optogenetic cables	Thorlabs	RJPFL4
595 nm LED (Thorlabs, M595F2)	Thorlabs	M595F2
Blue optogenetics laser	Shanghai Laser and Optics Century	T8_612
Power meter	Thorlabs	PM20A
Confocal microscope	Marianas	3i
2-Photon microscope	Leica	TCS SP5
Photometry minicube	Doric	FMC5_IE(400-410)_E(460-490)_F(500-540)_O(580-680)_S
Patch cord	Doric	MFP__m_FCM-MF1.25(F)_LAF

RESOURCE AVAILABILITY

Lead contact
Further information and requests for resources and reagents should be directed to and will be fulfilled by the lead contact, Daniel McGehee (dmcgehee@uchicago.edu).

Materials availability
This study did not generate new unique reagents.

Data and code availability
- All data reported in this paper will be shared by the lead contact upon request.
- This paper does not report original code.
- Any additional information required to reanalyze the data reported in this paper is available from the lead contact upon request.

EXPERIMENTAL MODEL AND STUDY PARTICIPANT DETAILS

Mouse lines
All procedures were conducted in accordance with the NIH guide for the care and use of laboratory animals, the American Veterinary Medical Association guidelines, and the guidelines from the International Association for the Study of Pain. The use of laboratory animals was approved by the Institutional Animal Care and Use Committee at the University of Chicago. Adult (>8 weeks, 25–35 g) male and female *WT* (C57BL6/J, Jackson labs), *ChAT-Cre* (Strain number: 006410, Jackson Labs), *Chrna7-Cre* (Strain number: 034808-UCD, MMRRC), *Oprm1-Cre* (gift of Julie Blendy, University of Pennsylvania), *Gad2-Cre* (Strain number: 010802, Jackson Labs) and *ChAT-Cre::Chrna7-Cre* were used in this study. These mice were bred at the University of Chicago. *Cre* expression specificity was verified using mRNA and immunohistological approaches for *ChAT-Cre* and *Gad-Cre* mouse lines, and mRNA and electrophysiological approaches for *Chrna7-Cre* and *Oprm1-Cre* mouse lines. The *ChAT-Cre::Chrna7-Cre* mouse line was verified by the absence of *Chrna7* mRNA in PPTg, *ChAT* mRNA in the vlPAG, and expression of *Cre* mRNA and in *Chrna7* mRNA expressing vlPAG neurons and *ChAT* mRNA expressing PPTg neurons. All experiments were conducted in mice that were heterozygous for *Cre* allele. Mice were group-housed with littermates of the same sex (2-5 animals per cage), given access to food and water *ad libitum*, and maintained on a 12 hr:12 hr light:dark cycle (lights on at 6:00 AM) at 23±1°C. Behavioral assays were conducted during the light cycle. All animals were monitored for appropriate gross health status daily for the entirety of the study. For *in vivo* experiments, we used randomly assigned age- and sex-matched litter-mate controls in experimental and control groups. All experiments were replicated in at least one additional independent group. Experimenters were blinded to the viral injection of the experimental groups for all optogenetic experiments. Optogenetic and behavioral experiments consisted of 5–11 mice per group, and *in vivo* and *ex vivo* physiology experiments consisted of 3-7 mice per group. Exact animal numbers are provided in the Figure legends. To assess sex differences, ANOVA was conducted to test for interaction between sex and antinociceptive effects of: a) optogenetic inhibition of vlPAG$^{Chrna7+}$ neurons and b) optogenetic excitation of PPTg^{ChAT+}→vlPAG neurons. We found no evidence of sex differences, as the interaction term was not significant assessing a) sex and optogenetic inhibition of vlPAG$^{Chrna7+}$ neurons yielded p=0.327, and b) sex and excitation of PPTg^{ChAT+}→vlPAG neurons yielded p=0.7894. Therefore, male and female mice were combined in the final groups. Animals were excluded only after post-hoc validation for virus expression and fiber optic placements. Multiple acute somatic pain assays were conducted within the same cohort of animals. However, tonic, chronic, and affective pain assays were conducted in separate animal cohorts. Repeated somatic pain assays did not alter baseline pain sensitivity by more than 1 standard deviation for the tested parameter. Mice were naive to the drug or the test, unless otherwise stated in the text and the figures (e.g. tolerance or conditioning experiments). This study did not use any tissue culture systems.

METHOD DETAILS

Surgeries
Stereotaxic injections and surgical procedures
All surgeries were conducted under aseptic conditions, and all surgical tools were sterilized using a glass bead sterilizer (FST sterilization tool 18000-45). A small animal stereotaxic surgery device (Kopf Instruments) was used to position viral injections and fiber-optic implants. Mice were anesthetized with isoflurane (2% induction, 1-1.5% maintenance), shaved using a trimmer, and placed on the stereotaxic apparatus. Body temperature was maintained at 37°C using a homeothermic heating pad (Harvard Apparatus). An ophthalmic ointment was used to maintain eye lubrication throughout the duration of the surgery. Prior to incision, mice were administered buprenorphine (Hospira, 0.05 mg/kg, s.c.) and bupivacaine (Hospira, 1 mg/kg s.c. at the site of incision). The surgery site was sterilized with betadine solution and an incision was made on the top of the skull using surgical blades. A Foredom micromotor drill was used with a drill bit (Kyocera 105-0210L310) to drill a hole (∼600-800μm diameter) in the skull. Care was taken to prevent bleeding, and sterilized cotton tip applicators were used to limit any bleeding that occurred. A blunt Hamilton syringe (1700 series,

33G) was used for all viral and fluorescent microsphere injections. The injection volume and flow rates were controlled using a syringe pump (World Precision Instrument, UMP3T). For viral and microsphere injections, 400 nL fluid was injected at a rate of 150 nL/min, unless otherwise stated. After the injection needle reached the target DV location, the needle was gently moved dorsoventrally for ~50μm to create a 'pocket' for viral injection. After injection, the needle was held in place for ~7mins to ensure adequate viral diffusion and minimize viral solution from being suctioned up due to backpressure while removing the needle. The injection needle was slowly withdrawn 5-10 min after the end of the infusion.

Injection coordinates in mm relative to Bregma for various brain regions were: vlPAG - AP: -4.75, ML: 0.55, DV: -2.70; PPTg - AP: -4.60, ML: 1.10, DV: -3.50; LDTg - AP:-5.20, ML:0.50, DV:3.5; RVM - AP: -5.70, - 5.50, -5.90 ML: 0.00, DV: -5.90. The coordinates were scaled based on the length variations of the AP distance between the Bregma and the Lambda. This distance was divided by 4.21 (standard distance) and the ratio was used to scale the coordinates.

For photometry and optogenetics experiments, fiber optic cannulas (MFC_400/430-0.48_5mm_MF1.25_FL, Doric) were implanted using a cannula holder stereotaxic attachment (Kopf Instruments). Cannulas were lowered into the brain at a rate of 300 μm/min. Two skull screws (0-80 1/16, PlasticsOne) were affixed to separate plates of the skull, and dental cement (Lang Dental) was used to affix the cannulas and the skull and the screws to form a headcap. Cannula placement coordinates in mm relative to Bregma are as follows: vlPAG: AP: -4.75 AP, ML: 0.55, DV: -2.50; PPTg: AP: -4.60, ML: 1.10, DV: -3.30. Post-surgery, 0.5mL sterile saline and Meloxicam (Sigma, 5 mg/kg, s.c.). Animals were placed on a heating pad and monitored until they fully recovered from the anesthetic. Mice were allowed to recover, and the virus was allowed time to express for three weeks before behavioral assays. Injection coordinate choices for PPTg and vlPAG were guided by preliminary anatomical experiments exploring the density of cholinergic innervation in the vlPAG.

Viral approaches for anatomical tracing, immunohistochemistry, and slice electrophysiology For retrograde labeling of cholinergic inputs to vlPAG, we injected 200nL of retrogradely transported virus AAVrg-CAG-DIO-tdTomato (Addgene: 28306) unilaterally into the vlPAG of *ChAT-Cre* mice. For retrograde labeling of inputs to the vlPAG for immunohistochemical analysis, 200nL of fluorescent microspheres (FluoSpheres Carboxylate-Modified Microspheres, dark red fluorescent, 660/680, Fisher Scientific, F8783, diluted 1:4 in saline) were injected unilaterally into the vlPAG of WT mice. To label PPTg^{ChAT+} terminals in vlPAG, in a *ChAT-Cre* mouse line were unilaterally injected 200nL of AAV1-phSyn1-Flex-tdTomato-T2A-SypEGFP (Addgene: 51509) into the PPTg. To label vlPAG$^{Chrna7+}$ neurons for slice electrophysiology recordings, AAV9-hSyn-DIO-mCherry (Addgene: 50459) was injected bilaterally into the vlPAG of *Chrna7-Cre* mice. For electrophysiological recordings of vlPAG→RVM projections, AAVrg-CAG-tdTomato (Addgene: 59462) was injected into the RVM of *Chrna7-Cre* mice. In a subset of these experiments, we also injected AAV9-Ef1a-DIO-ChR2-EYFP (Addgene: 20298) in the vlPAG to optogenetically activate vlPAG$^{Chrna7+}$ neurons, while recording from vlPAG→RVM projecting neurons. In slice electrophysiology experiments that tested cholinergic synaptic transmission from PPTg^{ChAT+}→vlPAG, we injected AAV9-EF1a-DIO-ChR2-mCherry (Addgene: 20297) bilaterally in the PPTg of *ChAT-Cre* mice. To test GABAergic synaptic transmission from vlPAG$^{Chrna7+}$ neurons to neighboring vlPAG neurons, AAV9-EF1a-DIO-ChR2-mCherry was injected bilaterally into the vlPAG. To explore overlap between vlPAG$^{Chrna7+}$ neurons and vlPAG→RVM projecting neurons, Cre-dependent EGFP was injected in vlPAG of *Chrna7-Cre* mice and AAVrg-CAG-tdTomato in the RVM at 3 locations along the AP-axis (see stereotaxic injections and surgical procedures).

Viral injections and cannula implants for behavioral optogenetic assays

To optogenetically inhibit vlPAG^{Oprm1+} neurons, we injected AAV9-EF1a-DIO-eNpHR3.0-EYFP (Addgene: 26966) in the vlPAG of *Oprm1-Cre* mice and implanted an optical cannula in vlPAG. To optogenetically excite PPTg^{ChAT+}→vlPAG terminals, we injected AAV9-EF1a-DIO-ChR2-mCherry in the PPTg of *ChAT-Cre* mice and implanted an optical cannula in the vlPAG for terminal excitation. A similar method was employed to optogenetically activate LDTg^{ChAT+}→vlPAG terminals, but the virus was injected in the LDTg instead of PPTg. In these surgeries, we implanted the cannula ipsilateral to the viral injection site. For optogenetic manipulation of vlPAG$^{Chrna7+}$ activity, a *Chrna7-Cre* mouse line was used, AAV9-Ef1a-DIO-eNpHR3.0-EYFP or AAV9-EF1a-DIO-ChR2-mCherry was injected, and an optical cannula was implanted into the vlPAG to inhibit or excite, respectively. For optogenetic manipulation of vlPAG^{Gad+} neurons, a *Gad-Cre* mouse line was used, and AAV9-Ef1a-DIO-eNpHR3.0-EYFP or AAV9-Syn-DIO-ChrimsonR-tdTomato (UNC Vector Core) was injected, and an optical cannula was implanted into the vlPAG to inhibit or excite, respectively. To optogenetically activate RVM projecting vlPAG$^{Chrna7+}$ neurons, a retrogradely transported AAVrg expressing ChR2 in a Cre-dependent manner (Addgene: 20297) was injected into the RVM of *Chrna7-Cre* mice at 3 locations along the AP-axis (see stereotaxic injections and surgical procedures). Optical cannula was implanted in the vlPAG for cell body optogenetic activation at 20hz. Unless otherwise stated, AAV9-hSyn-DIO-EYFP (Addgene: 27056) was used as a control probe for behavioral experiments. For optogenetic experiments, the optical fiber was implanted ~100-150 μm above the virus injection site.

Viral injections and cannula implants for fiber photometry assays

To monitor the activity of vlPAG^{Oprm1+} neurons, in an *Oprm1-Cre* mouse line, we injected AAV9-Syn-DIO-GCaMP6m (Addgene: 100838) and implanted an optical cannula into the vlPAG. Similar approaches were used to monitor the activity of vlPAG$^{Chrna7+}$ and vlPAG^{Gad+} neurons using fiber photometry using *Chrna7-Cre* and *Gad-Cre* mouse lines, respectively. To monitor ACh levels in vlPAG, in WT mice, we injected AAV9-hSyn-ACh4.3 (GRAB$_{ACh 3.0}$, WZ Biosciences) and implanted an optical cannula into the vlPAG. To monitor GABA levels in vlPAG, in WT mice, we injected AAV1-hSyn-iGABASnFR (Addgene: 112159) and implanted an optical cannula into the vlPAG. For photometry experiments, the optical fiber was targeted ~100-150μm above the virus injection site.

Viral injections and cannula implants for simultaneous fiber photometry and optogenetic assays

To simultaneously activate PPTg^{ChAT+}→vlPAG terminals in the vlPAG and monitor the activation-induced ACh release, in *Chat-Cre* mice, we injected GRAB$_{ACh\ 3.0}$ in the vlPAG and *Cre*-dependent ChrimsonR in the PPTg. The optical cannula was implanted in the vlPAG. To simultaneously activate PPTg^{ChAT+}→vlPAG terminals while monitoring the activity of vlPAG$^{Chrna7+}$ neurons, in *Chat-Cre::Chrna7-Cre* mice, we injected *Cre*-dependent ChrimsonR in the PPTg and *Cre*-dependent GCaMP6m in the vlPAG. The optical cannula was implanted in the vlPAG. To simultaneously activate vlPAG$^{Chrna7+}$ neurons while monitoring the neuronal activity of vlPAG→RVM projection neurons, in *Chrna7-Cre* mice, we injected *Cre*-dependent ChrimsonR in the vlPAG and AAVrg-Syn-jGCaMP7s (Addgene: 104487) in the RVM. The optical cannula was implanted in the vlPAG.

Viral injections and drug infusion cannula implant for opto-pharmacology assays

For focal drug infusion combined with optogenetic stimulation of PPTg^{ChAT+}→vlPAG terminals, we expressed *Cre*-dependent ChR2 in the PPTg in *Chat-Cre* mice and implanted a guide cannula into the vlPAG. A focal infusion and optical cannula (OmFC, Doric) was implanted through the guide cannula to optogenetically stimulate terminals after drug infusion in the same location. Optogenetic stimulation was conducted 15 mins after drug infusion.

Viral and GRIN lens approaches for *in vivo* imaging assays

For calcium imaging experiments, WT mice were injected with Dexamethasone (0.6mg/kg, Sigma-Aldrich, D1756) before anesthesia for surgery to minimize lens implantation-induced tissue swelling and inflammation. We performed a craniotomy using a trephine (Fine Science Tools, 18004-18) to create a ~1.5 mm diameter hole in the skull. We carefully removed the dura using a bent 30G syringe needle and irrigated the brain surface with sterile aCSF to prevent drying. We then injected 350nL of AAV9-Syn-GCaMP6m in the vlPAG at a rate of 50nL/min in two locations in mm relative to Bregma: AP: -4.75, ML: 0.65, DV: -2.80 and DV: -2.4. These locations are slightly lateral, dorsal, and ventral to the final GRIN lens implantation site. These injection locations were chosen because preliminary experiments suggested the area immediately above the injection track displayed strong autofluorescence, presumably due to tissue inflammation or death. To allow for viral diffusion, the syringe was removed 10 mins after the injection. Before implanting the grin lens, incisions in a cross-pattern were made on the brain's surface using a surgical blade. GRIN lens (0.6 mm diameter, 7.3mm length, Inscopix, 1050-004597) was implanted using a GRIN Lens holder (RWD Life Science, 998-00201-00) at a rate of 0.15 mm/min. The lens was retracted 200 μm every 1 mm of implantation to allow the tissue to settle around the lens. The GRIN lens was placed ~100–300 μm above the imaging plane. SRO accolade (Zest Dental Solutions) was applied to the base of the GRIN Lens and was cured for 2 mins with a high-intensity UV LED (SDI). The lens was bonded to the skull with adhesive cement (C&B, S380 Metabond Quick Adhesive Cement System) and allowed to harden. Three skull screws were inserted on three separate skull plates to form a triangular pattern around the lens. The lens holder was then removed, and dental Cement (Zest Dental) was applied to the surrounding area of the skull, covering the skull screws. A titanium head plate 4 cm x 1 cm with a 0.75 cm diameter hole was affixed to the head cap with the hole centered above the GRIN Lens. Kwik Cast Silicone Sealant (WPI) was used to fill the hole and cover the GRIN Lens for protective purposes. Animals were monitored daily for changes in health and weight.

After experiments, all animals were checked for the location of viral injection and cannula placement using histological methods and confocal imaging. Animals with inappropriate viral or cannula placement were excluded from analysis.

Slice electrophysiology

After viral injections and behavioral assays, mice were deeply anesthetized using isoflurane (Baxter). After checking breathing rate (~1 breath per sec) and for lack of nocifensive responses, mice were transcardially perfused using an ice-cold NMDG-slicing solution (~20ml), containing: 92 mM NMDG, 2.5 mM KCl, 1.25 mM NaH$_2$PO$_4$, 30 mM NaHCO$_3$, 20 mM HEPES, 25 mM glucose, 2 mM thiourea, 5 mM Na-ascorbate, 3 mM Na-pyruvate, 0.5 mM CaCl$_2$·4H$_2$O, and 10 mM MgSO$_4$·7H$_2$O. pH was titrated to 7.3–7.4 with concentrated HCl, and osmolarity was measured to be 300–310 mOsm. After perfusion, the mice were decapitated, and the brains were extracted, dissected, and sliced in the same ice-cold NMDG slicing solution bubbled continuously with 95%-O$_2$/5%-CO$_2$.

Acute midbrain coronal slices (250μm thick) containing the vlPAG were taken on the vibratome (VT100S, Leica). These slices were transferred to NMDG solution at 32°C for <12 mins. Then these slices were transferred to HEPES containing recovery solution, which contained: 92 mM NaCl, 2.5 mM KCl, 1.25 mM NaH$_2$PO$_4$, 30 mM NaHCO$_3$, 20 mM HEPES, 25 mM glucose, 2 mM thiourea, 5 mM Na-ascorbate, 3 mM Na-pyruvate, 2 mM CaCl$_2$·4H$_2$O, and 2 mM MgSO$_4$·7H$_2$O. In the HEPES solution, slices rested for at least 60 mins before each recording. From each animal, 2-3 vlPAG slices were used for experiments. Opsin and fluorophore-containing slices were kept under an optically opaque wrap.

For electrophysiological recordings, the slices were transferred to an upright microscope (Axioskop, Zeiss). Neurons were visualized under infrared illumination with a 40x water-immersion objective equipped with infrared-differential interference contrast (IR/DIC) and epifluorescence video microscopy. A light source (XCite, Excelitas) coupled to excitation filters (470/40 nm and 560/40 nm bandpass) through the fluorescent port of the microscope was used to search for fluorescent neurons and optogenetic activation of opsins including ChR2, ChrimsonR, or eNpHR 3.0 with light pulses. Light pulses were triggered by pCLAMP via TTL pulses to a shutter (LS2, Uniblitz) through the Master-8 interface (A.M.P.I.). Optical power intensity through the microscope objective was set to ~4mW/mm^2 using a photodiode power sensor (S120C, Thor Labs). Optical pulse duration and frequencies were guided by *in vivo* experiments and pilot data collected using slice electrophysiology. Retrogradely or virally labeled neurons were visualized using fluorescence microscopy, and the patch pipette was guided to the neurons for whole-cell/cell-attached recordings using simultaneous

GFP/tdTomato fluorescence and DIC illumination. This combined visualization was critical when recording from vlPAG, and PPTg neurons, given that cell morphology was challenging to visualize using DIC illumination in these brain regions.

Recording external solution, artificial cerebrospinal fluid (aCSF) contained: 119 mM NaCl, 2.5 mM KCl, 1.25 mM NaH$_2$PO$_4$, 24 mM NaHCO$_3$, 12.5 mM glucose, 2 mM CaCl$_2$·4H$_2$O, and 2 mM MgSO$_4$·7H$_2$O superfused at ~2 ml/min. The intracellular recording solutions contained: 145 mM K-Gluconate or Cs-Gluconate (if monitoring synaptic currents), 10 mM HEPES, 1 mM EGTA, 2 mM Mg-ATP, 0.3 mM Na$_2$-GTP, and 2 mM MgCl$_2$ (pH 7.3 adjusted using Tris base, osmolarity of 290–300 mOsm adjusted using sucrose). These experiments were performed at room temperature (~23°C). Intracellular or external aCSF solutions were backfilled in the recording pipettes for whole-cell or cell-attached recordings. After recording, slices were fixed in PFA to confirm injection location and viral expression using confocal microscopy. If the majority of viral expression was outside the intended region, the data were excluded from the analysis.

Signals were amplified with a Multiclamp 700A/Axopatch 200B amplifier, digitized with Digidata 1440A, and controlled with pCLAMP 9 software (Molecular Devices). Data were sampled at 10 kHz and low pass filtered at 1 kHz. Whole-cell patch-clamp recordings were achieved with borosilicate patch pipettes containing the microelectrode (3–6 MΩ) pulled on a Flaming/Brown micropipette puller (model P-97, Sutter Instrument, Novato, CA). Patch pipettes with higher resistance (5-7 MΩ) were used for cell-attached recordings to minimize accidental whole-cell access. In circumstances when cell-attached recordings transitioned to whole-cell recordings, the data were discarded.

To isolate and identify the neurotransmitters mediating optogenetically evoked synaptic currents, we used the following antagonists as necessary: CNQX (20µM), bicuculline (20µM), MLA (10nM), Atropine (1µM), α-bungarotoxin (100nM). Where necessary, DMSO or Kolliphor HS 15 were used to dissolve drugs and control solutions contained the same diluent concentrations. Only one cell from each slice was recorded for experiments that required drug perfusion. The recorded optically-evoked post-synaptic currents (oPSCs) had short constant latency, suggesting the monosynaptic nature of these synaptic responses. For these oPSC measurements, the variance in 10 oPSC rise-time was monitored. The approximate latency was ~7 ms. To monitor the effects of α7 nAChR activation on vlPAG$^{Chrna7+}$ neuronal physiology, EVP-6124 (2 nM) was bath perfused. This concentration was chosen given the known pharmacokinetics of EVP-6124 in mice.[74]

Cell-attached recordings of action potential frequency were conducted in on-cell configuration with a ~GΩ seal resistance in voltage clamp (0mV) mode with aCSF in patch pipette. Data were excluded if any run-down was observed during the recording. For cholinergic receptor synaptic communication, cells were held at -70mV in whole cell voltage clamp mode. For GABAergic synaptic transmission, cells were held at 0mV. Response sizes of oPSCs were calculated by baseline-subtracting and averaging 10 traces together, then calculating the peak amplitude in a 20ms window after the light pulse. When monitoring sEPSCs and sIPSCs, the currents were separated using -70mV and 0mV holding potentials, respectively. Spontaneous synaptic events were detected using MATLAB's *findpeaks* function with prominence >3 median absolute deviation of baseline noise, roughly corresponding to 5 pA amplitude, <0.75 ms rise time, and >3 RMS noise picocoulomb charge transfer as calculated using the area under the curve, roughly resulting in events lasting longer than 5ms. Identified sEPSCs and sIPSCs were cross verified using Easy Electrophysiology software and visually verified by the experimenter.

When testing for the involvement of PPARα signaling cascade, GW6471 (100nM) was included in the HEPES solution and aCSF to preincubate the slices and block the PPARα signaling cascade well before activation of α7 nAChRs using EVP-6124. The on-cell action potential firing rates were quantified by threshold crossing using MATLAB's *findpeaks* function and visually verified. These were binned according to described time intervals and normalized to baseline where necessary. Following stable 5 min whole-cell recordings, drugs or optogenetic stimulation effects were tested. In a subset of experiments, we expressed ChR2-mCherry on vlPAG$^{Chrna7+}$ neurons to use optogenetic stimulation after EVP-6124 induced a decrease in firing rate to test for neuronal action potentials.

For whole-cell excitability experiments, cells were recorded in current-clamp configuration and were allowed to stabilize for 5-10 min after establishing whole-cell access. Action potential voltage and current thresholds were calculated based on the first spike elicited by a slow current ramp protocol performed in current-clamp configuration (200pA over 250ms). Spike threshold was calculated as the first voltage value corresponding to the time derivative of the voltage trace greater than 5mV/ms.

To calculate the relationship between firing rate and current injection, the number of action potentials were counted per current step, using 25pA increments of 1s duration. Input resistance was assessed by injecting a negative current step of -50pA for 500ms duration.

In measurements of chronic pain-induced changes in cellular excitability, mice were sacrificed five days after CFA or saline injection in the hind paw. CFA or saline administration was counterbalanced within littermates. CFA's hyperalgesic effects were behaviorally verified on the day before electrophysiological recordings.

Data were only included from recordings with series resistance <30 MΩ and where input resistance or series resistance varied <25%. All batches of virally administered opsins employed in the study were functionally tested using slice electrophysiology. Data were primarily analyzed using Clampfit (Molecular Devices) and custom scripts in MATLAB. We aligned the data when the perfusion was switched to the drug-containing aCSF or other manipulations instead of the peak of monitored effects. All chemicals were purchased from Tocris or Sigma. The number of cells and animals employed for each experiment are included in the Figure legends.

Optogenetics

For optogenetics experiments, mice were tethered to an optical fiber cable with an inbuilt rotary joint (RJPFL4 outer diameter 1.25mm, core diameter 400μm, ThorLabs). To activate eNpHR 3.0 opsin, we used a 595 nm LED (Thorlabs, M595F2) to deliver constant orange light. To activate ChR2, we used pulsed blue light (473nm) delivered using a DPSS laser (Shanghai Laser & Optics Century Co., Ltd.). Pulses were triggered using Master-9 Pulse Stimulator (A.M.P.I.). To activate ChrimsonR, we used 595 nm LED pulsed using LED Driver and Doric Synapse Studio (Doric systems). Unless otherwise stated, we used 20Hz pulse frequency and 10ms pulse duration for pulsed opsin activation. In all optogenetic experiments, the light at the tip of the cannula was adjusted to ~5mW (10mW/mm^2) peak power at the desired wavelength using a power meter (Thorlabs, PM20A).

All behavioral assays were conducted four weeks after viral and cannula surgeries within a sound-attenuated room at ~23°C. The animals were acclimatized and habituated to the experimental room, experimenter handling, and optical tethers in their homecage for at least 30 mins during the five days prior to the start of experiments. On the day of the experiments, the animals were habituated to the experimental rooms for at least 30 mins before the experiments. Unless otherwise stated, PPTg^{ChAT+}→vlPAG projections were stimulated for 10 mins before acute pain assays. vlPAG$^{Chrna7+}$ and vlPAG^{Oprm1+} neurons were activated or inhibited immediately before the acute pain assay. Recovery was conducted on the subsequent day for all experiments to prevent residual effects of optogenetic or drug manipulations. Mice were tethered to the optical cables during the baseline and recovery assays. The behavioral apparatus was cleaned with a 70% alcohol solution and dried after each session. Experimenters were blinded to opsin or control fluorophore expression. Movements were video recorded using a camera (Basler) and Ethovision XT-16 software (Noldus) for later verification as necessary. During combined optogenetics and real-time place preference assay, the lasers were triggered based on Master-9 output, which occurred when the mice were detected within the optogenetic stimulation-paired chamber. The real-time location of mice was detected using a camera (Basler) interfaced with a computer (Dell Computers) running Ethovision XT-16 (Noldus). Ethovision sent a TTL output using Noldus IO box to the Master-9 pulse generator based on mouse location. In our experiments, we did not observe an interaction tested by repeated-measures ANOVA in antinociceptive effects and the laterality of the paw in vlPAG$^{Chrna7+}$ optogenetic inhibition or PPTg^{ChAT+}→vlPAG terminal excitation experiments. Hence, we pooled the data obtained from both hind paws. Mechanical thresholds or thermal latencies were measured three times for each mouse.

We used ex vivo slice electrophysiology and in vivo fiber photometry to verify opsin function and assess action potential fidelity. For ChR2 and ChrimsonR, optogenetic 10ms pulses at 1, 2, 4, 8, 16, 20, and 40 Hz were tested using slice electrophysiology in the expected neuron type. eNpHR 3.0 was tested using continuous 1s pulse delivery after step current injections that induced action potentials. ChrimsonR and eNpHR 3.0 were tested *in vivo* using GCaMP6 and GRAB$_{ACh\,3.0}$. We observed that eNpHR 3.0 reliably decreased spontaneous GCaMP6 dynamics during continuous light delivery, and ChrimsonR increased GCaMP6 fluorescence in *Oprm1-Cre*, *Gad-Cre*, and *Chrna7-Cre* mice experiments and increased ACh release in the vlPAG in a frequency-dependent manner in *ChAT-Cre* mice. 10ms pulses at 1, 2, 4, 8, 16, 20, and 40Hz were tested for ChrimsonR. For behavioral opto-pharmacology, we injected the antagonists of the tested AChR 15 mins before optogenetic stimulation in both focal and systemic antagonist assays. The recovery and subsequent AChR antagonist assays were conducted 1 and 2 days after antagonist infusion.

Each viral lot was tested at least once using slice electrophysiology and immunohistochemistry to verify function and expression in the appropriate neuronal phenotype. Post experiments, the viral expression cell-type and cannula placement were tested in all experimental animals.

Fiber photometry

A TDT-Doric system was used for our fiber photometry experiments with a lock-in amplifier and processor to drive and demodulate signals (TDT RZ5P). The experimental setup allowed us to simultaneously deliver 405 nm, 465 nm, and 594 nm light and monitor 525 nm light using a 5-port fluorescent minicube (FMC5_IE(400-410)_E(460-490)_F(500-540)_O(580-680)_S, Doric). The monitored light was sent to a femtowatt photodetector (Newport Model 2151), which sent the electrical signals to the RZ5P processor for demodulation. The setup allowed monitoring of both calcium-dependent and independent signals using different modulation frequencies. Excitation light with a wavelength of 465 nm was 'Calcium dependent' and modulated at 331Hz, and isosbestic control calcium-independent 405 nm wavelength light was modulated at 211 Hz driven using LEDs and LED Driver from Doric. The output power for individual wavelengths was ~20 μW as measured using a power meter (Thorlabs, PM20A). Since the signal was sampled at 1017.3 Hz, we ensured that no signal was modulated at a frequency greater than half the sampling frequency to prevent aliasing errors. The receiver power levels for the demodulated signal were matched for the calcium-dependent and independent signals. Matching power levels required ~5x light power output from the 405 nm LED. The demodulated signal was low pass filtered at 20 Hz at sixth order. Animals were tethered to a patch cord (0.48NA, 400 μm core diameter, Doric) using a freely pivoting rotary joint and gimbal holder (Doric Lenses). Synapse software (TDT) was used to interface with the RZ5P system to log data, timestamp events using TTL loggers, and control the LEDs. The 595nm wavelength LED (Thorlabs) for activating ChrimsonR, or eNpHR 3.0, was driven using Thorlabs LED driver and interfaced directly with the RZ5P system and Synapse software to deliver precise time-locked stimulation. To inhibit neurons using eNpHR 3.0, we continuously delivered the 595nm LED light. To activate neurons using ChrimsonR, we pulsed 595nm light at a frequency of 20Hz and pulse duration of 10ms, unless otherwise stated. During experiments where we activated PPTg^{ChAT+}→vlPAG terminals while monitoring vlPAG$^{Chrna7+}$ neurons, we conducted RHS assays every 3 mins to correlate changes in pain sensitivity and vlPAG$^{Chrna7+}$ neuronal activity induced by PPTg^{ChAT+}→vlPAG terminal activation. When monitoring

vlPAG → RVM projection neurons while activating vlPAG$^{Chrna7+}$ interneurons, 595nm LED was pulsed at 20Hz with a pulse duration of 10ms. For these opsin activation experiments, the peak power output for opsin activation was ~5mW (10mW/mm^2).

Habituation to the apparatus and cleaning between tests was identical to optogenetic experiments above. Generally, individual photometry sessions lasted ~30 mins. Baseline spontaneous fluorescence activity was recorded during open-field behavior where the movements of the mice were recorded using an overhead camera (Basler). We did not find the movement duration, velocity, or distance correlated with any of the photometry signals that we monitored. Indeed, a recent paper has demonstrated that activating or inhibiting PPTg^{ChAT+} neurons does not alter movement.[55,193,194] Stimuli evoked behaviors, and the associated changes in neuronal activity, were captured using two orthogonally positioned cameras allowing for a temporal precision of ~16ms. When monitoring responses of vlPAG$^{Chrna7+}$ neurons to noxious and salient stimuli, the test stimuli were presented in groups, and a minimum of 30 mins were given between testing of different stimuli.

The data were analyzed using MATLAB according to published protocols.[195,196] First, the first 5-secs of the recording were removed due to observed opto-electrical artifacts that could contaminate the fit parameters. The photo-bleaching of GCaMP over long sessions was removed using a double exponential fit to the entire dataset. We subtracted the calcium-independent signal from the calcium-dependent signal to reduce movement or hemodynamic artifacts. To that end, a smoothed 405 nm isosbestic signal was fitted to the 465 nm signal using linear regression to obtain fitting coefficients. Care was taken to ensure that the fitting coefficients agreed with expectations, i.e., no erroneously negative coefficients existed, and unique outliers did not dominate the fit. In instances where the patch cord came loose during recordings, data were analyzed in separate epochs where the patch cord was connected optimally to ensure consistency of the regression coefficients. Using the fitting coefficients, the 'fit 405nm' signal was calculated, subtracted, and divided from the 465nm signal to obtain a ΔF/F (=[F_{465}-F_{fit405}]/ F_{fit405}). A robust Z score based on the median ΔF/F was calculated for the concatenated ΔF/F data for all sessions for individual mice to facilitate comparison across mice and sessions. This robust z-score was calculated by first removing the high amplitude events (>2x median absolute deviation) and identifying the median of the filtered trace. This median was subsequently used to normalize the ΔF/F. Unless otherwise stated, the peri-event fluorescence traces were analyzed 2s prior to and 4s after the monitored event. Baseline activity was calculated from the time interval ranging from 2s to 1s before the event. This baseline activity was used to compare across animals and calculate the robust Z score. Generally, the area under the curve and peak amplitude parameters were used to evaluate changes in neuronal activity. The area under the curve was calculated using the trapezoidal method for integrals (*trapz*). Where applicable, peak, mean, and minimum fluorescence were calculated from the 2s prior to the event and from the event to 4s post the event. To calculate effects of a drug, mean fluorescence values were taken from 10 min to 5 min prior to the drug injection and from 25 min to 30 min after the drug injection, unless otherwise stated. In some instances, the mean ΔF/F value and the frequency and amplitude of transients were calculated using the *findpeaks* command in MATLAB with a prominence value of 2.9 x standard deviation of the data. These results were compared to another method where we took the first order time derivative of the ΔF/F signal and annotated transients above 5% ΔF/F per 0.01s. If significant differences were observed in the frequency of transients between these two measurement approaches, we manually verified the transients in signal or discarded data. Three conditions were used to identify GCaMP6/ GRAB$_{ACh 3.0}$/iGABASnFR signals as true physiological signals: 1. The signal should show spontaneous activity under baseline conditions, which was generally reduced under isoflurane anesthesia. 2. The rise time should be much more rapid than the decay time for transients corresponding to behavioral responses or spontaneous transients. And the transient decay time should be representative of the time constant of the physiological response and the indicator used, and 3. The standard deviation of the signal should correspond to *at least* 5% ΔF/F consistently for the duration of the recording period. As additional verification of the signals for GRAB$_{ACh 3.0}$ experiments, we used M3 mAChR antagonist: scopolamine (3 mg/kg, Tocris) and acetylcholine esterase inhibitor: donepezil (6 mg/kg, Tocris) to confirm that the signal was representative of acetylcholine. The decrease in activity associated with nocifensive behaviors was observed in those experiments after trial averaging. In a single trial, the nocifensive behaviors were associated with a 'pause' in ACh release. In formalin assays, we normalized the fluorescence to 15 mins of pre-formalin administration baseline. Generally, we temporally aligned the data to the time when a drug was injected, or manipulation was conducted and not to the peak monitored effects. Code that supports the analysis will be made available from the corresponding author upon reasonable request.

In vivo calcium imaging

Mice first underwent surgery for viral injection, GRIN lens implant, and headplate attachment as described above. These mice were individually housed after the surgeries. Three weeks after the surgery, each mouse was habituated to the head fixing apparatus (custom-made) over one week. For the first day, mice were allowed to freely explore the apparatus for 15 mins. On days 2-5, mice were head-fixed in the apparatus multiple times a day for increasing time intervals ranging from 5 to 30 mins with sucrose rewards during head fixation. On days 6-7, mice were head fixed to the apparatus for 30 mins without sucrose rewards. On day 7, we selected a particular field of view (FOV) by adjusting the imaging plane (z-axis) through the GRIN lens using a two-photon microscope imaging system (Leica SP-5 equipped with Mai Tai (SpectraPhysics) 710-990 nm broadband laser). Multiple FOVs in different wavelength channels were collected using confocal and two-photon imaging capabilities along different z-positions. This data was logged, and 3D reconstructed to aid in capturing images from the same FOV during the experiments. The z-position of the objective

relative to the GRIN lens was controlled using LAS AF software. The FOV selected for imaging was where most cells showed pain evoked responses. Throughout the imaging session, we just used one FOV to capture all neuronal data. Neurons above and below the FOV were excluded from the analysis.

To image calcium dynamics, an excitation wavelength of 910 nm was used. The microscope was equipped with resonant scanners allowing for 512 x 512 image acquisition at 32 Hz. For photon detection, nondescanned GaAsP photomultiplier tubes (PMT) were used. The PMT photodetectors with adjustable voltage, gain, and offset were kept consistent across animals and imaging sessions. The microscope was interfaced with the LAS AF software system on a computer (HP) to tune the 2p laser power, adjust the gain, and acquire data. The software also allowed control of the z-position of the objective, as mentioned earlier. These software settings corresponded to peak laser intensity: $\sim$1.12W; PMT voltage gain: 1250V, offset: 0%, scan resolution: 512 x 512, zoom: 1.2x, aspect ratio, 1:1. An inverter (LSM technologies) was used to convert the inverted microscope to an upright microscope for *in vivo* imaging. A long working distance 20x air objective was used in these imaging experiments (Olympus, LCPLN20X, 0.45 NA, 8.3 mm WD). This microscope was also capable of confocal imaging with 488 nm Argon laser and GaAsP PMT detectors. These were used to identify the surface of the lens and the potential focal plane, which was subsequently fine-tuned using 2p excitation. When necessary, fields of view and the laser scanning direction were manually rotated to superimpose previous fields of view. To accomplish this, scratch marks on the head plate were used to orient the appropriate FOVs. Prior to each imaging session, FOVs were manually aligned with standard deviation projections from the previous imaging session to ensure the same cells were imaged on consecutive days. Images were collected as 12-bit tiff files at a resolution of 512 x 512 pixels ($\sim$455μm x $\sim$455μm) at $\sim$32 Hz.

The experimental procedure was as outlined in Figure 5. Mice were head-fixed during each test day, and cells were visualized first using confocal imaging and then 2p imaging. After 10 mins of head fixing, spontaneous activity was recorded for 10 mins. Subsequently, a noxious stimulus was administered to the tail, which consisted of mechanical and thermal stimuli. Thirty secs of data were captured, during which the noxious stimuli were administered. Data were truncated to 2s before and 4s after applying noxious stimuli to aid in data storage and subsequent analysis. Behavioral data was logged by two independent cameras at 60fps to synchronize recordings of nocifensive responses and the neuronal activity with an error rate of $\sim$1-2 frames (15-30 ms). For the mechanical stimuli, we applied a tail pinch using forceps calibrated using a force transducer for consistent application of mechanical force (Sparkfun SEN-09376). A high-intensity infrared heat source was used for consistent application of radiant heat (BigLasers). Both mechanical and thermal stimuli were applied to the tail of the mice. During separate experiments not conducted during in vivo imaging, we also tested the latency to paw flick using a radiant heat source assay in the same mice. These responses were logged to compare the progression of the pain state. Drugs, including morphine (10mg/kg) and EVP 6124 (0.3mg/kg), were injected subcutaneously, and 15 mins following injection, spontaneous and noxious stimuli evoked activity were once again monitored using the 2-photon microscope. This method was repeated after induction of chronic neuropathic pain via paclitaxel injection, following morphine tolerance paradigm, and finally after EVP-6124 administration. Successful development of chronic neuropathic pain and opioid tolerance were verified using the RHS assay.

Data were primarily analyzed using NoRMCorre, CNMF, and CellReg pipelines.[197–202] Non-rigid motion correction was conducted on non-spatially and temporally downsampled data. To rectify artifacts induced by motion correction, we determined the maximum translation in each session and cropped it out before cell registration. After non-rigid motion correction, 32 Hz images were temporally downsampled by bilinear averaging to 8Hz to reduce the sampling frequency for data analysis. Data were not spatially or temporally downsampled after this point for the remainder of the analysis. We used a constrained non-negative matrix factorization pipeline for cell registration, allowing for automated registration of cells. Cells were identified based on their spatial morphology and temporal independence of dynamics. The registered cells were verified by an experimenter blinded to the pain condition or the drug administered. This verification was essential given the neuronal-like calcium activity traces shown by neuropil, including dendrites and local axons. When verifying neurons, experimenters evaluated the median and the standard deviations of the spatial profiles of the neurons and activity trace across all sessions. These metrics allowed for efficient isolation of active neurons from neuropils, background, and quiescent neurons.

Post-registration, neurons were first selected based on their responses to noxious stimuli. To identify these pain-responsive cells, we pooled evoked responses across all conditions and calculated a p-value for each neuron using single-tailed Wilcoxon rank-sum. Neurons with p<0.01 were designated as responsive to noxious stimuli. Neurons that were responsive in at least one session of the study were considered pain-responsive. While many neurons were pain-responsive in baseline testing, even more neurons were recruited after induction of chronic pain state. Subsequently, they were tested for their sensitivity to morphine, development of opioid tolerance, and sensitivity to EVP-6124. In raster plot Figures, cells are ordered by identity on the magnitude of baseline pain responses. Transients were identified based on fast rise time and slow decay. These transients were also identified based on first-time-derivative, similar to fiber photometry analysis. These transients were >2.9 median absolute deviation for at least 0.5s. The mean baseline transient rate was calculated independently for each neuron across all sessions. The same identification parameters were used for individual neurons across all sessions. To align cells across multiple sessions, we used CellReg. After assigning all neurons across all imaging sessions to a 'global' neuron, we manually inspected each mouse's cross-day neuronal registration. Given that the activity of multiple neurons was significantly correlated, substantial care was taken to ensure that the spatial footprints were appropriately segregated. ΔF/F values were generated using median fluorescence values after excluding values outside 2x median absolute deviation, similar to fiber photometry analysis. Robust-z-score was generated using similar methods as fiber photometry.

Behavior

Opioid tolerance paradigm

To induce tolerance to the antinociceptive effects of morphine, mice were exposed to twice-daily subcutaneous injections of morphine at escalating doses over seven days. On days 1-2 mice received 2x 10mg/kg injections; on days 3-4 mice received 2x 20mg/kg; and on days 5-7 received 2x 30mg/kg. Morphine or control saline injections were separated by at least 6 hours.

Tonic inflammatory pain/formalin assay

One week prior to experimentation, mice were habituated to experimenter handling, drug injection, behavioral chamber, and optical fibers. The behavioral chamber was 30cm x 30cm x 100cm (LxWxH) with transparent walls and a 45° angled mirror fixed beneath a transparent floor. On the day of testing, mice were injected intraplantar with saline or 10μL of 1.5% formalin into the plantar surface of one hind paw. The formalin solution was made by diluting 37% formaldehyde (Fisher Scientific Company, F79500) in sterile saline. Following intraplantar injection, animals were placed within the behavior chamber and monitored for 1-hour post-injection by researchers blinded to drug/optogenetic treatment conditions. All sessions were video-recorded using a Logitech camera and Dell laptop to cross-verify behavior scoring with other experimenters and reanalyze data as necessary. JWatcher (UCLA) software was used to track the amount of time the injected paw was flat, lifted, or licked. When fiber photometry was combined with the formalin assay, Synapse software was used to monitor the time spent engaging in nocifensive behaviors. Percentage time spent licking or lifting the paw during this 5-min time bin was calculated to quantify the duration of nocifensive behaviors. The first 10 mins after formalin injection was classified as the acute inflammatory pain phase, and 20-40 mins after formalin infection was classified as the tonic inflammatory pain phase.

To test the analgesic effects of drugs, we injected the test drug 10 mins prior to formalin injection. To test the analgesic efficacy of α7 nAChRs we injected agonists EVP-6124 (0.3mg/kg s.c., ChemBlock) or PHA-543613 (10mg/kg s.c., Sigma). To test the necessity of PPARα signaling, GW6471 (3mg/kg, Tocris) was injected intraperitoneally 15 min prior to EVP-6124 administration. To test the efficacy of α7 nAChR PAM, PNU-120596 (10mg/kg, Tocris) was injected subcutaneously. To test the involvement of endogenous opioid circuits, naloxone hydrochloride was administered subcutaneously (6mg/kg, Sigma-Aldrich, BP548). Morphine (10mg/kg s.c., Sigma) was used as a μ-opioid receptor agonist. NESS-0327 (0.5mg/kg, Tocris) was used as a CB1 receptor antagonist. Sterile saline or vehicle control was used in all assays. Drugs were dissolved in sterile saline, and either Kolliphor or DMSO was used to dissolve drugs when they were not water-soluble according to published protocols.[203]

Thermal radiant heat source (RHS) assay

Mice were habituated to experimenter handling and behavioral arena for three consecutive days prior to experiments. On the day of testing, the radiant heat source was placed at a distance of ∼3cm from the foot paw with a power output of ∼300mW/cm^2 in the IR wavelength range. The latency to paw withdrawal was measured when additional nocifensive signs accompanied the responses, including vocalization, repeated flicking or licking of the paw, orofacial changes, etc., to prevent incorrect classification of general locomotion related paw movement. If no response was observed at a latency of 20s, the test was stopped to avoid tissue damage. Three measurements were taken from each hind paw. Generally, in optogenetic RHS assays, we measured three paw withdrawal latencies corresponding to baseline, manipulation, and recovery.

In opioid tolerance and associated optogenetic testing, morphine was injected 1hr after optogenetic stimulation. In experiments that tested naloxone, it was injected 10 mins before the first RHS assay. Morphine was administered immediately after the first RHS assay, and the second RHS assay was conducted 10 mins later. 10 mins following the second RHS assay, optogenetic stimulation testing was carried out.

During optogenetic activation of PPTg^{ChAT+}→vlPAG terminals, an RHS assay was conducted 15 mins after 20hz pulsed stimulation. In a subset of experiments, varying frequencies of optogenetic stimulation were tested. Multiple frequencies and pulse duration paradigms resulted in analgesic effects >8 mins after optogenetic activation of PPTg^{ChAT+}→vlPAG terminals, but 10ms pulses at 20hz were chosen as they closely mimic optogenetic strategies used in various publications.[55] Optogenetic activation was conducted 3 hours after baseline testing, and the recovery assays were conducted on the subsequent day. To test for reproducibility of analgesic effects, we conducted baseline and optogenetic assays on 10 consecutive days.

vlPAG$^{Chrna7+/Oprm1+/Gad+}$ optogenetic manipulation assay was preceded by baseline testing 3 hours before the manipulation and followed by recovery testing on the subsequent day. Optogenetic activation was conducted using 20hz pulsed stimulation, and inhibition was conducted using continuous light delivery at the respective opsin activating wavelengths. During certain assays, where we were testing for pronociceptive effects, e.g., activating vlPAG$^{Chrna7+}$ neurons, we decreased the light intensity of the radiant heat source to ∼200 mW/cm^2 at a distance of ∼3 cm. The intensity was decreased to prevent 'floor' effects which could impede measurements of pronociceptive effects of optogenetic manipulation.

To test for thermal hyperalgesia, first baseline paw withdrawal latencies were measured, and then complete Freund's adjuvant (CFA, volume, company) was injected into the intraplantar surface of the hind paw. Mice were tested daily for six days 3 hours before and during optogenetic activation of PPTg^{ChAT+}→vlPAG terminals or optogenetic inhibition of vlPAG$^{Chrna7+}$ neurons.

To test the involvement of various AChRs in the antinociceptive effects of activating PPTg^{ChAT+}→vlPAG terminals, we administered antagonists systemically after baseline testing. Optogenetic stimulation was conducted 20 mins after antagonist administration for 15 mins before the RHS assay. Antagonists included atropine (10mg/kg, Sigma Aldrich), mecamylamine hydrochloride (3mg/kg, Tocris), DhBE (3mg/kg, Tocris), MLA (10mg/kg, Tocris), or AFDX 116 (6mg/kg, Tocris). Antagonists in focal drug administration studies included MLA (0.5mM, 200nL) and atropine (1mM, 200nL).

To test if EVP-6124 decreases activity of vlPAG$^{Chrna7+}$ neurons, we optogenetically activated these neurons 35 min after subcutaneous EVP-6124 administration (0.3mg/kg). The RHS assays were conducted at 30 mins and 40 mins after EVP-6124 administration. The test conducted 30 mins after EVP-6124 administration captured the analgesic effects of EVP-6124. The test conducted 40 mins after EVP-6124 administration tested the necessity for the decrease in vlPAG$^{Chrna7+}$ neuronal activity for the analgesic effects of EVP-6124.

Cold allodynia assay

Mice were habituated to experimenter handling and behavioral chamber for three consecutive days prior to experiments. Mice were placed in a test chamber of dimensions 20cm x 20cm x 20cm (LxWxH) with a 2mm thick glass floor. Crushed dry ice was applied to the glass floor below the plantar surface of the hind paws. The time taken by the mice to withdraw their paw from the noxious cold stimulus was quantified as the latency to paw flick. Experiments were conducted with an intertrial interval of 15 mins. These tests were conducted in naïve, and CFA injected paws. Latencies to paw withdrawal were repeated to obtain three values for each hind paw which were then averaged.

Mechanical von Frey assay

Mice were habituated to experimenter handling and behavioral chamber for three consecutive days prior to experiments. Mice were placed in a test chamber 20cm x 20cm x 20cm with a mesh floor. Von Frey Filaments (EB Instruments, Fisher Scientific Company, NM1208120) were pressed perpendicular to the plantar surface of one hind paw applying a constant force to the paw. Paw withdrawal response or lack of a response was recorded for each force of the von Frey filament ranging from 0.04g to 8g using the up-down method. These tests were conducted in naïve, and CFA injected paws. von Frey assays were conducted before (baseline), during, and after (recovery) optogenetic manipulation. Recovery tests were conducted on the day after optogenetic manipulation.

Chronic inflammatory assay

We used complete Freund's adjuvant (CFA) to induce a chronic inflammatory pain state. 20uL of CFA (Sigma-Aldrich, F5881) diluted 1:1 in sterile saline was injected into the hind paw using a 30G insulin syringe. The mice were picked from and returned to the home cage for the CFA injection. The mice were monitored daily for significant changes in health and behavior. Effects of chronic inflammatory pain on neuronal physiology using fiber photometry were tested within and between groups one day prior to CFA injection and three days after CFA injection unless otherwise stated.

Chronic neuropathic assay

To induce a chronic neuropathic pain state, mice were injected subcutaneously with paclitaxel (8mg/kg, Thermo Scientific, AAJ62734MC) on alternate days for eight days, resulting in a total of 4 injections. The mice were picked from and returned to the home cage for these injections. During and after this injection protocol, mice were monitored daily for changes in health and behavior. Effects of chronic neuropathic pain on neuronal physiology using fiber photometry were tested within and between groups one day prior to the first paclitaxel injection and ten days after the last paclitaxel injection unless otherwise stated.

Noxious mechanical or thermal assays

To explore the responses of vlPAG$^{Chrna7+}$ neurons, we administered multiple noxious stimuli. These included pinprick, applying acetone to the hind paw, and applying water at different temperatures to the hind paw. These assays were conducted in the same chamber as mechanical von Frey assays. The order was kept consistent across animals tested. In these assays, high frame rate video capture was used to time lock the nocifensive responses to the fiber photometry signal. For the pinprick, a 25G needle (BD, Fisher Scientific Company, 511098) was applied to the plantar surface of one hind paw. The pressure was applied to the point of tissue indentation without rupturing the paw surface.

To test for cooling-induced nocifensive responses associated with acetone, using a micropipette (Eppendorf, 20-200μL, 3123000055), 20μL of 100% Acetone (Fisher Scientific Company, A18P-4) was applied to the plantar surface of one hind paw. To test for nocifensive responses evoked by water at 55°C, distilled water was maintained at heated to 57°C using a dry bath incubator, and 20μL was applied to the hindpaw using a micropipette. To test for nocifensive responses evoked by water at 2°C, ice water was applied to the hindpaw using a micropipette. The time between pipetting the water in either condition and application was calibrated such that by the time water was applied, the temperature of the water was 55°C or 2°C, as necessary.

Salient stimuli assays

To explore the responses of vlPAG$^{Chrna7+}$ neurons, we administered multiple salient stimuli that were inherently non-noxious. These stimuli included experimenter approach to the plantar surface of the paw, white light, auditory tone, plantar brush, and water application, and oral sucrose and quinine administration. These experiments were conducted in the same chamber as von Frey assays. For 'experimenter approach', the experimenter approached the plantar surface of the paw with regular von Frey filaments, but the filament was not touched to the paw. For light application, white light was projected onto the eyes of the mouse at 2000 lux. For auditory tone, 18kHz at 50dB was played for 500ms at a 20cm distance from the mice. To test non-noxious somatosensory stimuli, a brush (Royal & Langnickel size 2) was lightly applied to the plantar surface of the hindpaw, and 20μL of water at 27°C was applied to the plantar surface of the hindpaw using a micropipette. For intraoral delivery of rewarding and aversive gustatory stimuli, 50μL 30% sucrose or 0.2 mg/ml quinine were delivered orally for the mice to spontaneously lick from the micropippeter. The quinine was presented after multiple bouts of sucrose licks.

Open field assay

Mice were placed in a custom-made white acrylic chamber (42cm x 42cm x 20cm) for 20 min. Locomotion was captured using Ethovision XT-16 software by a video camera mounted above the behavioral chamber. We used Ethovision to monitor the mouse's center

point, which captured the distance moved, locomotion speed, and movement bouts in 30 sec time bins. These binned locomotor parameters were correlated with fiber photometry data to test for relationships between locomotion and ACh levels or activity of vlPAG$^{Chrna7+}$ neurons using temporal cross-correlation. The correlogram was compared with shuffled data to test for the significance of correlations. In addition to center point-based locomotion, we used head and tail point detection based on fine movements and pixel energy based on the total change in pixels in the video frame to evaluate if fine movements were correlated with physiological parameters using a similar analysis. Spontaneous activity was recorded in the open field chamber unless otherwise stated. To test for changes in anxiety phenotypes during stimulation, we quantified the time spent in the center of the open field and the number of entries into the center region using arenas defined in Ethovision. The center of the arena was 21cm x 21cm. These anxiety assays were conducted for 20 mins, and optogenetic activation or inhibition was conducted for either the first or last 10 mins counterbalanced within groups.

Rotarod assay

Mice were acclimatized to the experimental room for 30 mins before testing. The rotarod (Columbus Instruments, Rota Rod Rotamex 5) was started at four rotations per min (rpm). Then animals were placed in a way so that they walked forward in individual lanes. Four animals were tested simultaneously. The rotations were increased by 1 rpm every 10s. The latency to fall was measured. The assay was stopped after 200s. Five repeated trials were conducted with an intertrial interval of 5 mins, and the latency to fall (s) was averaged across trials. Drugs were injected 15 mins before the first trial. Optogenetic stimulation was conducted for 15min before the first trial and during the intertrial intervals.

Somatic withdrawal assays

Mice subjected to the opioid exposure paradigm described above were injected with naloxone (6mg/kg). They were placed in a cylindrical chamber with transparent walls with a diameter of 5 in and a height of 10 in. In a 10 min period, the number of times that mice stood on their hind legs was quantified as 'rearing', and the number of times mice jumped (all four paws were off the ground) was quantified as 'escape jumps'. These behaviors are well-characterized outcomes of naloxone-precipitated opioid withdrawal. Optogenetic inhibition of vlPAG$^{Chrna7+}$ neurons was conducted to test for relief of somatic withdrawal signs, including rearing and jumping.

Real-time place preference assay

Mice were placed into a custom-made black acrylic two-chambered box (52cm x 26cm x 26cm) and allowed to explore the chambers for 20 min. Optogenetic stimulation was triggered based on a pre-decided 'stimulation-paired' chamber when mice spontaneously moved to the stimulation-paired chamber. The physical side of the 'stimulation-paired' chamber was counterbalanced in these experiments. During these experiments, mice were tethered to an optogenetic patch cord with a rotary joint, and their position was tracked using a Basler camera and Noldus Ethovision XT 16 software. The amount of time spent in the 'stimulation-paired' chamber as a percent of total time (20 min) was quantified. Optogenetic stimulation strategy in the real-time place preference assay is defined in the optogenetics section.

Conditioned place preference assay

A custom-made three-chambered behavioral apparatus was used (58cm x 28cm x 28cm). The walls had either vertical or horizontal black stripes with different textured floors in the two main chambers (26cm x 28cm x 28cm). These main chambers were connected by a small central connecting chamber (6cm x 6xm x 28cm). A camera was positioned above the behavioral apparatus to track mice using Noldus Ethovision XT 16 software. On the preconditioning day (day 1), mice were allowed to freely roam the three chambers for 20 mins. This preconditioning data was used to counterbalance the initial chamber preference. We used an unbiased design, wherein groups contained an equal number of mice that showed a preference for the chamber that they would receive or would not receive drug or optogenetic manipulation. On the next three consecutive days (days 2–4), mice underwent a morning and afternoon conditioning session separated by at least 6 hours. In the morning session, mice were secluded in one chamber for 20 mins, and in the afternoon session, mice were secluded in the other chamber for 20 mins. On the post-conditioning day (day 5), mice were allowed to freely roam all chambers. The amount of time spent in either chamber was captured using a video camera interfaced with Ethovision XT 16.

For drug or pain conditioning-based CPP experiments, WT mice were used. When testing for affective pain relief by EVP-6124 – after the pre-conditioning day, mice were split up into two groups. Group 1 received a subcutaneous saline injection and intraplantar saline injection (10μL) in the morning and a subcutaneous saline injection and intraplantar 2% formalin injection (10μL) in the afternoon. Group 2 received a subcutaneous saline injection and intraplantar 2% formalin injection in the morning and a subcutaneous EVP 6124 injection and intraplantar 2% formalin injection in the afternoon.

When testing for withdrawal effects associated with EVP-6124 and morphine use, mice were injected with EVP-6124 or morphine for five days. On Day 6, preconditioning baseline preference was monitored. For conditioning, Group 1 received EVP-6124 and saline in the morning and EVP-6124 and MLA in the afternoon. Group 2 received morphine and saline in the morning and morphine and naloxone in the afternoon. Antagonist or saline was injected 10 mins prior to EVP-6124/morphine injection.

For reward profile testing of the conditioned drugs, animals were injected with saline in the morning and EVP-6124, morphine, or saline in the afternoon. The post-conditioning preference for all groups was monitored on the subsequent day. Drug concentrations used in these assays: EVP-6124 (0.3mg/kg), morphine (10mg/kg), naloxone (6mg/kg), and MLA (10mg/kg).

Histology

Viral and cannula placement

Mice were deeply anesthetized with isoflurane and perfused with cold phosphate-buffered saline, followed by perfusion with 4% paraformaldehyde in PBS. Brains were then placed in PFA for 24 hours and then immersed in hypertonic sucrose solution, first 15% and then 30% until they sank. They were subsequently embedded in optimal cutting temperature (OCT) compound (Tissue-Plus, FisherBrand) until slicing. 40 μm coronal slices (Leica CS3050 S) were cut and mounted onto Superfrost-Plus Microscope Slides (FisherBrand) with DAPI Fluoromount-G (Southern Biotech) and covered by a coverslip (Fisherbrand). Slides were stored at 4°C until imaging. The slices were imaged on a confocal microscope (Marianas 3i spinning disk confocal) for viral and cannula placement at 20x magnification (Zeiss). These images were masked, and if the majority of viral spread or cannula tip was outside the intended region, the animals and the associated data were discarded.

Immunohistochemistry

Slicing procedures were the same as above. But for immunohistochemistry staining, slices were transferred to a 24 well-plate and immersed in PBS (1X, pH 7.4). Slices were treated for 1 hour with a blocking solution based in PBS (1X, pH 7.4) with 0.01% Triton X-100 (Electron Microscopy Sciences, 22145) and 10% Normal Goat or Donkey Serum (Abcam, AB 7481, AB 7475). For the described experiments, one or multiple of the following primary antibodies were mixed in blocking solution: solution: anti-μ-OR (Abcam 134054), Anti-NAPE-PLD (Abcam 246951), Anti-pAMPK (Cell Signaling 2535), Anti pK$_v$2.1 (S563 and S603) (gift from James Trimmer). In experiments exploring protein expression of α7 nAChRs, we used fluorescently conjugated α-Bungarotoxin (Invitrogen B13422 or B35450). Slices were incubated in the primary antibody overnight and triple washed with PBS (1X, pH 7.4) the following morning. When using antibodies raised in mice, Mouse F(ab) IgG H&L fragments were used (Abcam 6668). Secondary antibodies were chosen according to the blocking serum, the primary antibody's host, and multiplexing with other antibodies. For example, if we used normal goat serum and primary raised in rabbit, and needed staining in 488/green channel, we used 1:400 dilution of Goat Anti-Rabbit IgG H&L (Alexa Fluor 488, Abcam 150077). Secondaries antibodies were allowed to incubate for 2 hours. Slices were then triple-washed and mounted on Superfrost-Plus Microscope Slides (FisherBrand) with DAPI Fluoromount-G (Southern Biotech) and covered by a coverslip (Fisherbrand). Slides were covered and stored at 4°C until imaging. For visualization, the slices were imaged on a confocal microscope (Marianas 3i spinning disk confocal) at 20x (Zeiss Plan-Neofluar NA 0.5 air) or 40x (Zeiss Plan-Apochromat NA 1.3 oil). In certain experiments, mice were either pretreated *in vivo* with α7 nAChR agonist or saline, and then exposed to a pain state using formalin or saline injection in the hindpaw. Care was taken to acclimatize the animals to handling, transport, and anesthesia-related stress for 3-days prior to the perfusion. Animals were sacrificed 30 mins after drug or formalin injection. For vlPAG slices, 1 in 4 sampling was used, i.e., every 4th brain slice was used to cover the extent of the vlPAG. For whole-brain slicing exploring cholinergic inputs, 1 in 6 sampling was used. Known cholinergic nuclei with long-range projections were selectively explored for labeling. After image acquisition, slices were analyzed for overlap using a custom-written script in Cell Profiler in a manner similar to the analysis profile used for FISH. To evaluate changes in expression or phosphorylation levels of proteins of interest, data from both experimental groups were acquired, processed, and analyzed with exactly the same parameters by experimenters blinded to the treatment. At least one slice per animal was included where no primary antibody was added and another slice where no secondary antibody was added to test for nonspecific labeling or background fluorescence, respectively.

Fluorescent in situ hybridization/RNAScope

Adult (∼P60) wild-type male and female (n = 4 total) were used for these experiments. Mice were deeply anesthetized with isoflurane, and brains were extracted and immediately flash-frozen over dry ice and in -80°C under RNase-free conditions. Care was taken to ensure that decapitation to permanent freezing happened within ∼45 s - 1 min. After the brains were completely frozen, they were embedded in OCT compound (Tissue-plus, Fisherbrand) and frozen once again. Brains were sliced along the coronal plane at a thickness of 20μm (Leica CS3050 S). These slices were immediately transferred to Superfrost Plus Microscope Slides (Fisherbrand) and stored at -80°C until the next day, when the hybridization protocol was conducted.

The hybridization assay was conducted as per Advanced Cell Diagnostics (ACD) instructions for Manual RNAscope Fluorescent Multiplex Assay. Materials for this experiment were purchased as a complete kit from ACD (ACD, 321720). Slides were removed from the -80°C freezer and fixed in chilled 4% PFA using Tissue-Tek containers for 10 mins. The tissue was then dehydrated in 50% EtOH, 70% EtOH, and 2x in 100% for 5 min immersions. Slides were air-dried, and a hydrophobic barrier was drawn by a hydrophobic pen (Immedge Pen). After the barrier was dried, the slices were treated with a protease (Protease 4) that completely covered the slice for 30 min at room temperature. The protease was removed from the slides. The slides were placed in the Tissue-Tek hybEZ slide rack and staining dish and washed with PBS (1X, pH 7.4). Probes were mixed so that Channel 1, Channel 2, and Channel 3 had a 50:1:1 dilution, per ACD instructions, and were warmed to 40°C. The probe mix was pipetted onto the tissue to fully immersed the tissue. The slides were then placed in a sealed 40°C oven for 2 hours (HybEZ oven). The slides were then washed in 1X RNAscope wash buffer (ACD) three times for 2 mins each. AMP-1 was then applied to the slides and incubated in the oven for 30 mins. After incubation, slices were washed three times in the RNAScope wash buffer. The process of incubation and triple washing was repeated for AMP-2 (15 min incubation), AMP-3 (30 mins), and AMP 4-FL (15 mins). After the final wash, nuclei were counterstained using DAPI Fluoromount-G (Southern Biotech), and slides were coverslipped (Fisherbrand). Slides were stored at 4°C in a dark environment until imaging on the subsequent day.

Images were acquired with a Marianas confocal microscope and 3i software using a 20x (Zeiss Plan-Neofluar NA 0.5 air) or 40x (Zeiss Plan-Apochromat NA 1.3 oil) objective. 16-bit images were acquired using the same microscope settings for each quantified

image, i.e., similar intensity, threshold, and exposure times. The images were analyzed using a custom script written in CellProfiler. To analyze the images, individual channels corresponding to 405 nm, 488 nm, 561 nm, and 647 nm excitation were extracted. No deconvolution was performed. The DAPI/405 nm images were used to draw nuclei outlines using size, roundness, intensity, and contrast parameters. After identifying the nuclei, the number of green, orange, and red puncta were quantified using intensity, roundness, and size thresholds. Given that few mRNA, including those of vGat and vGlut, were extremely highly expressed, we used % area coverage as our measure instead of counting puncta. This parameter captured the amount of extended nucleus area covered by probes in green, orange, or red channels. The extended nucleus area was characterized by increasing the diameter of the DAPI stained nucleus to 20 μm. Generally, the % area coverage correlated strongly with the number of puncta in separately analyzed data. Background intensity values were obtained from ROIs that lacked cell bodies and subtracted independently in each channel, if necessary. Parameters to identify mRNA puncta, including area and nucleus boundaries, were kept consistent across slices. Positive and negative cells were categorized based on an adapted Otsu thresholding method. Generally, these required % area coverage to be $>\sim3\%$ of the extended nucleus area. Three slices spanning the anterior-posterior axis of vlPAG were used for the analysis. From each slice, six fields of view were captured for the analysis. Images were taken with six z-plane steps with 3μm step sizes. All assays included three positive (*Polr2a, Ppib, Ubc*) and one negative control probe (*Dapb*), which were used to verify the signal in the slides with test probes. Where possible, positive and negative tests were conducted using brain regions known to contain mRNA of the concerned test probe, e.g., VTA, hippocampus, mHb, etc. The RNAScope probes reference numbers that were used are listed: Neurotransmitters: 317621 – Th; 319191 – *Slc32a1*; 319171 – *Slc17a6*; 410351 – *Tac1*; 318761 – *Penk*; 318771 – *Pdyn*; 408731 – *Chat*; 404631 – *Sst*; and 313321 – *Npy*. Cholinergic receptors: 495291 – *Chrm1*; 495311 – *Chrm2*; 437701 – *Chrm3*; 410581 – *Chrm4*; 495301 – *Chrm5*; 312571 – *Chrna5*; 465161 – *Chrna7*; 449231 – *Chrnb2*; 449201 – *Chrnb3*; and 452971 – *Chrnb4*. Other targets: 315841 – *Oprm1*; 420721 – *Cnr1*; 466631 – *Hcrtr1*; 418851 – *Glp1r*; 411141 – *Htr3a*; 406501 – *Drd2*; and 474001 – *Cre-O1*.

QUANTIFICATION AND STATISTICAL ANALYSIS

Data are expressed as means ± standard error of the mean in Figures and text. Paired or unpaired two-tailed t-tests with or without Sidak multiple comparisons as appropriate. One-way, two-way, and repeated-measures ANOVA were used to compare more than two groups using Graphpad or MATLAB. Signed-rank and rank-sum tests refer to Wilcoxon signed-rank and rank-sum tests, respectively. For spontaneous post-synaptic currents, unpaired t-test was used to test for changes in frequency, and Kolmogorov–Smirnov test was used to test for differences in amplitude distributions. Spontaneous synaptic or calcium events were visually verified by the experimenter blinded to treatment group to ensure that the software determined the events correctly. For behavioral assays, either unpaired t-test, paired t-test, 1-way ANOVA or 2-way repeated-measures ANOVA was used to analyze data, and Sidak multiple comparisons test was used as appropriate. The main-effects and interactions were quantified using RM ANOVA. The paired t-test referring to within group testing was computed using Sidak multiple comparison test to obtain the within group adjusted p-value and the corresponding t-statistic. For example, in Figure 2F, when comparing effects of optogenetic activation on latency, we look at the interaction term according to RM-ANOVA. But, we also report within group and between group comparisons using t-tests as appropriate, e.g. the GFP and ChR2 group is compared in baseline and stimulated conditions and we report the t-tests with p-value calculated according to Sidak multiple comparison test. We used identical code and analysis methods for all cohorts throughout the study. All experiments were randomized and performed by a researcher blind to the viral injection or the pain state. Mice were not selected for any experimental condition based on previous observations or tests. Individual mice within cages were chosen arbitrarily to receive control or experimental viral injections, opioid tolerance treatment, or chronic pain manipulation. Individual mice were ear-tagged to assist in post-hoc verification of the animal's identity. At least one animal from each group was tested within an experimental session. Generally, no cage was assigned for just one manipulation. Optogenetic stimulation frequencies, drug concentrations, and tolerance exposure paradigms were selected based on preliminary experiments. All behavioral experiments were recorded by computer videography and analyzed in a blinded manner. Histological verifications were conducted prior to the final analysis of behavioral data. Experimenters were blinded to the groups during histological verification to the group allocation. Sample sizes were predetermined for optogenetic and electrophysiological studies using power analysis, but were not predetermined for fiber photometry and imaging studies. Variances observed on a subset of fiber photometry and imaging experiments were used to conduct power analysis for the remaining experiments. Our current experimental n's are adequate to measure differences based on this post-hoc power analysis on a subset of assays. Our sample sizes are similar to those reported in the literature. All relevant data and code are available from the authors upon reasonable request.

Test, statistics, significance levels, and sample sizes for each experiment are listed in Table S1. ns $p > 0.05$, t tests and post hoc comparisons: *$p < 0.05$, **$p < 0.01$, ***$p < 0.001$, ****$p < 0.0001$; interaction: # < 0.05, ## $p < 0.01$, ### $p < 0.001$, #### $p < 0.0001$.